The role of FtsZ treadmilling and torsional stress for bacterial cytokinesis: an *in vitro* study

Diego Alejandro Ramirez Diaz

München 2019

The role of FtsZ treadmilling and torsional stress for bacterial cytokinesis: an *in vitro* study

Dissertation
an der Fakultät für Physik
der Ludwig-Maximilians-Universität München

vorgelegt von

Diego Alejandro Ramirez Diaz
aus Pamplona, Kolumbien

München, den 13. März 2019

Erstgutachter: Prof. Dr. Petra Schwille

Zweitgutachter: Prof. Dr. German Rivas

Tag der mündlichen Prüfung: 29. April 2019

KURZFASSUNG

In dieser Dissertation studierte ich die „Treadmilling“-Dynamik der GTPase FtsZ *in vitro*. FtsZ gehört zu den häufigsten Proteinen, die an der bakteriellen Zellteilung beteiligt sind. Da FtsZ *in vivo* an der Lipid Membran verankert ist und eine ringartige Struktur formt, wurde vermutet, dass FtsZ für den mechanischen Prozess der Zytokinese Einschnürungskräfte ausübt. Mehr noch als zu testen, ob FtsZ Kräfte ausübt, die hinreichend für die bakterielle Zellteilung sind, soll die hier präsentierte Studie vielmehr Eigenschaften von FtsZ Polymeren aufzeigen um den physikalischen Prozess der Einschnürung zu verstehen. Zuerst habe ich vorherige Konzepte über die Rolle von FtsA als natürliches Ankerprotein in Frage gestellt nach Rekonstituierung von FtsZ auf „Supported Lipid Membranes“ (SLBs). Anders als erwartet konnte ich zeigen, dass die FtsZ-YFP-mts Chimäre autonom an die Membran binden kann und die Proteine sich auf der Membran zu einer ringartigen Struktur zusammensetzen, abhängig von der Dichte der Proteine auf der Membranoberfläche. Dieser Ring weist „treadmilling“ Verhalten auf, welches sich in einer anscheinenden Rotation im Uhrzeigersinn äußert. Bei intermediären Proteindichten von FtsZ-YFP-mts formten sich Ringe und bei hohen Proteindichten formten sich parallel zueinander liegende Filamente in nematischer Anordnung. Ferner scheint die Entstehung der ringförmigen Strukturen, ähnlich der *in vivo* Situation, eher von der GTPase Aktivität abzuhängen als von spezifischen Protein-Anker Interaktionen.

Um den Einfluß von FtsZ auf deformierbare Oberflächen zu untersuchen, habe ich Verfahren entwickelt, um FtsZ Ringe an der Außenseite von gigantischen unilamellaren Vesikeln (GUVs) zu rekonstituieren. Nachdem die Vesikel einem osmotischen Schock ausgesetzt wurden um sie deformierbar zu machen, induzierten die FtsZ Ringe durch „Bohr-Kräfte“ nach innen gerichtete Membraneinstülpungen („Membran-Kegel“). Mit den nach innen gerichteten Membraneinstülpungen zeigte FtsZ „treadmilling“ Richtungen sowohl im Uhrzeigersinn, als auch gegen den Uhrzeigersinn. Ferner, um den Einfluß von FtsZ auf zylindrische Geometrien zu untersuchen, habe ich ein neues Verfahren entwickelt, um längliche, weiche, Membranausstülpungen aus GUVs mit Hilfe optischer Pinzetten zu ziehen. Bei GUVs mit FtsZ Ringen an der Membranaußenseite und nach innen gerichteten Membrane-

instülpungen, wurden die weichen mit der optischen Pinzette gezogenen „Lipid-Röhren“ bemerkenswerterweise durch FtsZ in eine 3D-helikale, federartige Struktur transformiert. Diese helikalen Deformationen lassen sich durch Verdrehen eines elastischen Stabes erklären. Zusätzlich verursacht die GTPase Aktivität einen „super-verdrehten“ Zustand der ausgezogenen Lipid Membran, die eine Feder-Kompression verursacht mit Kräften um die $0.6 - 1$ pN. Diese GTPase abhängige Feder-Kompression entspricht den Einschnürungen, wenn FtsZ innerhalb von GUVs rekonstituiert wurde. Daher schlage ich vor, dass FtsZ bedingte Einschnürungen durch Torsion erzeugt werden.

ABSTRACT

In this thesis, I studied the treadmilling-dynamic properties of GTP-consuming FtsZ filaments *in vitro*. FtsZ is the most abundant protein in bacteria cell-division machinery. Since FtsZ filaments are anchored to the lipid membrane to form a ring-like structure, it has been suggested that FtsZ exerts constriction-forces driving the mechanical process of cytokinesis. More than determining whether FtsZ generate forces that suffice bacteria cell division, the here presented *in vitro* study sheds light on FtsZ polymer properties aiming to understand the physical process of constriction. First, I challenged previous conceptions about the role of FtsA, a natural FtsZ membrane anchor, when FtsZ was reconstituted on Supported-Lipid Membranes (SLBs). Contrary to expected, I found that an autonomous membrane binding chimera FtsZ-YFP-mts self-assembles into treadmilling (clockwise-rotation) ring-like structures as a function of the surface protein density. At intermediate surface densities, FtsZ-YFP-mts formed rings whereas, at high surface densities, filaments exhibited a parallel-nematic arrangement. Moreover, rather than an specific protein-anchor interaction, FtsZ GTPase activity determined the emergence of treadmilling rings as also shown *in vivo*.

To explore the impact of FtsZ on deformable surfaces, I found the conditions to reconstitute FtsZ rings outside Giant Unilamellar Vesicles (GUVs). Once vesicles were deflated (deformable), rings induced drilling-like forces shaping inwards cones. In this cone-geometry, FtsZ showed clockwise/anticlockwise treadmilling directions. Moreover, to investigate the impact of FtsZ on tubular geometries, I implemented a novel technique to pull soft lipid tubes (from GUVs) using optical tweezers. Then, soft tubes were pulled from GUVs displaying (outside) FtsZ rings and inwards deformation. Strikingly, FtsZ transformed the lipid tube into a 3D helical spring-like structure. These helical deformations can be rationalized by twisting an elastic rod. In addition, GTPase activity triggered a super-twisted state causing spring compression and delivering forces around $0.6 - 1$ pN. This GTPase dependent spring-compression resulted equivalent to the formation of constriction necks when FtsZ was reconstituted inside GUVs. Therefore, I suggest that FtsZ makes constriction via torsional stress.

Contents

List of Figures

I

INTRODUCTION AND OUTLINE

FtsZ is the most abundant protein in the bacteria divisome. Since FtsZ filaments are anchored to the lipid membrane to form a ring-like structure, it has been suggested that FtsZ exerts constriction-forces driving the mechanical process of cytokinesis [28, 35]. However, in view of the mechanical requirements to drive cytokinesis it is unclear whether FtsZ could deliver forces that suffice cell division [19,38]. More than determining whether FtsZ generate forces that suffice bacteria cell division, **the here presented *in vitro* investigation aims to reveal FtsZ polymer properties than can be linked to the physical process of constriction. "Finding how FtsZ could perform constriction".** *In vitro* approach provides several technical advantages in view of controlling parameter space such as protein concentration, geometry, and surface stiffness [86]. In addition, using *in vitro* reconstitution, FtsZ force measurement can be achieved.

This aim can be divided in two questions:

1. **Can a "very" minimal FtsZ protein system rescue self-assembly into treadmilling dynamic ring-like structures on a flat-stiff geometry (SLB)?** (Chapter II)

   (a) **Does the anchoring determine the FtsZ self-assembly of treadmilling ring like structures?** According to Loose and Mitchison, the FtsZ self assembles into dynamic swirls only when FtsA anchors FtsZ to the supported lipid membrane [53].

   (b) **What parameters rule the emergence of FtsZ treadmilling rotating rings on SLBs?**

2. **What is the impact of FtsZ ring self-assembly when reconstituted in a deformable lipid surface?** (Chapter IV)

   (a) **What type of deformations over a soft tubular geometry are equivalent to inwards deformations on a flat soft surface? (FtsZ outside**

geometry) Erickson and coworkers have shown that FtsZ filaments can generate inwards deformations [70]. However, no rings were observed in this report.

(b) **What FtsZ property explains lipid tube transformations (FtsZ outside geometry) when compared to FtsZ-inside-geometry?**

To create a soft tubular geometry, current techniques to pull lipid tubes from GUVs using optical tweezers had to be modified [80,89] to achieve a large diameter and soft tube. This represented a technical advance achieved in this thesis (Chapter III).

II

SELF-ASSEMBLY OF FTSZ-YFP-MTS INTO TREADMILLING RING-LIKE STRUCTURES ON SUPPORTED LIPID BILAYERS

In this chapter, I challenge the current views about the role of FtsA in the process of creating treadmilling FtsZ filaments, as suggested by Loose and Mitchison (2018) [53]. To prove that the exclusivity for the FtsA is not a requirement, I showed that FtsZ-YFP-mts (Fig II.3B) also self-assembles into dynamic treadmilling rings only in certain surface density regime. In addition, I found that the destabilization process required to obtain dynamic treadmilling rings arise from the GTPase activity. This work validates the functionality of the protein chimera FtsZ-YFP-mts to be further used as a robust protein model since it rescues the self-assembly and dynamic properties of FtsZ-FtsA.

II.1 State of the Art (extended introduction)

II.1.1 FtsZ and the bacterial cytokinesis machinery

Most bacterial cells divide by binary fission which is coordinated by a protein complex called the divisome [35]. FtsZ, a GTPase polymeric protein with structural homology to tubulin [28], represents the most abundant component of the divisome. Similar to tubulin, polymerization occurs when GTP binds the N-terminal (Fig.II.1 A) and a second monomer docks over this binding site from the C-terminal (head-to-tail polymerization) [1]. In this way, FtsZ represents a self activating GTPase since its catalytic activity is triggered only upon polymerization [1]. *In vitro*, FtsZ exhibits cooperative assembly of different polymeric species: single filaments, bundles, rings and sheets, depending on the experimental conditions [26,57,59,63,79]. On the other hand, *in vivo*, FtsZ forms a ring in the center of cell with an architecture that remains unclear. Super-resolution microscopy

techniques have shown a non-continuous ring (Fig. II.1 B) built of different patches or bundles [18].

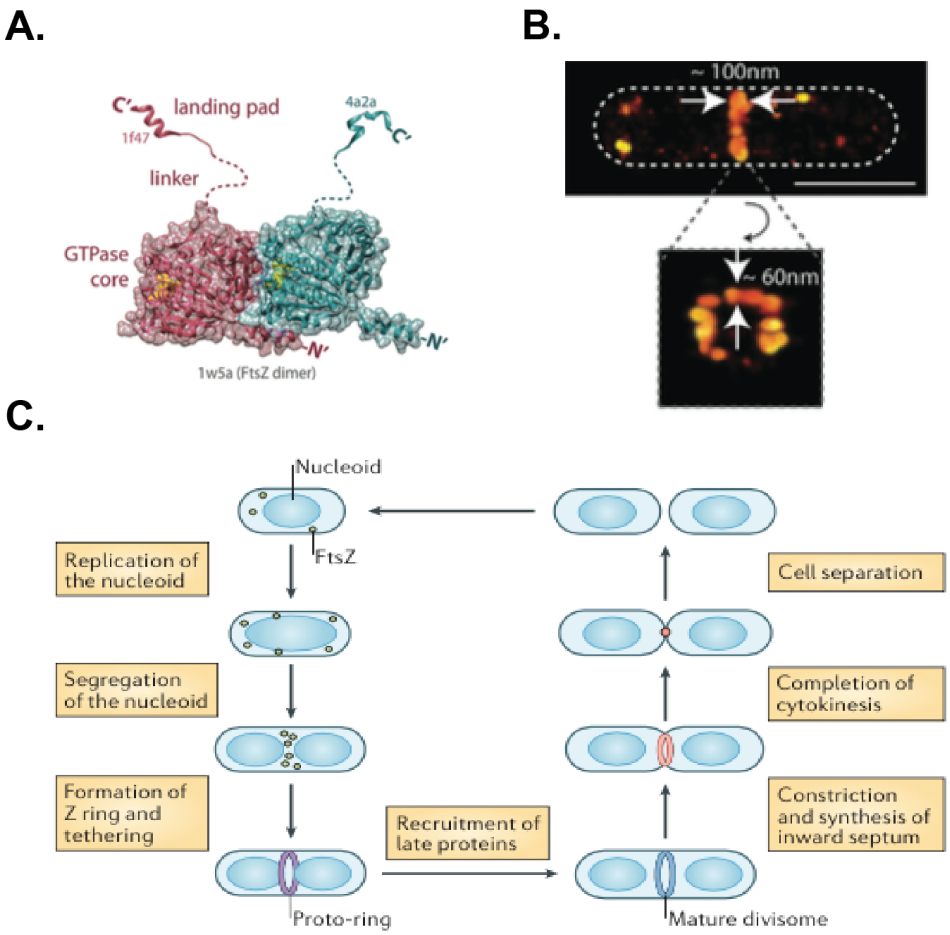

Figure II.1: FtsZ ring and bacterial cell division cycle. A) FtsZ dimer displaying head-to-tail polymerization. B) Super-resolution image of Z-ring using PALM (Photo-activated localization microscopy) (A and B adapted from [19]). C) Bacterial cell division cycle. Adapted from [35].

The assembly of the divisome is can be described and simplified as a two-step process [20]. The early stage of the divisome begins with anchoring FtsZ filaments to the plasma membrane to form the Z-ring (protoring)(Fig. II.1C). FtsA and ZipA represent the two most important anchors in *E. coli* [28]. FtsA interacts with the membrane through a alpha-helix over the C-terminal (membrane targeting sequence, mts) implying a transient binding. In contrast, ZipA has a trans-membrane domain suggesting a more permanent binding [35]. Both anchor proteins interact with FtsZ via the C-linker (Fig.II.1 A) [19,28].

Furthermore, the Z-ring needs to be spatially regulated and positioned in the center of bacteria. To achieve this, positive protein regulators guide FtsZ filaments to be assembled mid-cell. Before FtsZ, PomZ goes mid-cell and promotes FtsZ assembly in *Myxococcus xanthus* [106]. Interestingly, PomZ is ParA homolog (DNA segregation protein) which suggest a connection between FtsZ and chromosome segregation [20]. In addition, FtsZ negative regulators such as Min proteins or nucleoid occlusion are widely studied. MinCDE system oscillates pole-to-pole in rod-shaped bacteria. As a result of this gradient, the concentration of MinC is maximal at the poles and minimal in the center of the cell. Since MinC is a negative regulator of FtsZ, FtsZ assembly occurs mainly in the center of the cell [90]. On the other hand, the DNA-associated nucleoid occlussion system with SlmA protein for *E.coli* and Noc in *B. subtilis* prevent the formation of FtsZ ring-like structures over unsegregated chromosomes [20]. Lastly, proteins such as ZapA (FtsZ crosslinkers) and FtsEX (signaling cell wall hydrolysis) are incorporated to the Z-ring [25].

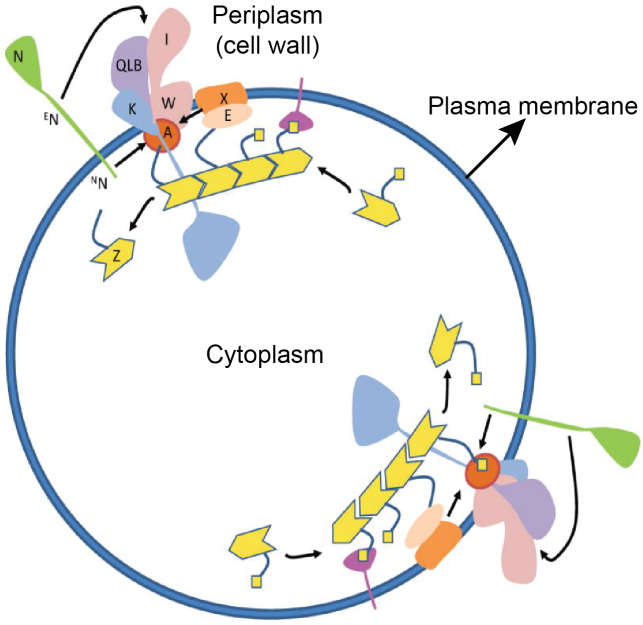

Figure II.2: Divisome assembly to trigger septum formation. The Z ring (early stage) recruits machinery for peptidoglycan synthesis to activate constriction and septum formation. Figure adapted from [25]

In the last stage, the divisome recruits the machinery to synthesize peptidoglycan (PG) such as PBSs (PBP3 or FtsI) and FtsW proteins [20, 35]. The peptidoglycan cell wall is constituted by a mesh of sugars cross-linked by peptides, that provide mechanical rigidity to maintain bacteria shape [95]. This wall is located on the outer side of the plasma

membrane, in the periplasm (Fig. II.2). Although the recruiting mechanism is unknown, monomeric FtsA serves as docking site for these proteins. In this context, FtsA plays a vital role of connecting the Z-ring from the cytoplasm side with the periplasm and the PG (Fig. II.2). In addition, FtsN arrival triggers the start of the PG synthesis and membrane invagination [25]. Since the N-terminal of FtsN interacts with FtsA [25], data suggest that FtsN actuates the FtsQLB+FtsA switch [52, 107]. When the switch is inactivated without FtsN, the complex FtsQLB inhibits enzymatic activity of PBP3. Therefore, FtsN closes the loop and enable *in situ* PG production. Consequently, FtsA+FtsN interacts with FtsEX (cell wall hydrolysis) complex to regulate PG synthesis as well as hydrolysis [25].

.

II.1.2 Constriction forces and dynamics: FtsZ-YFP-mts *in vitro* constriction and FtsZ *in vivo* treadmilling

An important question remains yet to be answered: What is the origin of the cytokinesis force? [19,28,35,38]. Most common bacteria such as *E. coli* and *B. subtilis* are rod-shaped bacteria (Fig. II.3A). Then, dividing a rod-like bacteria into two daughters that conserve volume and diameter incurs of an energetic cost in the order of $10^{-19} - 10^{-18}$ J only considering lipid contribution (exercise proposed in [12]). However, bacteria have other mechanical elements to be considered: turgor pressure and cell wall [116]. Turgor or internal pressure in *E. coli* and *B. subtilis* range from $0.3-2$ MPa [21,115] respectively. Therefore, a septum-like section of $60 nm$ width and $3\ \mu m$ circumference have to hold forces in the range $50 - 300$ nN due to this pressure [116]. To bear this pressure range, the peptidoglycan cell wall provides sufficient mechanical rigidity to maintain shape. Interestingly, *E. coli* PG layer is thinner ($\sim 6\ nm$, ref) compared to *B. subtilis* ($\sim 40\ nm$, ref) in agreement with different turgor pressure [116]. By considering turgor pressure, the amount of work required for dividing a rod-shape bacteria might be in the order of 10^{-14} J. Therefore, what is the source of this energy?

Since FtsZ is the most abundant protein in the divisome and has GTPase activity (energy consumption), the idea of a contractile FtsZ ring became exciting. In fact, an estimation of the energy released by GTP hydrolysis ($\Delta G \sim$ 30kJ/mol [116]) for a typical FtsZ concentration ($\sim 3\ \mu M$ [33]) could equal the energy required for cell division ($\sim 10^{-14}$ J),

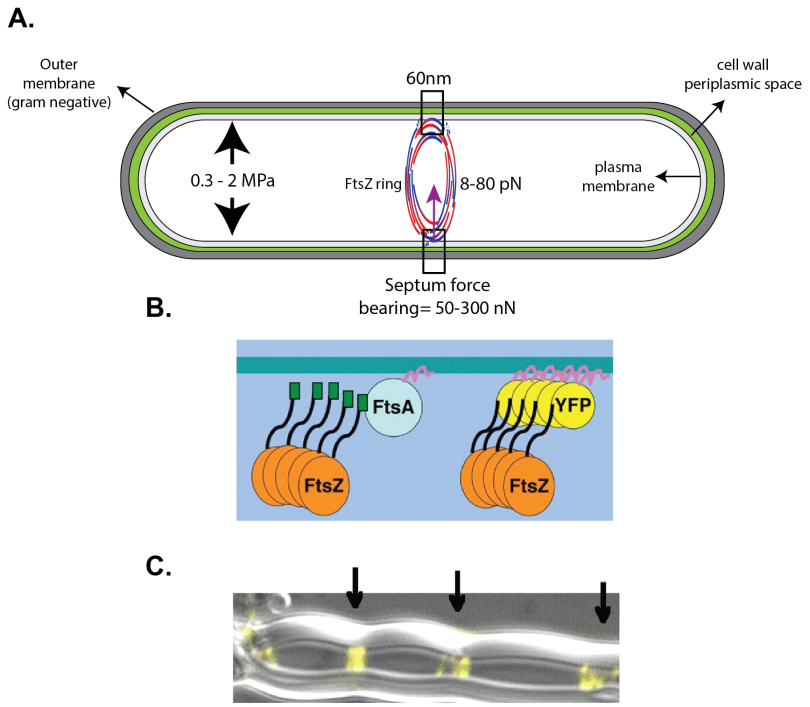

Figure II.3: Bacterial mechanical layout and FtsZ *in vitro* constriction forces. A) Turgor pressure determines the mechanics of bacteria and therefore the force requirements for cytokinesis [116] Bacteria exhibit three different mechanical contributions to bear turgor pressure: i) The cytoplasmatic lipid membrane ii) The peptidoglycan cell wall and iii) (gram-negative) The outer lipid membrane composed mainly of lipopolysaccharides [95]. Recent data highlights the important role of the outer membrane for sustaining the mechanical-load from turgor pressure [87]. B) FtsZ-YFP-mts bypasses FtsA to bind lipid membranes using a membrane targeting sequence. C) When FtsZ is reconstituted inside tubular liposomes, it creates constriction rings.(B and C adapted from [69])

if completely harvested. To study whether FtsZ could exert constriction forces, at least *in vitro*, Erickson and coworkers developed a FtsZ chimera (FtsZ-YFP-mts) that bypasses the natural lipid membrane anchors (FtsA or ZipA) by adding a membrane targeting sequence (mts) (Fig. II.3B) [69]. FtsZ-YFP-mts binds autonomously to membranes using an alpha helix (mts) that MinD uses to bind negatively charged lipids (negatively charged lipids $\sim 30-65\%$ in bacteria). Once FtsZ-YFP-mts is encapsulated in tubular liposomes, it self-assembles into rings that cluster producing constriction (Fig. II.3C) [69]. When FtsZ polymerization is triggered by a GTP analog (GMPCPP), an analog that hydrolyzes at a slower rate, deformations were smaller and less frequent indicating that GTPase activity is related to its ability to deform membranes.

Different models have suggested how FtsZ filaments could generate constriction forces: sliding/condensation [49, 101], bending/conformation changes [3, 41] and intrinsic torsion [40,91]. Torsion has been rarely listed in literature as a possible force mechanism although it has been predicted using all-atom Molecular Dynamic (MD) simulations of FtsZ short polymers [41,91]. Indeed, it explains the formation of FtsZ circular structures ($r \sim 100nm$) over mica (electrically neutral) surfaces [36,57]. Regardless of the model, predictions claim that FtsZ could deliver forces in the range of $8 - 80$ pN. Therefore, the question here is to establish whether this force range could drive cell division against turgor pressure and cell wall mechanical conditions. Addressing this, Lan et al. (2007) have formulated a mathematical model that include cell growth, turgor pressure and cell wall to determine what range of forces could promote septum formation [50]. Interestingly, if there is no growth neither cell wall exchange, forces required would largely exceed predicted FtsZ forces ($\sim$ 400 pN). In contrast, when cell growth and peptidoglycan turn-over is present, forces between $8 - 80$ pN were sufficient to constrict from a diameter of 500 nm to 250 nm [50]. Also, this model reconstructed regular cell-dividing shapes in *E. coli* as well as *B. subtilis*. This model claims that FtsZ indeed could exert a cytokinesis driving force. However, force measurements either *in vitro* or *in vivo* represent a technical challenge and have not been performed so far.

To challenge the "FtsZ-centric" idea, Coltharp et al. (2016) studied the role of FtsZ dynamics and GTPase activity in *E. coli* [18]. Interestingly, none of those parameters affected the constriction rate. Therefore, FtsZ force is not the rate-limiting parameter for constriction. Instead, they observed that the septum closure correlates linearly with cell elongation, which is proportional to the cell wall synthesis rate [18]. This correlation was corroborated by reducing PG synthesis (PBP3) which consequently decreased constriction rates. This evidence agrees with cell division of "L forms" bacteria lacking *ftsZ* gene. Interestingly, cell wall in bacteria can be digested in strains that lack of the *ftsZ* gene; consequently, when *de novo* PG synthesis is induced, cells resume cell division [58]. These results indicate that cell division is achieved in cells that lack of FtsZ but produce PG. Furthermore, microorganisms such as *Chlamydiae* [78] and other species have developed strategies to proliferate without FtsZ [29].

If FtsZ dynamics and GTPase activity do not rule constriction rates, at least *E. coli*, What is the role of FtsZ? As it will be discussed later, Loose and Mitchison (2014) found that FtsZ, *in vitro*, self-assembles into ring-like structures when FtsA anchors FtsZ filaments to

a supported lipid bilayer (SLB) [53]. Strikingly, these swirls treadmill displaying an apparent clockwise rotation. In view of these compelling data, there was the need to determine the existence of *in vivo* FtsZ treadmilling and its function. Accordingly, Bisson-Filho et al. (2017) and Yang et al. (2017) observed FtsZ treadmilling filaments in *B. subtilis* [11] and *E. coli* [117] respectively. Moreover, using GTPase related mutants, they showed that the treadmilling speed scales with the GTPase activity. More interesting, both studies evidenced that FtsZ treadmilling controls spatially and temporally cell wall production. Motion of PBP3 in (*B. subtilis*) and PbP2B in (*E. coli*) PG syntheses synchronizes with FtsZ treadmilling speed [11, 117]. Lastly, FtsZ treadmilling speed regulates constriction rate in *B. subtilis*. In contrast, a reduction in treadmilling speed did not alter the constriction rate in *E. coli*, suggesting presence of an outer membrane [95] require of a different regulation strategy.

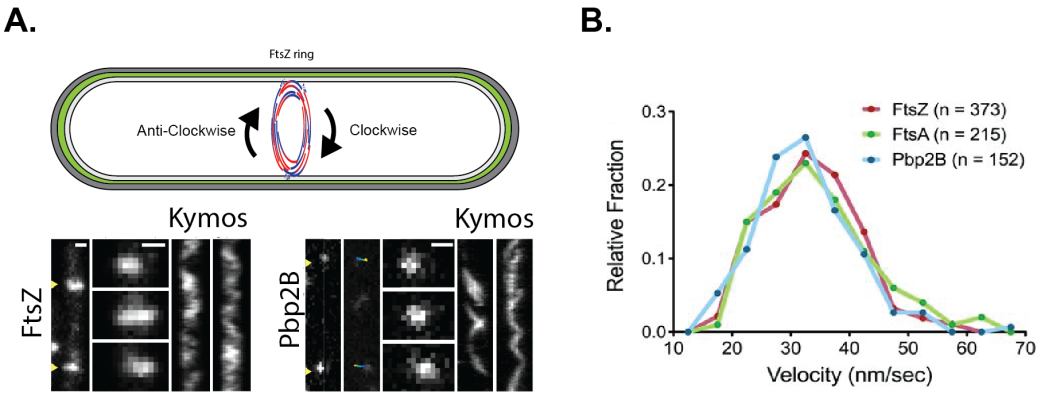

Figure II.4: *In vivo* FtsZ treadmilling in *E coli*. A) Clockwise and anticlockwise circumferential motion of FtsZ/FtsA and Pbp2B displayed in the kymograph analysis (positive and negative slopes in the kymograph) B) FtsZ/FtsA and Pbp2B exhibited the same treadmilling speed distribution indicating that FtsZ directs the Pbp2B motion and therefore PG synthesis. Adapted from [11].

The discovery of FtsZ treadmilling *in vivo* and *in vitro* represented a breakthrough; however, it did not establish the origin of the cytokinesis force [38]. Since new studies proved the coupling between PG synthesis and FtsZ dynamics, the highly localized insertion of PG could, in principle, explain an inwards force that bends the membrane. However, this idea requires of a ratchet-like cell wall synthesis mechanism that has not been observed [73]. Therefore, it seems reasonable to hypothesize that FtsZ locally induce inwards lipid membrane deformations (GTPase activity triggered) that are further stabilized by the insertion of PG material [38]. Arguments favoring this last hypothesis or even the "FtsZ-centric"

idea were recently formulated by Erickson and coworkers [73]. For an FtsZ contractile ring delivering forces in the range of pN, there might not be reason to overcome turgor pressure since periplasmic space might have the same turgor [27], at least in *E. coli*. In addition, if membrane production is coupled to cytokinesis, the excess of lipid area might favor blebbing and decrease the force required for membrane deformations [73]. In conclusion, force measurements of FtsZ are highly relevant to gain a deeper understanding the mechanical role of FtsZ in cell division process.

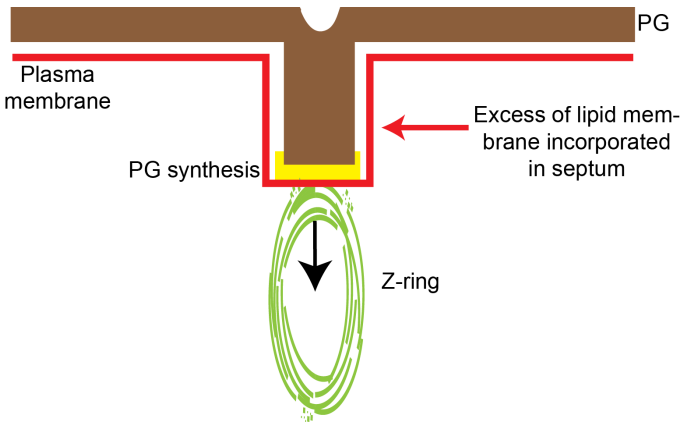

Figure II.5: The treadmilling-driven cytokinesis. Lipid synthesis and membrane excess area could favor the FtsZ local inwards deformations which can be further mechanically stabilized by *in situ* PG synthesis (FtsZ-treadmilling coordinated). Figure adapted from [73]

II.1.3 Imaging *in vitro* FtsZ dynamics on supported lipid bilayers (SLBs) using TIRF microscopy

Numerous *in vitro* studies have revealed, in solution, FtsZ polymerization properties using light scattering or ultra-centrifugation (nicely reviewed in [28]). Using Electron Microscopy (negative stain or CryoEM), these properties have been contrasted to the shape-type of sedimented polymers. Changing buffer conditions or nucleotide-state always affect the obtained polymeric state (mini-rings, straight filaments, helical filaments, bundles, sheets) [28]. Without disregard of these valuable studies, I pretend to highlight studies that have time-resolved *in vitro* FtsZ dynamics, in view of the purpose of this thesis. Mateos-Gil et al. (2012) have pioneered the imaging of single filament dynamics (depolymerization) using time-resolved AFM (Atomic Force Microscopy) [57]. Without the presence of a lipid bilayer,

they have evidenced that closed ring-like structures stochastically open (break) proceeding with fast depolymerization. Interestingly, this depolymerization (mean residence times) depends on the GTPase activity of FtsZ. Posterior work from Loose and Mitchison (2014) [53] have made significant progress for two reasons: i) the use of TIRF-single molecule microscopy to resolve treadmilling dynamics inside FtsZ swirls and ii) the use lipid bilayer as a substrate.

II.1.3.1 TIRF microscopy

Illumination

TIRFM or Total Internal Reflection Fluorescence Microscopy is a -light based- highly convenient technique to study surface events due to its remarkable axial resolution. The method is based on the total internal reflection of light experiencing a change from a higher to a lower refractive index ($\eta_i > \eta_t$). At total internal reflection, an electric field (evanescent field, figure II.6A) with the same excitation wavelength penetrates the lower medium. Since the intensity of the evanescent field decreases exponentially with the distance from the surface, few molecules are consistently illuminated ($\sim$ 100 nanometers above the surface) [31].

To understand deeper this evanescent field, a mathematical description is needed. Light can be described such as oscillating electromagnetic waves, travelling in the propagation direction defined by the wave vector $\boldsymbol{k}$. When these wave fronts reach a transparent interface with different refractive index $\eta_i > \eta_t$, energy will be transmitted as well as reflected. The transmitted wave can be described as [55]:

$$E_t = E_{ot} e^{i(k_t \cdot r - \omega_i t + \varepsilon_t)} \tag{II.1}$$

where ε_t represents a phase induced by the change of medium. Using Snell's laws $\theta_i = \theta_r$ and $\eta_i \sin(\theta_i) = \eta_t \sin(\theta_t)$ (derived from Maxwell's equations), total internal reflection occurs when $\theta_t = \pi/2$ and therefore the critical angle follows the condition: $\sin(\theta_c) = \eta_t/\eta_i$. Using the geometry described in figure II.6B, the component in z of wave vector is described as [55]:

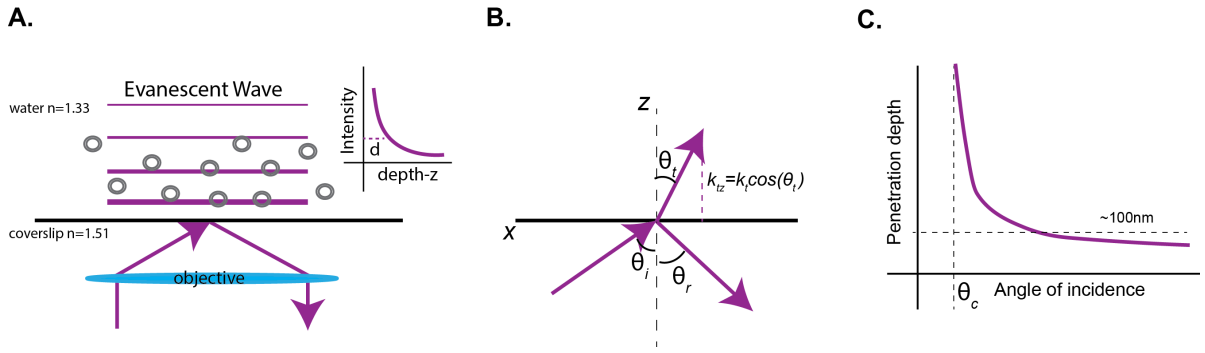

Figure II.6: TIRFM: physical principles A) Objective -based- TIRF: an evanescent wave penetrates the sample at total internal reflection angle θ_c [31]. B) When an incident wave front strike a surface, reflected and transmitted waves follow Snell's law. C) Penetration depth d rapidly decreases by increasing the angle of incidence [55].

$$k_{tz} = k_t \cos(\theta_t) = \pm k_t \left(1 - \frac{\eta_i^2 \sin^2(\theta_i)}{\eta_t^2}\right)^{1/2} \tag{II.2}$$

Since $\sin(\theta_i) > \sin(\theta_c) = \eta_t/\eta_i$, the radical en II.2 becomes < 1. Therefore, equation II.2 follows:

$$k_{tz} = \pm i \left[\frac{k_t}{\eta_t}\left(\eta_i^2 \sin^2(\theta_i) - \eta_t^2\right)^{1/2}\right] = \pm i\zeta \tag{II.3}$$

In view of equation II.3, there is now an explicit expression for the z-dependence of the transmitted electric field ($E_t = E(x,t)e^{-i\zeta z}$) showing exponential decrease when $\eta_i > \eta_c$. In addition, the intensity of an electromagnetic field can be computed since it is proportional to E_t^2. Therefore,

$$I = I_0 e^{-z/d} \tag{II.4}$$

$$d = \frac{\lambda}{4\pi}(\eta_i^2 \sin^2(\theta_i) - \eta_t^2)^{-1/2} \tag{II.5}$$

d decreases (figure II.6C) as θ_i increases and it is independent of the incident light polarization [55].

In practical terms, the critical angle $\theta_i = \sin^{-1}(\eta_{water}/\eta_{glass}) = 61°$ can be achieved using

a high numerical aperture (NA) objective. When light is focused in the back-focal-plane of the objective, light exiting the objective will be parallel to the optical axis (standard epi-illumination). Displacing the xy location of the beam in the back-focal-plane increases θ_i [55]. The maximum value θ_i can be determined using the NA and the refractive index η_m of the objective immersion medium: $NA = \eta_m \sin\alpha$ where α denotes half-angle of the light cone formed by the objective. Since $\sin(\alpha) \leq 1$, an objective having a NA larger than η_{water} might be able to provide TIRF illumination. However, objectives higher than NA= 1.45 are highly desirable. To reach NA$\geq$ 1.45, the immersion medium must have a refractive index $\eta_m \geq 1.45$. As a result, oil immersion objectives are highly used since their refractive index $\eta_{oil} \simeq 1.51$ also matches the refractive index of glass avoiding unwanted reflections [55].

Detection: Fluorescence

As described above, few molecules are illuminated using TIRF and excited at an specific wavelength. The detection of these molecules occurs -*via*- fluorescence. Flourophores (molecules/proteins) absorb single photons and re-emit light at a longer wavelengths [48]. As a result of a photon absorption, a ground-state electron reaches a higher energy state, process characterized by a time scale of 10^{-15} s. This excited electron losses energy due to internal conversion and/or vibrational relaxation in a time scale of $10^{-14} - 10^{-11}$ s. Therefore, the electron returns ($10^{-9} - 10^{-7}$ s) to ground state releasing a photon of lower energy and longer wavelength [93]. Fluorescence phenomenon corresponds only to transitions between singlet (electronic) states (spin paired electrons: multiplicity= 1). In fact, no transitions between states of different multiplicity are allowed; for example, singlet to triplet transition (spin unpaired electrons: multiplicity= 3)). However, an excited singlet state can transition to a lower triplet state in a process called intersystem crossing ($10^{-11} - 10^{-6}$ s) (Fig.II.7A) [48]. In practical terms, triplet states are avoided since decays from the triplet state are non-radiative [48] or they interact with -in solution- oxygen to create reactive oxygen species which degrade flourophores and induce photobleaching [119].

Single molecule imaging requires of a "chemical-fitness" in the process of emitting fluorescence photons. First, the flourophore strength is determined by its cross-section and quantum yield [48]. The cross-section measures the probability of capturing a photon per unit of area [60]. It is proportional to the extinction coefficient ε_p from the Beer-Lambert light absorption law. On the other hand, the quantum yield Φ of a flourophore is the prob-

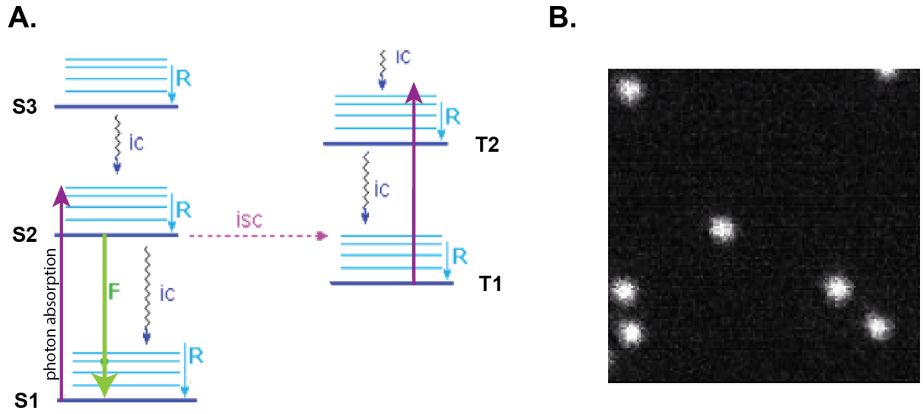

Figure II.7: Jablonski diagram and TIRF single molecule imaging A) The Jablonski diagram describes graphically different transition possibilities after a photon absorption. In fluorescence (F), an electron reaches to a higher energy state and losses partially this energy due to vibrational relaxation (R). Then, the electron returns to ground state emitting a photon of lower energy. B) Single molecule TIRF imaging of GFP-nanobodies crosslinked with ATTO647 dye

ability of emitting a photon after absorption [60]. For example, GFPs (and derivatives) have a quantum efficiency around $\sim 0.6 - 0.7$ [113]. Now, the brightness of a flourophore is defined as: $B = \varepsilon_p \, \Phi$. Although dye performance closely depends on its polar environment [60], brightness results useful parameter to evaluate the quality of a flourophore. In addition, chemical design of dyes owing protection towards oxygen reactive species is determinant for performance. Commercial Alexa or ATTO dyes are well known for their high brightness and low photobleaching.

II.1.3.2 Supported lipid bilayers (SLBs)

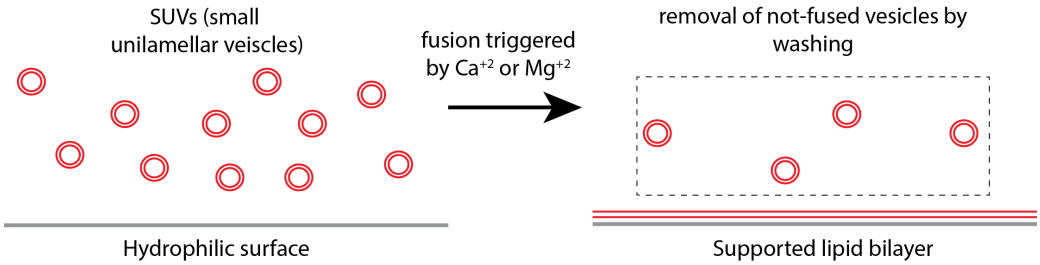

Figure II.8: SLB formation by fusion of SUVs over glass surface

Biological membranes are formed of amphiphilic monomeric units called lipids. Despite

of a detailed-formal description, lipids posses a polar head-group and non-polar oil-like tails. Since polar headgroups interact with water, they might be negatively charged (phosphatidylglycerols (PGs) and cardiolipins (CLs)) such as in bacterial membranes [118]. On the other hand, length and unsaturation levels of hydrophobic tails determine membrane fluidity and packing level [118]. Above the CMC (critical micellar concentration), lipids dissolved in water self-assemble into larger structures due to a competition between energy reduction and gain of entropy (for the lipid ensemble) [12]. The shape of those different structures depend on the lipid shape factor $S = V/(l_{hc}a_0)$ where V is the lipid volume, a_0 the headgroup cross-section and l_{hc} the hydrocarbon chain length. For values between $1/2 < S < 1$ (cylindrical shape), lipids spontaneously form bilayers [12]. Therefore, lipids used in this thesis (*E.coli* extract, EggPC, DOPG) self-assemble into -lipid bilayer made-vesicles once they dissolve in water-like environments. Multilamellar vesicles are further sonicated to reduce their size ($\sim$ 30 nm) and guarantee unilamellarity. For instance, SUVs (small unilamellar vesicles) or LUVs (large unilamellar vesicles) are widely used. In addition, SUVs are prone to fuse (presence of Ca^{+2} and Mg^{2+}) over hydrophilic surfaces such as clean glass or mica, creating a continuous sheet of supported lipid bilayer (SLB) [14].

II.1.3.3 FtsZ reconstitution on SLBs: FtsZ+FtsA self-assemble into dynamic vortices

As mentioned above, pioneering work on FtsZ reconstitution was done by Erickson and coworkers [69]. However, first attempts on SLBs were made by Arumugam et al. (2012) using Erickson's FtsZ-YFP-mts construct (Fig II.3B) [7]. To study the idea of FtsZ binding depending on curvature, flat surfaces (covered with SLBs) were engineered to exhibit curved inwards grooves with curvatures $\leq 1\,\mu m^{-1}$. As expected, FtsZ filaments aligned perpendicular to the groove at curvatures $\sim 1\,\mu m^{-1}$ (Fig.II.9A), compared to flat surfaces with no clear orientation. This indicates that FtsZ filaments are rigid objects with a intrinsic curvature $\sim 1\,\mu m^{-1}$ [7]. In addition, FtsZ coupling with MinCDE "waves" has been studied on SLBs. Using ZipA as FtsZ membrane anchor, Martos et al. (2018) found that MinCDE travelling waves were able to destabilize/depolymerize membrane FtsZ filaments in the wave front, where MinC is maximal (Fig.II.9B) [56]. Although MinC is supposed to interact with FtsZ *via* the c-linker (Fig.II.1A) [94], there is still the possibility that FtsZ+anchor and MinCDE compete for the binding site (here the membrane). In fact, MinDE (without MinC) can also induce dynamic FtsZ-YFP-mts gradients [83].

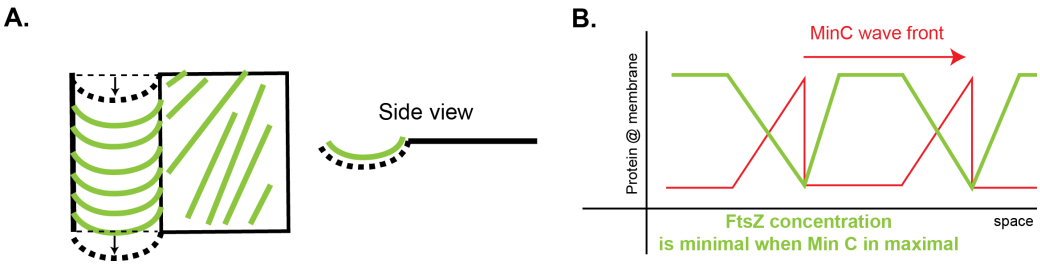

Figure II.9: FtsZ curvature and FtsZ coupling with Min proteins A) FtsZ filaments align perpendicular to the groove at curvatures $\sim 1\,\mu m^{-1}$ [7] B) MinCDE travelling waves were able to destabilize/depolymerize membrane FtsZ filaments in the wave front, where MinC is maximal [56].

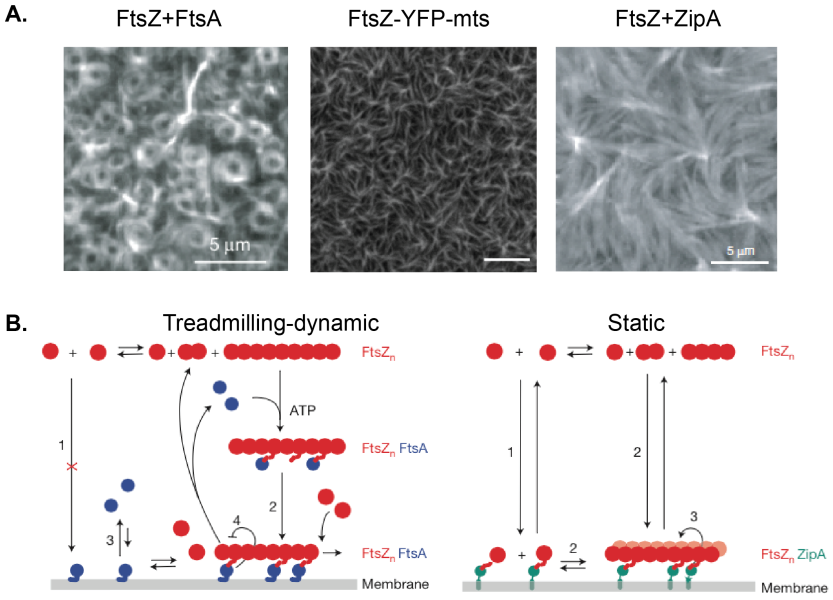

Figure II.10: FtsZ+FtsA self-assemble into dynamic treadmilling vortices. A) Dynamic ring-like structures are only observed when FtsA anchors FtsZ. FtsZ+ZipA and FtsZ-YFP-mts form static networks of filaments. B) The dynamic treadmilling is originated by the dual role of FtsA which i) promotes FtsZ membrane binding as well as ii) dissasembly once the reach the membrane. This negative feedback is absent in FtsZ+ZipA (as well as FtsZ-YFP-mts). Adapted from [53].

About dynamic treadmilling on SLBs, Loose and Mitchison (2014) made a remarkable observation using TIRF microscopy. After purifying the challenging FtsA, they evidenced that FtsZ + FtsA, mixed at a ratio 3:1 ($1.5\mu M$:$0.5\mu M$), self-assembled into dynamic vortices rotating clockwise [53]. Using a lower FtsA concentration, single filaments were observed and their dynamics revealed: polymerization/depolymerization and fragmentation.

Furthermore, single molecule assays showed that monomers do not rotate, as expected for a treadmilling-like phenomenon. On the other hand, using ZipA, 1.5 μM of FtsZ formed a static mesh of longer parallel filaments. Interestingly, adding FtsA to preformed FtsZ filaments (in solution) promoted initial attachment followed by protein detachment. This suggests that FtsA could act as a negative regulator [53]. Consequently, Loose and Mitchison (2014) claimed that the origin of FtsZ dynamics underlies on the dual role of FtsA: i) FtsA binds to in-solution filaments driving them to the membrane; however, ii) FtsA -in the membrane- promotes disassembly and therefore detachment. In contrast, ZipA does not negatively regulate FtsZ filaments and therefore a static network of filaments is observed. [53]. In the same study, an static mesh similar to FtsZ+ZipA was also observed for FtsZ-YFP-mts (1.5 μM).

II.2 FtsZ-YFP-mts self-assembles into dynamic ring-like structures: Treadmilling analysis reveals new insights into dynamic FtsZ ring architecture

The work of this section has been published as:

Ramirez-Diaz, D. A., Garcia-Soriano, D. A.*, Raso, A.*, Mücksch, J., Feingold, M., Rivas, G., Schwille, P. (2018).*

Treadmilling analysis reveals new insights into dynamic FtsZ ring architecture.

PLOS Biology, 16(5), e2004845. https://doi.org/10.1371/journal.pbio.2004845.

* These authors share first authorship on this work

My individual contribution: *(i) I carried out experiments and analysis for the emergence of rings from "nucleation points" (Figure 1). (ii) I implemented long-time lapse imaging to quantify membrane-bound protein density, over time (Figure 2). (iii) I implemented Matlab coding for kymograph-generation and Fourier Analysis for rotational speed measurements (Figure 4). (iv) I performed all single molecule experiments and data analysis (Figure 5). (v) I had a determinant role in "conceptual modelling" (Figure 6) and manuscript-writing.*

II.2.1 Introduction

For the fundamental task of cell and organelle division, life has evolved various strategies, many of which are based on ringlike contractile structures assembling from within a compartment to induce binary fission. The exact mechanisms of contraction of these rings are, however, poorly understood due to the plethora of different molecules involved, concealing presumably simple fundamental motifs. The bacterial FtsZ ring is a good example of such a structure [35, 68]. It interacts with additional anchor proteins to form a dynamic ring at the cytoplasmic membrane, which acts as a scaffold to recruit the remaining regulating elements of the divisome and cell wall-building machinery [20]. Intriguingly, FtsZ filaments were recently found to treadmill circumferentially around the division plane, guiding cell wall synthesis [11, 117]. In spite of this compositional complexity, the primary role of FtsZ in the contractile ring of many organisms is unquestioned. However, based on the structural analysis of the protein and its assemblies, so far, no decisive model has surfaced for how exactly structural changes within monomers and filaments could be transmitted into large-scale contractile forces [86]. Guanosine triphosphate (GTP)-dependent structural changes of FtsZ monomers and membrane-attached filaments toward greater curvatures have been proposed, but evidence has been lacking for how a continuously shrinking membrane orifice could be engineered from them. This is mainly due to the fact that although the closure dynamics of Z rings could be observed in vivo [96, 97],there is yet no direct proof that purified Z rings may actively proceed to closure through all stages of increasing curvature [20, 73].

For membrane attachment, FtsZ requires either FtsA or ZipA. Together they form the so-called proto-ring, the first molecular assembly of the divisome [68, 85]. FtsA is an amphitropic protein that associates to the membrane by an ATP-linked process mediated by a short amphipathic helix [77]. The bitopic membrane protein ZipA contains a short N-terminal region facing toward the periplasmic space, a transmembrane region, and a C-terminal FtsZ-interacting domain connected by a flexible linker region [66]. FtsZ binds the proto-ring tethering elements through its C-terminal end, which is also the interaction region for FtsZ-regulating proteins such as MinC, inhibiting FtsZ polymerization and hence FtsZ ring formation at undesired locations. Thus, the C-terminal region of FtsZ acts as a central hub, integrating signals that modulate divisome assembly in E. coli [68]. The membrane anchor proteins can be bypassed by an FtsZ chimera - FtsZ - yellow flourescent

protein (YFP) - membrane targeting sequence (mts) - through replacing the FtsZ central hub with a YFP and an amphipathic helix to provide autonomous membrane attachment. This mutant was found to become internalized and accumulated in narrow regions of tubular liposomes, forming ringlike structures. Polymerization of this chimeric FtsZ protein at the external face of liposomes has also shown to induce inward or outward deformations, depending on the location of the mts (C-terminus or N-terminus) [69, 70].

Recently, the coreconstitution of FtsZ and FtsA on supported bilayers has revealed that FtsA promotes the self-organization of FtsZ fibers into dynamic patterns, giving rise to coordinated streams and swirling rings with preferential directions, due to treadmilling dynamics [53]. In contrast, this dynamic behavior was not observed when FtsZ was tethered to the membrane through ZipA or when the membrane-targeted FtsZ variant was used. Interestingly, FtsZ - FtsA dynamic vortices showed no apparent change in size and curvature, suggesting that the functional role of the energy-consuming circumferential movement of FtsZ in a ring of apparently conserved radius was a secondary one: i.e., the sequential spatial targeting of downstream enzymes for cell wall assembly. There was further evidence by recent in vivo studies demonstrating the circumferential treadmilling dynamics of FtsZ in dividing cells and directly connecting it to spatial targeting of peptidoglycan synthesis [11, 117]. However, in spite of a wave of new papers targeting the exact role of FtsZ in ring architecture, the current models of how exactly the Z ring is constricting over time, and how the large accessible range of FtsZ filament curvatures may be exploited in this process, are still disappointingly vague.

To study the intrinsic role of FtsZ in the formation of dynamic patterns, we thus revisited the in vitro reconstitution of the membrane-targeted chimeric FtsZ variant, FtsZ-YFP-mts, to flat supported membranes. We further addressed the question whether the pronounced spatial dynamics in FtsZ vortices on the membrane could constitute a direct, rather than indirect, spatial cue in the constriction process of the Z ring. To this end, we compared FtsZ mutants that showed different deformation phenotypes when targeted to free-standing membranes.

Our results can be summarized as follows:

1. In contrast to what was proposed by Loose and Mitchison, the membrane adaptor FtsA is not required for the emergent spatial self-organization dynamics of FtsZ. Its

role can be fully accounted for by an mts to FtsZ.

2. A narrow range of protein concentrations on the membrane, modulated by free Mg^{2+} and dependent on GTP hydrolysis, supports the formation of dynamic FtsZ swirls.

3. Treadmilling results from a directional growth of curved and polar filaments from nucleation points at the membrane. The preferential addition of GTP subunits to the leading edge establishes a GTP - guanosine diphosphate (GDP) gradient along membrane-attached filaments, in which the "older" GDP - rich end is more likely to become destabilized.

4. There is a striking relationship between the vortex chirality of treadmilling and membrane attachment and deformation. FtsZ with C-terminal mts bending the membrane toward the attachment interface treadmills clockwise, while the N-terminal attachment mutant bending the membrane away from the attachment interface treadmills counterclockwise.

II.2.2 Results

Membrane-targeted FtsZ self-organizes into dynamic rotating vortices

The protein chimera FtsZ-YFP-mts (0.5 μM) in its GDP-bound form (corresponding to a nonassembled state, according to sedimentation velocity, S1 Fig) did not form visible structures on a supported lipid membrane, as revealed by a total internal reflection fluorescence microscope (TIRFM). We have found that FtsZ-YFP-mts under assembly-promoting conditions (4 mM GTP, 5 mM Mg^{2+}) formed filaments on supported lipid bilayers (SLBs), which self-organize with time into dynamic ringlike structures (S1 Movie). The assembly of the dynamic rings is a time-dependent phenomenon. After several minutes of GTP addition during which highly dynamic short filaments were observed to attach, detach, and diffuse on the surface longer curved filaments appeared to grow directionally (Fig II.11A panel 5:00). At this stage, intrinsic motion drives filament filament interactions to create small and dim closed circular structures (Fig II.11A panel 15:00). These structures tend to be highly unstable: Closed filaments were able to open, to fuse with adjacent filaments, or to close back. At later times, closed circular strands turned into thicker ringlike structures (Fig II.11A panel 30:00).

To understand the formation of circular structures and how they evolve into stable and thicker rings, we resolved and tracked individual filaments (consisting of several protofilaments) before stable ring formation. Here, we identified nucleation sites where clockwise chiral growth leads to the formation of circular structures (Fig II.11B, S2 Movie). Despite the fact that growth seems to be a discontinuous phenomenon limited by the accessibility of soluble protein, we can estimate a mean growth rate (slope p in the kymograph) which was found to be around 60 nm/s. Strikingly, these images also showed filament flexibility (panels 7-12) and breakage (panels 15-18) resulting in the formation of short free fragments. Such fragments were found to glide and "explore" the surface via treadmilling (Fig II.11C, S3 Movie), indicating that this process fuels filament-filament interactions and therefore ulterior formation of closed circular structures. The kymograph in Fig II.11C showed a representative example of one filament growing in the leading edge (p-line) and shrinking in the trailing edge (d-line). A coarse estimation of the velocity of displacement of this filament was about 55 nm/s.

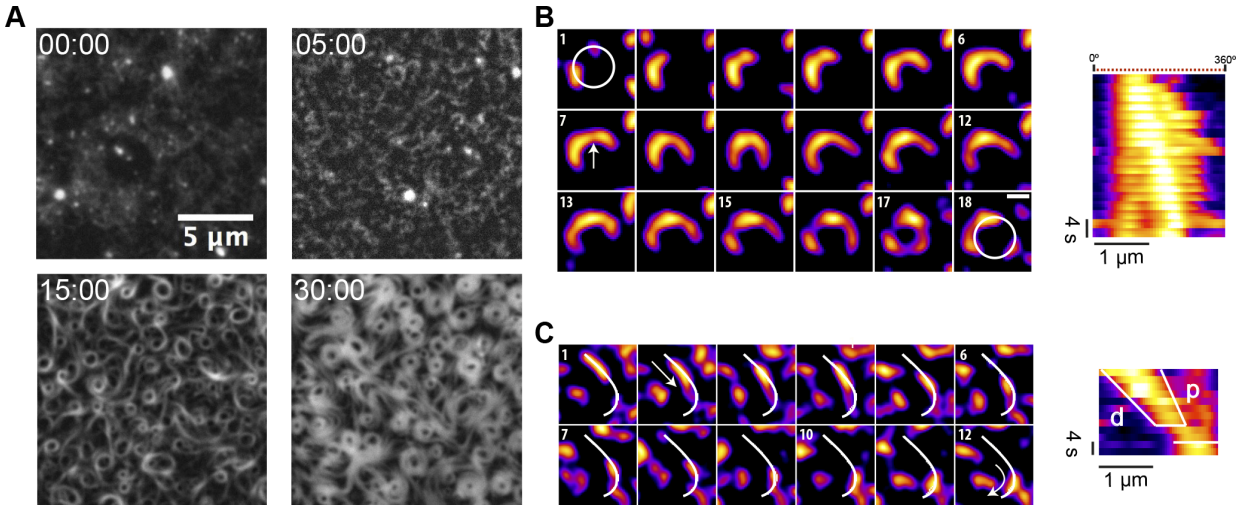

Figure II.11: Nucleation and growth of FtsZ filaments into rings on SLBs. A) Representative snapshots from a time-lapse experiment displaying different stages of ring formation. Images were taken every 10 s using TIRF illumination (YFP channel). Frames correspond to the times (min) indicated after the addition of GTP and Mg^{2+}. (B) Polar clockwise growth of a single FtsZ from a nucleation point. Growth seems to occur stepwise and depend on the accessibility of small filaments nearby (panel 1 and 2). Lower local protein density (white arrow) correlates with a higher flexibility of the polymer (panels 7 - 12). Breakage occurs primarily in trailing regions (15). After about 3 min, a primitive ring made of 3 distinct short filaments is exhibited (17). (C) Directional filament gliding via treadmilling. Fragmentation or depolymerization destabilizes the trailing ("older") edge as shown in the kymograph (d-labeled white line). Images in (B) and (C) were taken every 2 s, and the scale bar represents 500 nm. Further details are under "Results". Movies reconstructed from the whole collection of images can be found in supporting information S2 and S3 Movies. GTP, guanosine triphosphate; SLB, supported lipid bilayer; TIRF, total internal reflection fluorescence; YFP, yellow fluorescent protein.

Surface FtsZ concentration -linked to Mg- critically modulates the emergence of dynamic chiral ringlike structures

We further investigated the impact of protein concentration on the stability and dynamics of FtsZ vortex formation in the presence of GTP (4 mM) and Mg^{2+} (5 mM). Below 0.2 μM, no FtsZ filaments could be detected (S2 Fig). Interestingly, increasing the protein concentration to around 1.0 μM resulted in the formation of abundant three-dimensional polymer networks on the membrane, and no dynamic FtsZ rings were observed (S2 Fig, [53]). These results showed that the self-organization behavior of membrane-targeted FtsZ polymers was critically dependent on total protein concentration.

Next, we compared the kinetics of protein binding to the membrane at 0.2 μM and 0.5 μM of protein (Fig II.12A), under conditions previously used to detect the swirling rings (see Fig II.11). Upon the addition of GTP (4 mM) and Mg^{2+} (5 mM), a similar membrane adsorption rate (Fig II.12A) and the parallel appearance of short and highly dynamic filaments (Fig II.12B) were initially found for the two protein concentrations. Remarkably, the transition from short filaments to rudimentary circular structures (gray area in Fig II.12A) also occurred at similar times in both cases. After a lag time of around 10 min, the adsorption rate was found to be significantly slower at 0.2 μM than at 0.5 μM, suggesting that the kinetics of ring stabilization and widening of the structures was concentration dependent (Fig II.12A). These differences, found at elapsed times greater than 10 min, also correlated with the fact that the morphology of the rings observed at a protein concentration of 0.2 μM after 45 min incubation (Fig 2B, bottom right panel) was similar to the ones obtained after a lag time of 20 min when 0.5 μM protein was used (Fig II.12B, upper mid panel). The morphological similarity found at these two time points (denoted as 2 and 3 in Fig II.12A) occurred at a similar protein coverage of the membrane, suggesting that protein surface density, rather than bulk concentration, is the key parameter determining the nature of the network that assembles on the membrane. The correlation between the morphologies at time points 2 and 3 of Fig 2A was further established by determining the average diameter of the formed rings to be about 1 μm at both protein concentrations (Fig II.12B). This suggests that although the adsorption rates were different at these time points, the proteins condensed into similar structures.

Then, we monitored the impact of GTP concentration (0.04, 0.4, and 4 mM) on the formation of swirling vortices at fixed protein (0.2 μM) and Mg^{2+} (5 mM) concentration. Sur-

prisingly, at the lowest GTP assayed (0.04 mM), a highly ordered mesh of static filaments was found at t = 0. These filaments retained a certain degree of curvature and behaved as a nematic phase that entirely covered the membrane area (Fig II.13, left panel). A similar behavior was also observed at intermediate GTP concentration (0.4 mM) (S3 Fig). Notably, the surface mean intensity is 3-fold (approximately 1,500) increased, compared to the minimal density to form rings (Fig II.12), suggesting that the parallel arrangement of filaments correlates with a high-density regime of protein. Furthermore, aligned filaments showed no significant change after 10 min, in contrast to dynamic rings (S3 Fig).

Directionality of vortices and destabilization of the trailing edge

After formation, single rings reach a quasi-steady state as rotating vortices, meaning that the light intensity along their perimeter shows a nearly periodic time dependence. These rotating structures formed by the membrane-targeted FtsZ-YFP-mts (mts C-terminal) consistently showed a chiral clockwise rotation (Fig II.14A and S4 Movie). The directional ring dynamics were confirmed by the positive slope of kymographs generated along the ring circumference. Quantifying the slope of the kymograph (see Materials and methods and S4 Fig) of N = 60 rings, we calculated the velocity distribution with a mean velocity of 34 nm/s or 3.9 $^{\circ}s^{-1}$ for rings of about 500 nm radius (Fig II.14D). Interestingly, the rotational velocities measured here are in good agreement with those reported in vivo (30 nm/s), in spite of the significantly reduced complexity of the reconstituted system [11,117].

We next sought to understand whether there was any relationship between the structural features of the protein and the obviously chiral dynamics of our FtsZ mutants. Hence, we made use of a previously established chimera variant that was shown to have opposite effects on deformable membranes [7,70]. In the presence of GTP, FtsZ-YFP-mts is able to induce inward (concave) deformations on lipid vesicles. Strikingly, when the mts sequence is switched to the N-terminus, an outward (convex) deformation is observed [70]. To study the role of the position of the mts in our dynamic vortices, we carried out similar self-organization assays using an FtsZ chimera in which the membrane attachment was located at the opposite -the N-terminal-end (mts-H-FtsZ-YFP). Upon addition of GTP and Mg^{2+}, defined dynamic rings were observed (Fig II.14B). Strikingly, now the FtsZ swirls appeared to rotate counterclockwise (S4 Movie), a feature that was confirmed by the negative slope of the kymographs (Fig II.14B). As before, we measured the slope of kymographs for N = 50 different rings to calculate the velocity distribution with a mean of about 25 nm/s

or 2.8 $^{\circ}s^{-1}$ for a ring of 500 nm radius. This velocity is slower than that of the FtsZ-YFP-mts vortices (34 nm/s) (Fig II.14D). These observations show that the positioning of the mts determines the direction of polymerization, as it does for membrane binding and transformation. The fact that the N-terminal mts mutant -without a protein spacer between the FtsZ and the membrane attachment- results in the same qualitative dynamic behavior, although being inverted in chirality, also refutes potential speculations that YFP may take over a necessary (sterical) role of FtsA [53].

To further investigate how exactly GTP hydrolysis influences the formation of collective streams, we carried out similar self-organization assays using a variant of the FtsZ chimera with no GTPase activity (S5 Fig), in which the Threonine at position 108 was replaced by an Alanine (FtsZ*[T108A]-YFP-mts). Well-defined rings similar in size to the ones found with FtsZ-YFP-mts could be observed upon the addition of GTP and Mg^{2+} (Fig II.14C). Interestingly, these rings did not seem to treadmill and rotate (S4 Movie), as evidenced by the lack of clear patterns in the kymographs generated to track polymer dynamics (Fig II.14C). Interestingly, FtsZ*[T108A]-YFP-mts rings grow from nucleation points in a less dynamic manner compared to FtsZ-YFP-mts (S5 Movie). From these results, we conclude that GTPase activity is not required for the formation but for the quasi-steady-state rotational dynamics of the ring patterns, suggesting that GTPase activity particularly promotes filament destabilization in the trailing edge.

Treadmilling can be explained by an imbalance between growth and shrinkage at the two opposite ends of the polar filament. Since treadmilling is obviously GTP-turnover dependent, and the growth into ring like structures by capturing preformed diffusing filaments is not, the critical requirement for treadmilling seems to be the destabilization and shrinkage at the trailing edge. In order to directly visualize the destabilization dependent on nucleotide state, we developed a single molecule assay using FtsZ-YFP-mts incubated with fluorescently labeled nanobodies (green fluorescent protein [GFP]-Booster-Atto647N, see Materials and methods) (Fig II.15A) to investigate the protein turnover at the membrane, implying that faster disassembly suggests higher destabilization. By measuring the probability of protein detachment as a function of time (S6 Fig), we could calculate the mean residence time of single FtsZ subunits within the filaments on the membrane. Using this analysis, we found that the mean residence time of FtsZ-YFP-mts in fragments forming dynamic rings was (Fig II.15B), in good agreement with previous fluorescence recovery after photobleaching (FRAP) studies with native FtsZ [4, 16]. This residence time turns

out to be significantly faster than for the GTP hydrolysis-deficient mutant FtsZ*[T108A]-YFP-mts (S6 Fig, similar to the photobleaching time scale contribution approximately 32 s). By considering the rotational speed as measured in Fig II.14D and this residence time, we reason that rings are assembled by multiple filaments that treadmill in a synchronized manner, with a mean length of $\langle l \rangle = \bar{v} t_{res}$ (78 monomers). In comparison, in vitro assembly of native FtsZ showed shorter filaments that were, on average, 120 to 200 nm long (30-50 monomers) [16,42]. In addition, we measured the residence time without GTP (GDP form) with 1 mM free Mg^{2+}. Assuming that the residence time of a polymer of n-monomers scales to the power of n $t_r^{pol} \sim (t_r^{mon})^n$, one can estimate that the residence time associated to one monomer is approximately 1 s, which agrees with our results (approximately 0.8 s) in GDP form at 1 mM free Mg^{2+}.

Our single molecule experiments also allowed us to directly elucidate the impact of free Mg^{2+} and, in particular, its obvious role in the formation of the high-density FtsZ mesh. It was found that the protein release from the membrane upon GTP addition was slower at 5 mM (t_r=15.1 s) than at 1 mM free Mg^{2+} (Fig 5II.15). These findings represent compelling evidence that the formation of a high-density mesh of filaments is linked to the slow detachment of protein, at least when compared to the dynamic rings at lower free Mg^{2+} (1 mM). Also, the residence time of FtsZ in GDP form at 5 mM free Mg^{2+} was increased (t_r=1.72 s) compared to 1 mM. This general increase in the residence time implies that lateral interactions (bundling), favored by free Mg^{2+}, promote larger and more crosslinked polymeric species with higher membrane affinity and less susceptibility to destabilization.

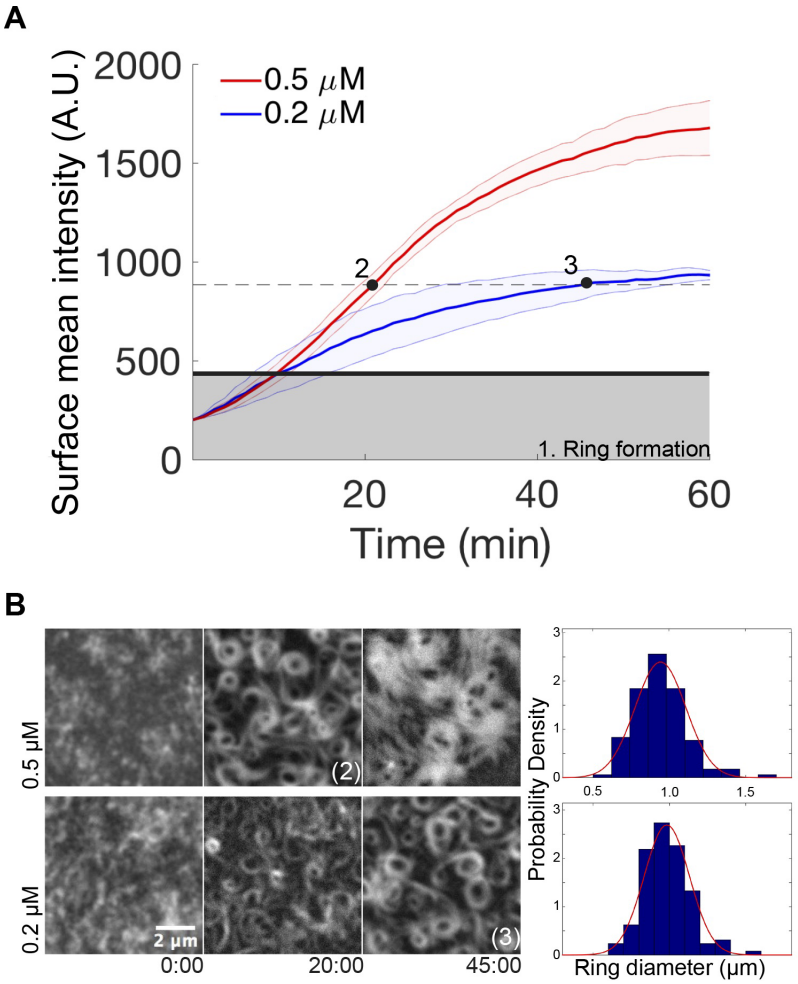

Figure II.12: Dependence of FtsZ-YFP-mts vortex formation on protein surface concentration. (A) Time dependence of the average fluorescence intensity of FtsZ-YFP-mts on the bilayer upon 4 mM GTP and 5 mM Mg^{2+} addition, as measured by TIRFM, at 0.2 (blue line) and 0.5 (red line) μM protein concentration. The gray area marks the intensity when first closed rings are observed, which is approximately the same for both protein concentrations. After closed rings have formed, the further accumulation of protein at the surface is strongly concentration dependent. The dashed line represents the phase in which clearly discernible, locally stable dynamic vortices are observed. While at 0.2 μM, the system reaches this regime after an elapsed time of 45 min (time point 3); at 0.5 μM, it only takes approximately 20 min (time point 2). (B) Representative images of the experiment shown in panel (A). Frames were taken at elapsed times in minutes. Right: Ring size distributions at time points 2 and 3, indicated in panel (A), with average diameters of 0.94 ± 0.16 Îijm, N = 140, and 0.98 ± 0.14 Îijm, N = 128, respectively. Size distributions of rings are similar since both correspond to the same protein surface density (approximately 880 A.U.) Further details are under "Results". A.U., arbitrary units; GTP, guanosine triphosphate; mts, membrane-targeting sequence; TIRFM, total internal reflection fluorescence microscope; YFP, yellow fluorescent protein.

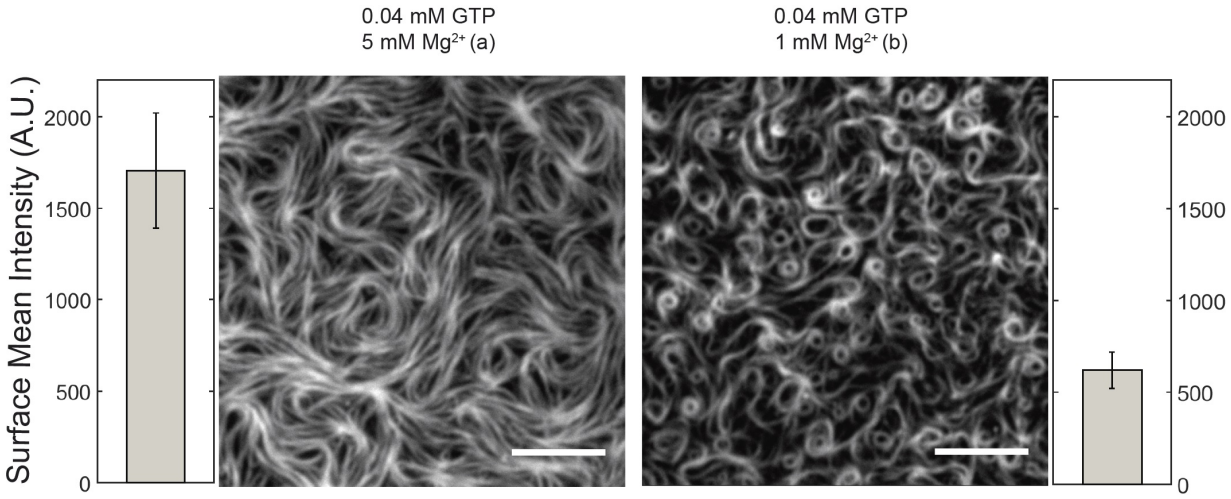

Figure II.13: Free Mg^{2+} regulates protein surface concentration and thus self-organization of membrane-targeted GTP-FtsZ. Representative snapshots showing TIRFM images of FtsZ-YFP-mts (0.2 μM) polymers on the bilayer taken 2-3 min after the addition of 0.04 mM GTP in the presence of 1 mM and 5 mM free Mg^{2+} concentrations, respectively. Next to each image, the mean fluorescence intensity, proportional to the FtsZ-YFP-mts density on the membrane, is shown (average of 3 experiments). The protein network observed at 5 mM free Mg^{2+} correlates with a high FtsZ-YFP-mts density regime, at least 3-fold larger (approximately 1,500 A.U.) than required for ring formation (approximately 500 A.U.) The scale bar represents 5 μM. A.U., arbitrary units; GTP, guanosine triphosphate; mts, membrane-targeting sequence; TIRFM, total internal reflection fluorescence microscope; YFP, yellow fluorescent protein.

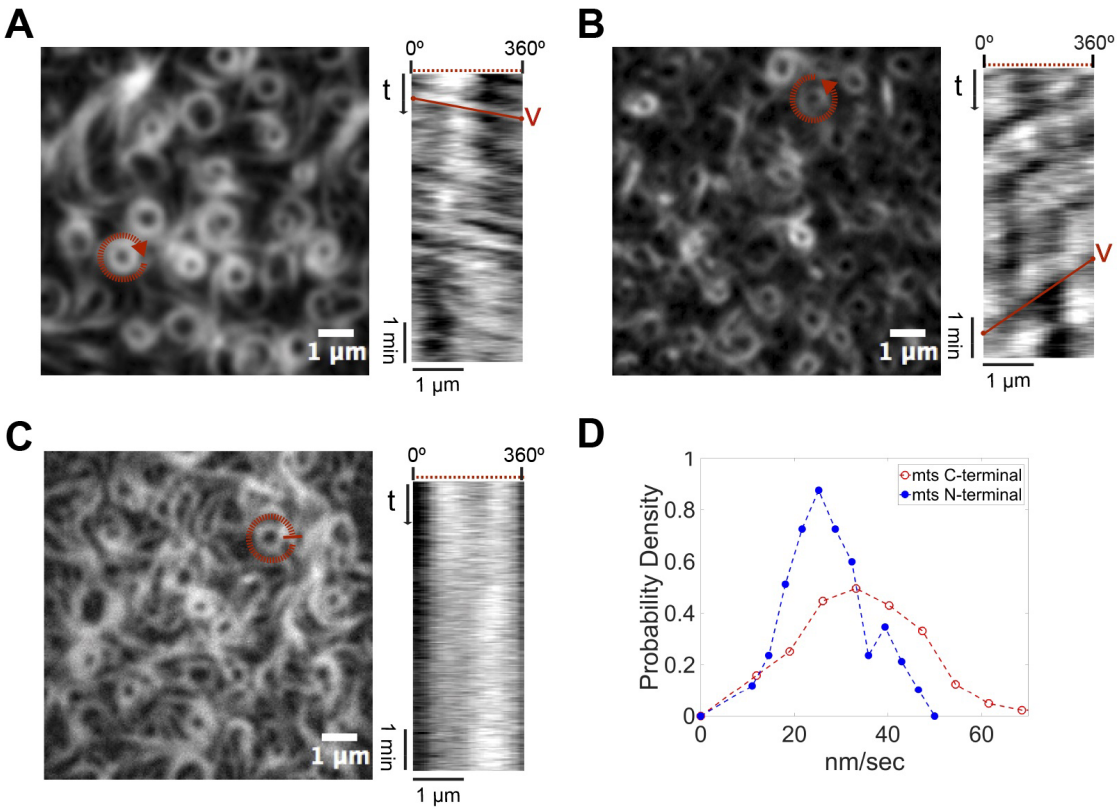

Figure II.14: Steady-state treadmilling and chirality of FtsZ vortices: Dependence on GTPase activity and location of the mts. (A-C) Left panels: Representative snapshots of the rings formed upon addition of GTP (4 mM) and Mg^{2+} (5 mM) by (A) FtsZ-YFP-mts, whose mts is located at the C-terminus of FtsZ; (B) mts-H-FtsZ-YFP, with mts located at the N-terminus of FtsZ; and (C) FtsZ*[T108A]-YFP-mts, a variant of FtsZ-mts with diminished GTPase activity. Right panels: Kymograph analysis showing (A) a positive slope that corresponds to the apparent clockwise rotation time of the selected ring (red circle); (B) a negative slope that corresponds to an apparent counterclockwise rotation, indicating that the position of the mts determines the chirality of the apparent rotation; (C) no apparent slope corresponding to static rings, suggesting that the apparent rotation in (A) and (B) is mediated by GTP hydrolysis. (D) Velocity distributions for FtsZ-YFP-mts (red) and mts-H-FtsZ-YFP (blue) with mean rotational speed values of 34 nm/s and 25 nm/s, respectively. Further details under Materials and methods and Results. GTP, guanosine triphosphate; mts, membrane targeting sequence; YFP, yellow fluorescent protein.

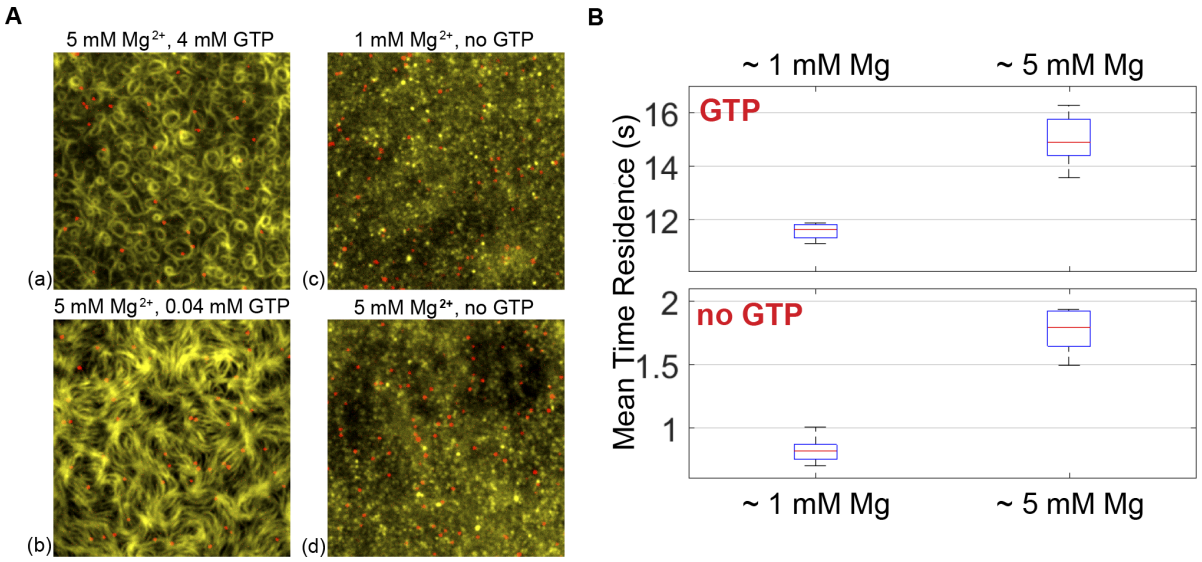

Figure II.15: Residence times of single membrane-targeted FtsZ molecules at the bilayer, dependent on nucleotide and free Mg^{2+}. (A) Overlaid images of FtsZ-YFP-mts structures (yellow channel) incubated with GFP-Booster-Atto647N (nanobody) (single molecules: red channel) in the presence of GTP (a, b), GDP (c, d), and indicated free Mg^{2+} concentration. The protein concentration in all cases was around 0.2 μM. (B) Mean residence times of FtsZ-YFP-mts were calculated using an exponential fit of the cumulative residence time distribution. Mean residence times were measured for different GTP and Mg^{2+} conditions. Further details under Materials and methods and Results. GDP, guanosine diphosphate; GFP, green fluorescent protein; GTP, guanosine triphosphate; mts, membrane targeting sequence; YFP, yellow fluorescent protein.

II.2.3 Discussion

In our minimalistic in vitro reconstitution study, we found that polymers of an artificially membrane-targeted variant of FtsZ autonomously and without the presence of FtsA self-organize on a supported bilayer upon addition of GTP and Mg^{2+} to form chiral ring like dynamic patterns (Fig II.12), displaying a clockwise or counterclockwise protein movement, dependent on whether the membrane attachment was enforced through the C-terminal or N-terminal end of the protein, respectively (Fig II.14A and II.14B). The mts in both cases was taken from MinD, one of the elements of the site-selection MinCDE complex, which allows FtsZ to be peripherally attached to the membrane. We thus showed that the ability of FtsZ to create dynamic patterns is an intrinsic property (Fig II.12A) rather than a specific interaction with a specific protein anchor. Instead, the formation of dynamic FtsZ ring structures in vitro is highly linked to (i) the surface protein density and (ii) GTPase activity, destabilizing surface-bound filaments and thus being key for treadmilling [117].

We found that the most decisive factor for the emergence of dynamic vortices of FtsZ on membranes is the overall surface coverage by protein monomers and filaments (Fig II.16A), which varies over time upon protein adsorption to the membrane (Fig II.12) and is controlled by free Mg^{2+} concentration (Fig II.13). Dynamic vortices appear primarily in an intermediate density regime (surface mean intensity: 450-1,000 arbitrary units A.U.) and isotropic bundles in a high-density regime (surface mean intensity $>$ 1,000 A.U.). Transitions from highly dynamic vortices to isotropic bundles occur upon an increase in lateral contacts that arrest treadmilling filaments, increasing their mean effective length (as in the case of ZipA [53]). This was clearly observed in our single molecule assay (Fig II.15B) that shows a slower turnover in the situation of dense isotropic bundles, i.e., longer filaments. Along these lines, the increase in lateral interactions at high free Mg^{2+} also explains the rapid formation of filaments at 5 mM free Mg^{2+} (Fig II.13), since larger FtsZ assemblies bind to the membrane and interact with each other more frequently (Fig II.15B). Presumably, the main reason why Loose and Mitchison failed to observe dynamic vortices in the case of the FtsZ-YFP-mts [53] is because of the high protein concentration used in their experiments (1.5 μM).

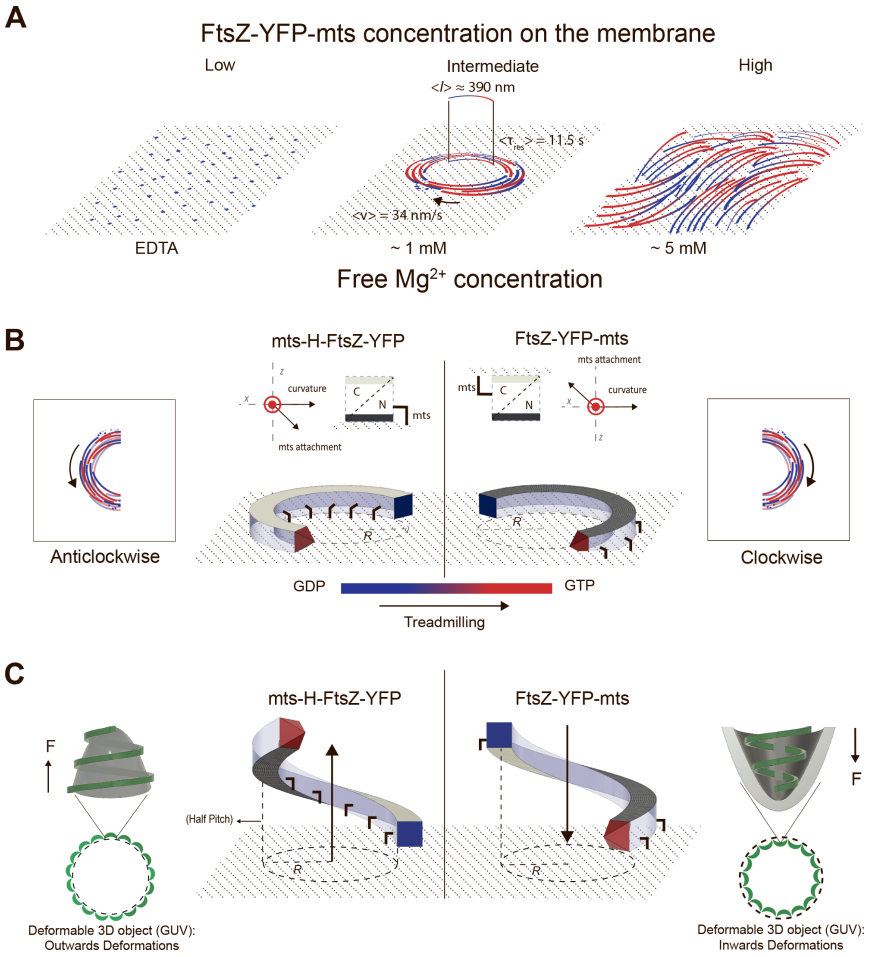

Figure II.16: (A) FtsZ-YFP-mts ring formation is dependent on GTP and protein surface concentration. At low protein concentration and no GTP and Mg^{2+}, FtsZ transiently binds to the membrane without forming visible structures. With GTP, dynamic chiral rings are formed as a function of time. Once stable swirls are built, they exhibit a mean velocity of 34 nm/s and a turnover time of short fragments of 11.5 s. From the velocity and the turnover time, the average length of the protofilaments can be estimated to 390 nm. However, ring formation is only observed at intermediate protein density regimes. At high protein density, a parallel network of filaments (nematic phase) is observed. (B) To guarantee chirality, attachment needs to have a perpendicular component to both the ring curvature and filament polarity to have a preferential binding face. In this case, the mts interacts with the flat surface on opposite sides of the FtsZ filament, so curvature is also in the opposite direction. (C) We here suggest that an intrinsic helical FtsZ shape, characterized by a radius and a pitch, can alternatively explain previous FtsZ-induced inwards/outwards deformations in the following way: Due to the intrinsic pitch, the growing filament would either pull up (left) or push down (right) the surface. On the contrary, if the surface is not deformable (SLB), the filament would experience a strain, get destabilized, and eventually break upon growth. GDP, guanosine diphosphate; GTP, guanosine triphosphate; GUV, giant unilamellar vesicles; mts, membrane targeting sequence; SLB, supported lipid bilayer; YFP, yellow fluorescent protein.

Our results are compatible with previous atomic force microscopy analysis of static structures formed by FtsZ polymers on mica as a function of protein concentration at the surface [59]. The protein concentration-dependent formation of dynamic FtsZ patterns also nicely correlates with a recent theoretical study suggesting that protein density at the membrane controls the formation of vortex patterns on membranes in a phase-like behavior. According to this, independent curved polar filaments showing chiral motion and repulsion can self-assemble into vortex or ring like structures in an intermediate density regime. While at low protein densities filaments travel independently, at the high-density regime they form isotropic networks and jammed bundles [22].

By gradually increasing protein concentration on the membrane, we were able to investigate the initial formation phase of dynamic rings. At low density (surface mean intensity < 450 A.U.), curved and polar filaments initially emerge from nucleation points, which presumably are small attached filaments above a critical length. Intriguingly, the overall adsorption rates to the membrane at this stage are similar for protein concentrations of 0.2 $\mu M$and 0.5 μM (Fig II.12A). Upon sufficiently high membrane coverage of nucleating filaments after the initial phase, protein binding from solution begins to scale with total (i.e., bulk) protein concentration. Whether nucleators are directly formed on the membrane after GTP addition or whether short polymers are formed in solution and an increase in affinity with growth brings them to the membrane cannot be determined based on our data and will be the topic of further investigation.

We found that filaments growing from nucleators are prone to fragmentation, resulting in free fragments that may stay connected to the membrane. There, they assemble with other attached filaments by diffusion and directional treadmilling, which ultimately results in closed rings in which the treadmilling continues. Our experiments demonstrate that treadmilling, particularly via destabilization of the trailing edge, is highly regulated by GTPase activity. When GTPase activity is switched off (FtsZ*[T108A]-YFP-mts), rings seemed to grow only from nucleation points and do not treadmill, at least on time scales found for FtsZ-YFP-mts (Fig II.14C). Moreover, the residence time of single FtsZ*[T108A]-YFP-mts subunits in the filaments is comparable with the photobleaching control, implying that protein turnover is almost nonexistent (S6 Fig). It has been suggested that a kinetic and structural polarity at monomeric level and a GTP/GDP gradient are requirements for robust treadmilling [111]. As seen from our experiments of the initial vortex growth phase, a GTP/GDP gradient along the treadmilling direction is likely to result from the

preferential addition of GTP subunits to the existing filaments at the polar front and a more likely GTP turnover toward the "older" tail

.

In light of the role of GTPase activity for the formation of dynamic vortices, the measured velocity of the FtsZ + FtsA vortices reported by Loose and Mitchison is about 3-fold faster (108 nm/s) compared to our FtsZ-YFP-mts rings (34 nm/s). In addition, these authors reported a higher GTPase activity of the FtsZ + FtsA compared to the FtsZ-YFP-mts [53]. Nonetheless, it is not clear how variables such as GTPase activity and attachment strength influence the speed of rotation. For instance, our mutant mts-H-FtsZ-YFP has shown a considerable decrease in rotation speed compared to the FtsZ-YFP-mts. Remarkably, to observe mts-H-FtsZ-YFP dynamic rings, we had to increase the bulk concentration to 1.25 μM. This may be due to a reduced affinity for membranes, affecting the overall dynamics.

The most remarkable outcome of this study is the clear dependence of vortex chirality on the positioning of the membrane anchor, which, in turn, has severe effects on the topology of membrane deformation by FtsZ. Chirality is inverted by switching the membrane anchor from the C-terminus (clockwise) to the N-terminus (counterclockwise). Intriguingly, these two different mutants cause concave (C-terminal) or convex (N-terminal) deformations when bound to deformable liposomes [70]. To explain these different deformations, Erickson and colleagues have previously depicted FtsZ filaments as arc segments with a direction of membrane attachment either parallel or antiparallel to the vector of curvature. In order to support the here-observed chiral treadmilling of curved rings on planar membranes, however, attachment through the preferential binding face of the filaments needs to have a perpendicular component to both the ring curvature and filament polarity. Fig II.16B shows a curved filament with a C-terminal (clear gray) and N-terminal (dark gray) face perpendicular to the curvature of the filament. Note that the mts is represented here with one parallel component to the curvature, as suggested by Erickson, and one perpendicular component to accommodate flat membrane binding. In this flat representation of a curved FtsZ filament, treadmilling is explained by a polar growth at the leading edge and a destabilization mechanism, driven by GTP hydrolysis, toward the GDP-enriched region at the trailing edge [111].

Therefore, in light of evidence showing that FtsZ forms helical structures in vivo [33, 39, 65, 103] and in vitro [7], we here suggest an alternative structural model to the one

depicted in Fig II.16B (Fig II.16C). We propose that an FtsZ filament with more than one main direction of curvature, such as a helix, would much more elegantly accommodate the combination of inward/outward deformations and chiral treadmilling for the opposite mts mutants. Such a corkscrew-like FtsZ filament can be simply described by an intrinsic radius and a pitch, in which the latter would reflect on the attachment direction (Fig II.16C). On a deformable surface (deflated liposome), the growing filament would either pull up (left) or push down (right) the surface due to the respective pitch. The interplay between the elastic response of the membrane (increased membrane tension) and local changes in the helix radius due to GTP hydrolysis [43, 54] could explain the stabilization of higher curvature or smaller radii regions (Fig II.16C). On a non-deformable surface (SLB), however, since the surface is not resilient, the filament would experience a strain, get destabilized, and eventually break upon growth.

Thus, together with the very recent studies showing the linkage between treadmilling of FtsZ polymers and peptidoglycan synthesis in E. coli [117] and B. subtilis [11] cells, our findings shed new light on the interplay between FtsZ structure and treadmilling dynamics but may also hint to a direct mechanical link of these to bacterial division. The minimal system we used unambiguously shows that the observed chiral vortices are the result of intrinsic GTP-linked FtsZ polymerization dynamics on the membrane without the need of additional complex interactions with FtsA and ATP, pointing to a fascinating archetypal feature of this important structural protein. The reduced number of components allowed us to selectively determine the influence of key factors -e.g., the surface density of FtsZ- on the self-organization behavior, thus contributing to a much better mechanistic understanding of FtsZ's dynamic architecture and its potential physiological implications.

II.2.4 Materials and methods

Mutants

Mutations in ftsZ-YFP-mts were constructed using site-directed mutagenesis. FW oligonucleotide was designed using the NEBaseChanger-Substitution. RV oligonucleotide was obtained from the reverser complement sequence of the FW oligonucleotide. Oligonucleotides

$$5' - GGTGGTGGTGCCGGTACAGGT - 3'$$

and

$$5 - ACCTGTACCGGCACCACCACC - 3'$$

were used to generate FtsZ-YFP-mts-T108A mutant by replacing a Thr in position 108 by an Ala. Briefly, FtsZ-YFP-mts was first amplified using the FW and RV oligonucleotides in different PCR reactions, testing 3 different temperatures: 54°C, 58.5°C, and 65°C. In a second PCR reaction, the PCR products from the FW and RV oligonucleotides were mixed; also, 3 different temperatures were tested: 54°C, 58.5°C, and 65°C. After digestion with DpnI, the 3 PCR products were used to transform CH3-Blue competent cells. Five colonies were picked for DNA extraction and selected for sequencing.

Protein purification

The FtsZ-YFP-mts, FtsZ*[T108A]-YFP-mts, and mts-H-FtsZ-YFP were purified as previously described [71]. Briefly, the protein was expressed from a pET-11b expression vector and transformed into E. coli strain BL21. ON overexpression was performed at 20°C for the proteins FtsZ-YFP-mts and FtsZ*[T108A]-YFP-mts and at 37°C for protein mts-H-FtsZ-YFP. Cells were lysed by sonication and separated by centrifugation. Then, protein was precipitated from the supernatant, adding 30% ammonium sulphate and incubating the mixture for 20 min on ice (slow shaking). After centrifugation and resuspension of the pellet, the protein was purified by anion exchange chromatography using a 5 x 5 ml Hi-Trap Q-Sepharose column (GE Healthcare, 17515601). Purity of the protein was confirmed by SDS-PAGE and mass spectrometry.

Small unilamellar vesicles (SUVs)

E. coli polar lipid extract (Avanti, AL, United States), initially dissolved in chloroform, was desiccated under a gas nitrogen stream. Chloroform traces were further removed by 1-h vacuum. This lipid film was hydrated with SLB-buffer (50 mM Tris-HCl, 150 mM KCl, pH 7.5) to reach a lipid concentration of 4 mg/ml. After 10 min sonication, SUVs were obtained.

SLBs

Glass coverslips 1.5 (Menzel, Germany) were cleaned in air plasma. Then, a plastic chamber was attached on a cleaned glass coverslip using ultraviolet-curable glue (Norland Optical Adhesive 63). SLBs were obtained by the method of vesicle fusion from SUVs on a glass

surface as described elsewhere [14]. The SUV dispersion was diluted in SLB buffer (50 mM Tris-HCl at pH 7.5, 150 mM KCl) to 0.5 mg/ml, of which 75 μl was added to the reaction chamber. Adding $CaCl_2$ to a final concentration of 2 mM promoted vesicle fusion and the formation of a lipid bilayer on the glass. The samples were incubated at 38°C for 20 min and then washed with prewarmed SLB buffer to remove nonfused vesicles. Lastly, a washing step with the reaction buffer (50 mM Tris-HCl at pH 7.5, 150 mM KCl and $MgCl^{2+}$ [5 mM or 1 mM]) was carried out in the sample.

Self-organization assays

FtsZ-YFP-mts or FtsZ-YFP-mts mutants were added to the reaction buffer above the supported lipid membrane in the chamber. The final volume of the samples was approximately 200 μl. FtsZ-YFP-mts was added to a final concentration of 0.5 μM or 0.2 μM. Polymerization was induced by adding GTP to a final concentration between 0.04 and 4 mM, as indicated in the text.

TIRFM imaging

All experiments were performed on a WF1 GE DeltaVision Elite TIRFM (GE Healthcare Life Sciences, Germany) equipped with an OLYMPUS 100X TIRF objective (NA 1.49). The UltimateFocus feature of DeltaVision Elite maintains the focus plane constant in time. FtsZ-YFP-mts was excited with a 488 nm diode laser (10 mW, before objective) Fluorescence imaging is performed using a standard FITC filter set. Images were acquired with a PCO sCMOS 5.5 camera (PCO, Germany) controlled by the softWoRx Software (GE Healthcare Life Sciences, Germany). For time-lapse experiments, images were acquired every 3 or 10 s, with a 0.05 s exposure time, with light illumination shuttered between acquisitions.

Image analysis and processing

Image analysis was carried out in MATLAB 2015 (MATLAB and Image Processing and Computer Vision Toolbox Release 2015a, The MathWorks, Inc., Natick, Massachusetts, USA) and processing with Fiji/ImageJ (Rasband, W. S., ImageJ, US National Institutes of Health, Bethesda, 1997-2007). Images correspond to an average of 5-10 frames from a time-series experiment. For the kymograph analysis, time-series acquisitions were filtered using a standard mean filter and were drift corrected (Image J). A MATLAB script allows the

user to define a ring by providing 2 coordinates. Every ring is automatically fitted to a circle with radius r. Then, 3 trajectories corresponding to 3 concentric circles having radii r, $r+1$, and $r-1$ pixels are determined. At this point, the script will read the time-series data and calculate a kymograph for each time point and trajectory. The final kymograph corresponds to the average of the 3 different trajectories. To automatically calculate the slope, we first smooth the kymograph with a Savitzky-Golay filter of order 2 and enhance its contrast using a contrast-limited-adaptive-histogram-equalization (CLAHE) routine (MATLAB). Next, using Fourier analysis, we find the characteristic frequency for the patterns on the kymograph (S4 Fig). Finally, the slope corresponds to the change in phase at this frequency. Quality criteria are properly chosen to reject low-quality regions over the kymograph. To synchronize time-lapse acquisitions, the initial frame (time 0) was defined when surface mean intensity was around 200 A.U.

Single-molecule imaging and residence time measurement

FtsZ-YFP-mts previously incubated 1:1 with the nanobody GFP-Booster Atto647N (ChromoTek, Germany) for at least 1 h at 4°C under agitation. To filter out nonbound nanobody, we centrifuge our protein in a 30 KDa Amicon unit. The GFP-Booster Atto647N was excited with a 640 nm diode laser (30 mW, before objective). Single molecule imaging was performed using a standard Cy5 filter set. After 10 min of GTP addition, a significant number of spots in the single molecule channel (Atto647N) were observed and imaged at a rate of 1 fps or 3 fps with 0.3 s exposure time. To improve imaging conditions, we added 10 nM protocatechuate-dioxygenase (PCD) and 2 mM 3,4-protocatechuicacid (PCA) as an oxygen-scavenging system. To determine the position of every single molecule and calculate its residence time, we employed a MATLAB routine designed by Weimann and Ganzinger [114]. Briefly, a bandpass filter was used to remove low -and high- frequency noise. Then, single molecule positions with intensity above a user-defined threshold were determined by their brightness-weighted centroid. The detection algorithm is highly efficient for detecting particles with a signal-to-noise ratio above 1.5. The user-defined threshold was chosen to detect the largest number of spots and kept constant for all experiments. Single molecules were tracked among consecutive frames in an area given by a radius of 10 pixels (pixel size = 0.042 μm). Thus, the residence time is defined as the time that the particle stays in this area before its signal vanishes.

To calculate the mean residence time, we calculated the probability as a function of time

t to obtain a loss of signal event at times $\leq$ t (cumulative probability, S6A Fig). We fitted to a double exponential function $Ae^{-kt} + Be^{-k_p t}$, in which k refers to the inverse of the mean residence time, and k_p corresponds to the photobleaching rate. A and B are constrained, since the photobleaching contribution is limited to be between 0.2-0.25 in the fitting routine for all conditions (MATLAB). The photobleaching rate was calculated as $k_p = 0.031 s^{-1}$ using a single exponential fit shown in S6B Fig.

Events shorter than 2 frames are below the accuracy of our method and were not included in the statistics. The cumulative probability was measured for 5 different experiments having a total number of events (N) in each experiment. For GDP forms: 5 mM Mg^{2+}, N varies in the range of 3,000-5,300 events (1 fps) and 660-8,800 events (3 fps); 1 mM Mg^{2+}, N = 3,000-11,000 (3 fps). For GTP forms: 0.04 mM GTP, N = 1,300-3,000 (1 fps); and 4 mM GTP, N = 1,200-6,700. In the case of FtsZ*[T108A]-YFP-mts at 4 mM GTP, N = 180-800.

II.2.5 Supporting information

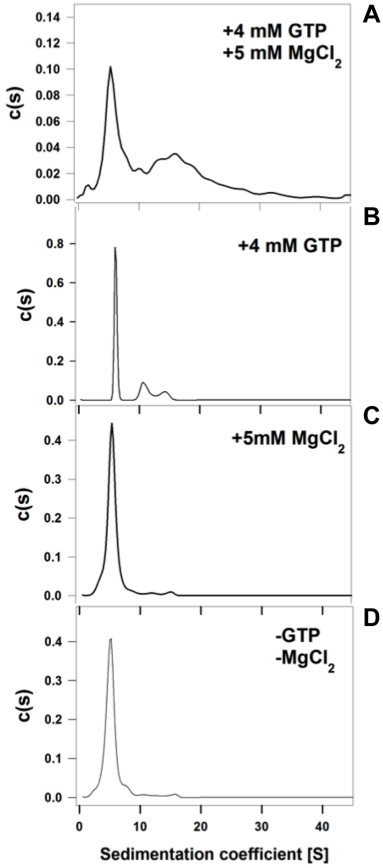

S1 FIGURE. FtsZ-YFP-mts sedimentation velocity analysis. c(S) sedimentation coefficient distributions obtained for the chimeric FtsZ variant (7 μM) obtained from experiments conducting in working buffer at the following conditions: 4mM GTP and 5 mM Mg^{2+} (A), 4 mM GTP but no Mg^{2+} added (B), 0.05 mM GDP and 5 mM Mg^{2+} (C), and 0.05 mM GDP and no Mg^{2+} added (D). These experiments show that FtsZ-YFP-mts is a well-behaved self-associating protein: In the absence of GTP and/or Mg^{2+} (B-D) the protein exists mainly as a slowly sedimenting species with s-value of around 6S (C-D), compatible with the heterodimeric FtsZ-YFG form. In the presence of both GTP and Mg^{2+} (A) most of the protein (70%) sediments as a polydisperse mixture of higher orders species with an average s-value of 20 +/- 5 S. These results are important because they allowed to control the association state of the membrane-targeted FtsZ variant by GTP and Mg^{2+}, which was crucial to obtain the reproducible dynamic ring-like structures on the bilayers shown in this work (see main text). The broad distribution of higher order species shown in (A) contrast to the sharp s-values observed in previous studies from the Rivas lab under specific experimental conditions of protein and buffer composition. These differences in sedimentation

coefficient distributions of FtsZ under assembly promoting conditions could in part be related to the presence of the mts-tag. However, they are also compatible with the behavior of self-assembling systems as plastic as FtsZ, in which it would take only a very small free energy perturbation to produce large changes in the relative abundance of the species present as higher order oligomers.

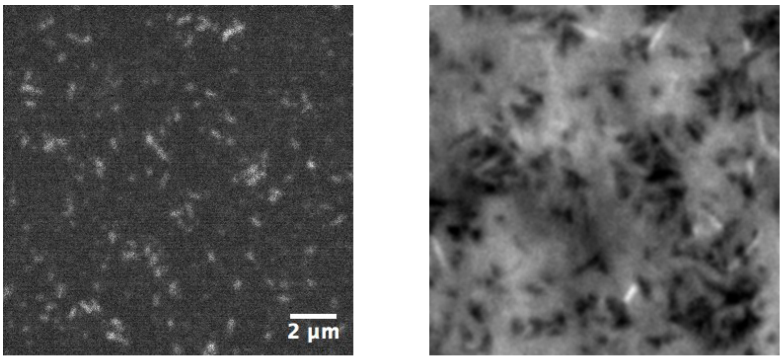

0.1 µm FtsZ-YFP-mts 1 µm FtsZ-YFP-mts

S2 FIGURE. Representative images of FtsZ-YFP-mts at low (left panel) and high (right panel) protein concentrations. Only short filaments could be detected at 0.1 µM, no further structures were later observed. On the contrary, when 1 µM of FtsZ-TFP-mts is added, polymer networks were observed almost instantly at the vicinity of the membrane. Dynamic rings were only noticed at intermediated protein concentrations.

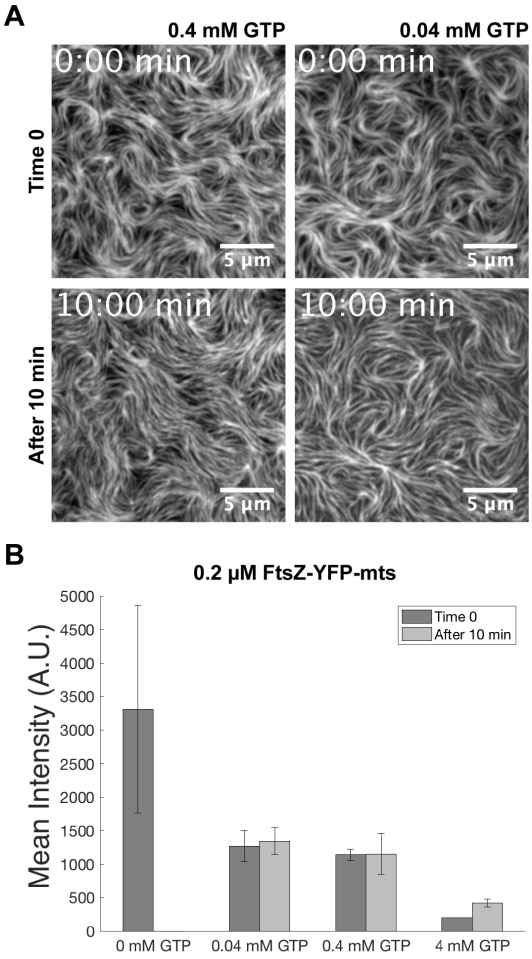

S3 FIGURE. Effect of GTP concentration on the FtsZ-YFP-mts rings formation**. (A)** Images of 0.2 µM FtsZ-YFP-mts bundles after the addition of 0.4 mM GTP and 0.04mM GTP showing long filaments with a parallel arrangement. Images of upper panels were taken 1-2 minutes (Initial acquisition) after GTP addition. Lower panels represent images after 10 minutes. **(B)** Bar plot of the mean fluorescence intensity of the different GTP concentrations at initial time of triggering and 10 minutes later.

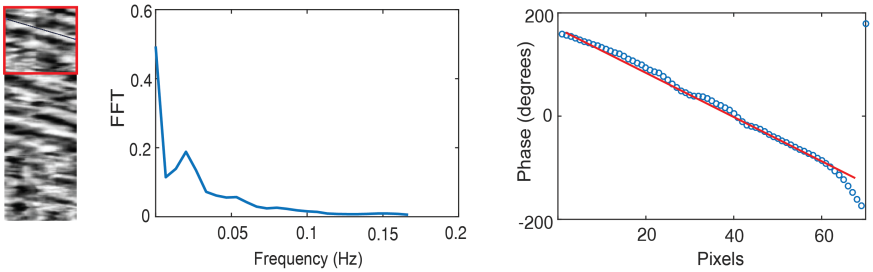

S4 FIGURE. Fourier Analysis allows to calculate automatically the slope of the kymograph. **(A)** A representative kymograph after a Savitzky-Golay filter and enhance contrast using a contrast-limited-adaptive-histogram-equalization (CLAHE) routine. To discard low quality regions, the analysis is made over 50 vertical pixels (marked region in A). **(B)** The fourier transformation spectrum (FFT) shows a clear peak at ~0.02 Hz. **(C)** Then, to calculate the slope, we measure the change in phase by linear fit. Regions are rejected when a) the peak in the FFT spectrum lower that 10-fold the mean of the FFT data or b) linear fit with R^2 <0.95.

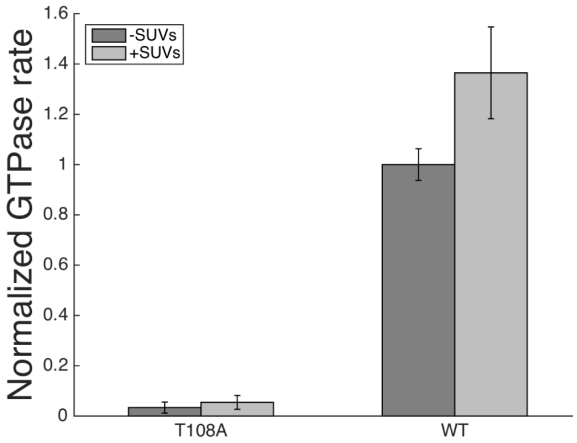

S5 FIGURE. GTPase activity of FtsZ-YFP-mts (5 μM) or FtsZ*[T108A]-YFP-mts (5 μM) in the absence or presence of phospholipids (4 mg/ml). The corresponding rates where normalized to the GTP activity of FtsZ-YFP-mts in the absence of phospholipids. We observed that the GTPase activity of FtsZ*[T108A]-YFP-mts was almost zero. GTPase activities were determined using the BIOMOL GRENN assay (Enzo). Error bars correspond to s.d. from three different experiments.

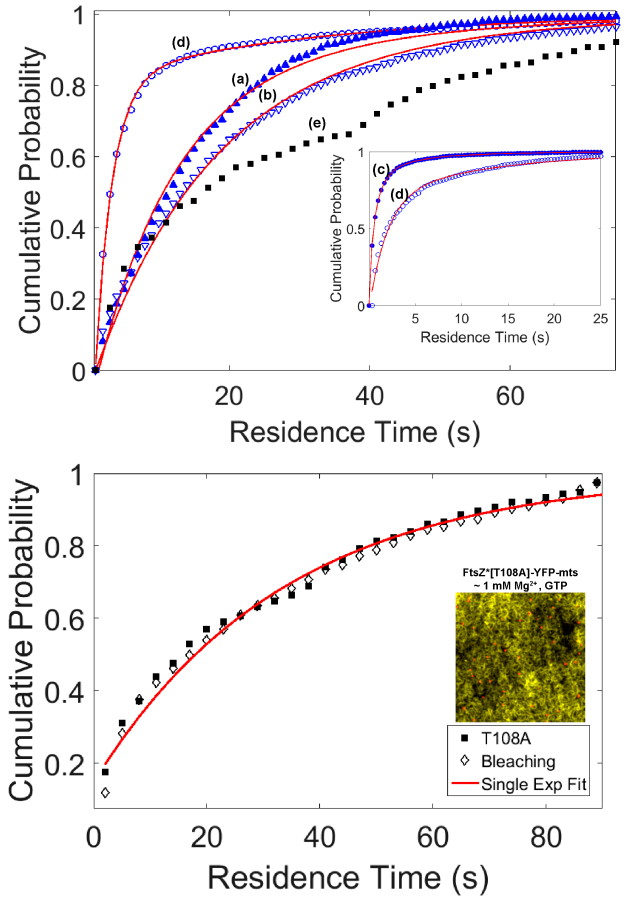

S6 FIGURE. **(A)** Cumulative probability of the residence time distributions for (a) 4mM GTP 1mM free Mg^{2+} and (b) 0.04 mM GTP 1 mM free Mg^{2+} having an acquisition rate (1fps). Inset: Cumulative residence time distribution for GDP forms with a faster acquisition rate (3fps) at (c) 1 mM free Mg^{2+} and (d) 5 mM free Mg^{2+}. Note that the residence time distributions for GDP - 5 mM Mg^{2+} (blue circles) are equivalent at 1fps or 3fps. (e) represents photobleaching decay. Curves were fitted to a double exponential function to calculate the mean residence time having a constant photo-bleaching contribution. Further details are under "Materials and Methods". **(B)** Cumulative probability of the residence time distribution for FtsZ*[T108A]-YFP-mts (closed squares). In the same plot the photobleaching timescale of fixed nanobodies is shown (empty inverted triangles).

III

OPTICAL TWEEZERS TO PULL LIPID TUBES FROM GIANT UNILAMELLAR VESICLES (GUVS)

In this chapter, I describe the current state of the technique of pulling out lipid tubes ($d < 100nm$) from -controlled membrane tension- GUVs using optical tweezers. Since FtsZ senses curvatures $\sim 1\ \mu m^{-1}$, the technique had to be modified. Here, I describe the new-methodology I have implemented to increase the mean diameter ($d = 0.47\mu$m) of pulled lipid tubes.

III.1 Optical tweezers: A brief introduction

Since Maxwell's equations predicted that light could transmit momentum and create a radiation pressure -pushing- illuminated objects, experimental data was required to prove these predictions [44]. First data came from very complicated experiments showing light-induced torque. However, these effects were small and hard to replicate. After the invention of lasers [44], Ashkin (Nobel Laurate in Physics, 2018) showed that laser-light could accelerate microscopic semi-transparent particles in the direction of light [8]. Indeed, trapping particles was possible by using two laser beams traveling in opposite directions [8]. Interestingly, later Ashkin et al. (1986) also demonstrated that a single laser beam could create a negative light pressure -due to a gradient force- that can trap dielectric particles [8] .

To calculate light-induced forces, Mie theory derives the exact analytical solutions of Maxwell's equations that apply to any particle size, compared to the laser-wavelength [45]. However, math is complicated and out of the scope of this thesis. However, for the two extreme situations $\lambda << R_p$ and $\lambda >> R_p$ (R_p=particle's radius) the quantitative analysis rescue the two forces contributions which origins the optical trapping phenomenon: the scattering and gradient contribution.

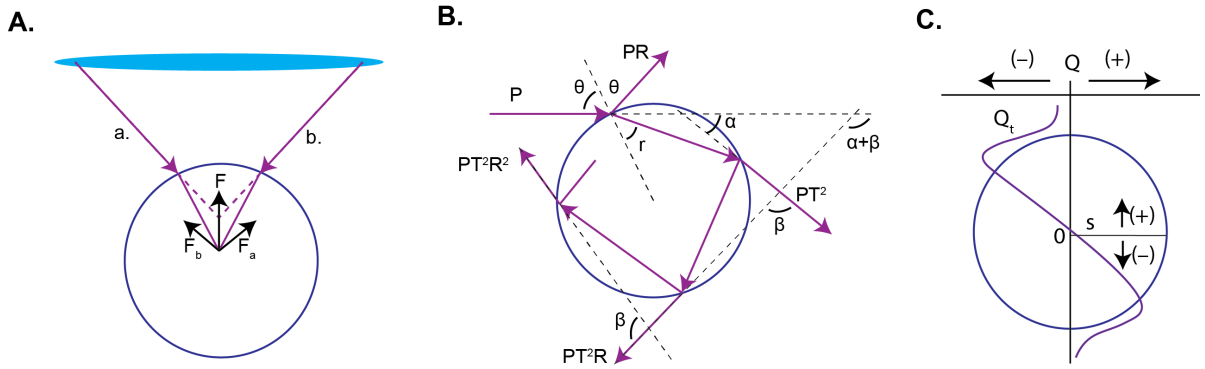

Figure III.1: Ray optics explains optical trapping. A) Two rays a and b reach the sphere and their refraction causes a change of momentum generating an upwards force. B) Scattered rays make relative angles with respect to the incident ray $\pi + 2\theta$, α, $\alpha + \beta$, $\alpha + 2\beta$, ... $\alpha + n\beta$. C) The axial trapping potential here expressed by the Q-factor that rules the direction of the force.

In the ray optics regime ($\lambda << R_p$), when a light ray hits a surface and it is reflected, there is a change of momentum per unit of time (force) given by $\mathbf{F} = -2P/c\,\mathbf{u}$ where P is the laser power, c the speed of light and $\mathbf{u}$ the unitary vector indicating the light propagation direction [44]. In a similar way, refraction of two ray beams a and b hitting a sphere, as shown in Figure III.1A, causes a momentum change that creates an upwards net force. Consequently, the exit of those a and b causes a downwards net force. Therefore, this is the qualitative principle behind optical trapping and trapping potential. Further than a qualitative description, Ashkin et al (1992) estimated the exerted forces of a focused laser beam (exiting an objective) over a dielectric sphere (Fig. III.1A) [9]. The net force on the sphere is the contribution of the first reflected ray PR and an infinite sum of refracted rays PT^2R^n, where R and T represent the Fresnel reflection-refraction coefficients. As shown in Figure III.1B, scattered rays make relative angles with respect to the incident ray $\pi + 2\theta$, α, $\alpha + \beta$, $\alpha + 2\beta$, ... $\alpha + n\beta$. Thus, the total force can be written in F_z and F_y components [9]:

$$F_z = F_s = \frac{mP}{c} - \Big(\frac{mPR}{c}\cos(\pi + \theta) + \sum_{n=0}^{\infty} \frac{mP}{c} T^2 R^n \cos(\alpha + n\beta)\Big) \qquad \text{(III.1)}$$

$$= \frac{mP}{c}\Big(1 + R\cos(2\theta) - \frac{T^2[\cos(2\theta - 2r) + R\cos(2\theta)]}{1 + R^2 + 2R\cos(2r)}\Big) = \frac{mP}{c}Q_s \tag{III.2}$$

$$F_y = F_g = \frac{mP}{c}\Big(R\sin(2\theta) - \frac{T^2[\cos(2\theta - 2r) + R\cos(2\theta)]}{1 + R^2 + 2R\cos(2r)}\Big) = \frac{mP}{c}Q_g \tag{III.3}$$

where m is the ratio between the sphere-refractive index over the medium index n_p/n_m. Also, θ and r represent incident and refractive angles respectively. Note that net forces are polarization-state dependent since R and T Fresnel coefficients vary with light polarization. As a result, the magnitude of the total force experienced by the bead can be described by [9]:

$$F = \sqrt{Q_s^2 + Q_g^2}\,\frac{mP}{c} \tag{III.4}$$

By assuming a before-objective beam radius and a typical -objective- numerical aperture (NA) to estimate the range of possible angles ($\phi_{max} \sim 70°$), a fairly close computation of Q can be achieved. This calculation also considers different light polarization (parallel/perpendicular) contributions. Figure III.1C sketches Q_t as as function of the distance S above/below of the center of the bead [9]. Interestingly, gradient forces balance weaker scattering forces creating a force profile largely confined inside the sphere and having the equilibrium point S_e slightly above the center ($S \sim 0.06$). Clearly, signs in Q_t indicate a restoring force pushing for equilibrium: upwards displacements are counteracted by a downwards force and vice versa [9]. The maximum value for the restoring force occurs very close to the edges of the sphere ($S = 1.01$ and $-S = 1.02$). Furthermore, the magnitude of this restoring force has an important component of large angle $\sim 70°$ rays. As a result, for practical matters, a high NA objective is very important for robust trapping.

For the Rayleigh case, the electric **E** and magnetic **B** field of the laser beam interact with the dipole **p** moment of a point-like particle ($\lambda >> R_p$). As a result, this dipole experiences

a force according to the Lorentz equation:

$$\mathbf{F} = (\mathbf{p} \cdot \nabla)\mathbf{E} + \frac{\partial \mathbf{p}}{\partial t} \times \mathbf{B} \tag{III.5}$$

An applied electric field applied to an atom or a molecule induce a dipole moment $\mathbf{p} = \alpha\mathbf{E}$ where α is polarizability coefficient of an atom. Using the *Clausius-Mossotti* relation, the dipole of a small volume element dV can be written [45]:

$$\mathbf{p} = \epsilon_0 n_m^2 \alpha dV \mathbf{E} \tag{III.6}$$

where ϵ_0 is the vacuum permittivity and $\alpha = 3(m^2-1)/(m^2+2)$ with $m = n_p/n_m$. Using $(\mathbf{E}\cdot\nabla)\mathbf{E} = \frac{1}{2}\nabla\mathbf{E}^2 - \mathbf{E}\times(\nabla\times\mathbf{E})$ identity and $\nabla\times\mathbf{E} = -\frac{\partial}{\partial t}\mathbf{B}$ (Faraday's Law), equation III.1 can be written to calculate the force-density contribution of a small volume element [45]:

$$\mathbf{f} = \epsilon_0 n_m^2 \alpha dV (\frac{1}{2}\nabla\mathbf{E}^2 + \frac{\partial}{\partial t}\mathbf{E} \times \mathbf{B}) \tag{III.7}$$

To calculate the net force, the gradient $\nabla\mathbf{E}^2$ and the scattering $\frac{\partial}{\partial t}\mathbf{E} \times \mathbf{B}$ contributions are integrated over the sphere volume. Assuming that for small objects the gradient $\nabla\mathbf{E}^2$ remains constant over the entire volume, the integral for the gradient can be simplified whereas a relatively simple calculation for the scattering part is not possible. The scattering contribution represents an small force offset (compared to the gradient contribution) that is proportional to the laser intensity I [45].

$$\mathbf{F}_g = \int_V f dV = \epsilon_0 n_m^2 \alpha \int_V (\frac{1}{2}\nabla\mathbf{E}^2) = \frac{n_m \alpha V}{2c}\nabla I \tag{III.8}$$

An important aspect to be mentioned is that gradient forces are linear with the small displacements d. Assuming a Guassian beam with x-width: $\sigma_x = 0.61\lambda/\mathrm{NA}$, the gradient force can be Taylor-expanded to have an approximated expression for the trap-stiffness. Similar analysis can be done for y and z. This linear behavior is widely used for measuring forces in the scale of piconewtons (pN) since the trap-stiffness κ can be easily determined

[45].

$$F_g(d) = F_g|_{d=0} + \nabla F_g|_{d=0} \cdot d + \mathcal{O}(d^2) \approx \frac{n_m \alpha V I_0}{\sqrt{8\pi}c} \frac{1}{\sigma_x^3} \cdot d = \kappa \cdot d \tag{III.9}$$

III.2 The physics of pulling tubes from GUVs: current state of the technique

Giant unilamellar vesicles (GUVs) are 3D spherical objects made of a lipid-bilayer shell. The size of GUVs varies from $5 - 80\,\mu m$ depending on the swelling method (e.g. electroformation, swelling, emulsion techniques) [10,112]. Since biological phenomena occur, mostly, in 3D environments with defined geometry, GUVs represent an important model-system to study protein-lipid interaction when geometry and surface-stiffness has to be defined. For example, GUVs have been widely used to study protein reconstitution over tubular geometries since the ease of creating tubular structures from GUVs. Several techniques have been used to extract lipid tethers from GUVS (or liposomes) using micro-manipulated micropipettes [32], controlled flows [13] and optical tweezers [89]. For the purpose of this thesis, the optical tweezers approach is highlighted.

To understand the process of forming a tube from GUVs, the elastic properties of a -fluid lipid bilayer- have to be considered. Bending a square flat surface (a like a piece of paper) require of compression of the inner leaflet and stretching of the outer leaflet (Figure III.2A). The energetic cost of this deformations can be calculated as [24]:

$$E_{bend} = Y \frac{V - V_0}{V_0} \tag{III.10}$$

where Y represents the Young's module and V volume. Assuming that the square flat surface has an area $A = L^2$ size and thickness h , the energy -per area- required to bend the surface is [24]:

$$e_{bend} = \frac{E_{bend}}{L^2} = \frac{1}{2} Y \int_{-h/2}^{h/2} \left(\frac{z}{R}\right)^2 dz = \frac{1}{24} Y \frac{h^3}{R^2} \tag{III.11}$$

By defining the stretching modulus as $K_a = Yh$ and the bending modulus as:

$$\kappa_b = \frac{1}{12} K_a h^2 \tag{III.12}$$

equation III.11 can be written as:

$$e_{bend} = \frac{1}{2}\kappa_b \frac{1}{R^2} = \frac{1}{2}\kappa_b c^2 \tag{III.13}$$

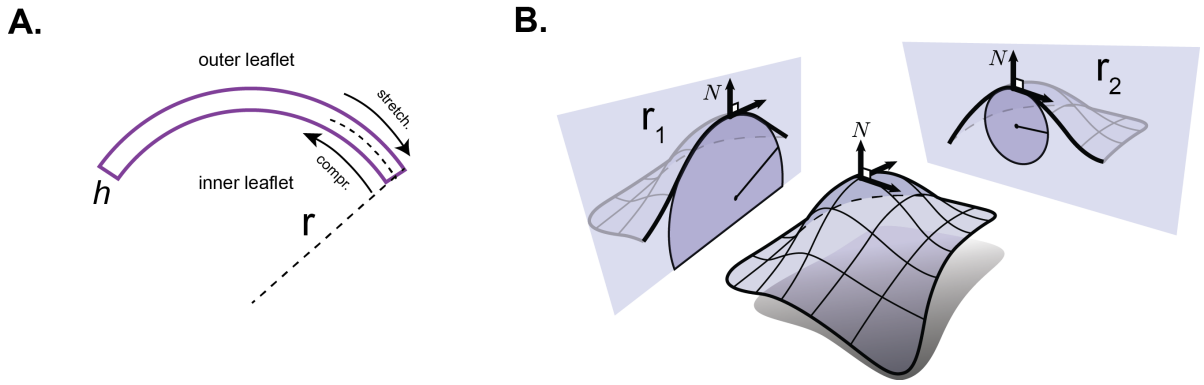

Figure III.2: Membrane surface curvatures. A) Bending a lipid bilayer membrane (piece of paper shape) implies stretching in the outer leaflet and compression in the inner leaflet. B) An arbitrary surface can be described by two main curvatures: $c_1 = 1/r_1$ and $c_2 = 1/r_2$. Illustration (modified) retrieved February 29, 2019, from http://brickisland.net/cs177/?p=144.

Interestingly, this energy has a spring-like behavior meaning that it scales quadratic with the surface curvature (curvature= $1/R$) [24]. Also, the bending modulus κ_b, an -energy units- constant, characterizes the elastic properties of the material. Accordingly, W. Herfrich (1973) proposed a mathematical formalism that generalizes this quadratic-curvature dependence for the bending energy [37]. The Helfrich-Hamiltonian defines the membrane energy density as a function of its mean curvature $H = 1/2\,(c_1 + c_2) = 1/2\,(1/r_1 + 1/r_2)$ (Figure III.2B), intrinsic curvature c_0 (e.g. intrinsic lipid shape) and tension σ [10]:

$$F_{Helfrich} = \int_A \Big[\frac{\kappa_b}{2}(2H - c_0)^2 + \sigma\Big] dA \tag{III.14}$$

Regarding GUVs (spherical lipid bilayer shell), the Helfrich-Hamiltonian governs the GUV

shape which -at equilibrium- is spherical, like a soap bubble. Here, two aspects are worth to mention about this equation. First, a lipid bilayer with symmetric composition (inner-outer leaflet) has an intrinsic curvature $c_0 = 0$. Interestingly, binding of proteins (or polymers) subjected to bind only one leaflet (only from inside or only from outside) can locally alter curvature and then drive GUV shape transformations such as budding [98] or tubulation [100]. Second, the bending modulus represents an intrinsic property of the lipid bilayer. It depends on the physical state (liquid-solid state) and chemical lipid properties. For example, lipid's fatty acids length and unsaturation level (carbon double bonds) highly modulate the bending modulus [67, 84]. Lipid membranes exhibit κ_b values between $10 - 100 k_B T$ where $k_B T$ ($\sim 4 \times 10^{-21}$J) refers to the thermal energy with k_B as the Boltzmann's constant.

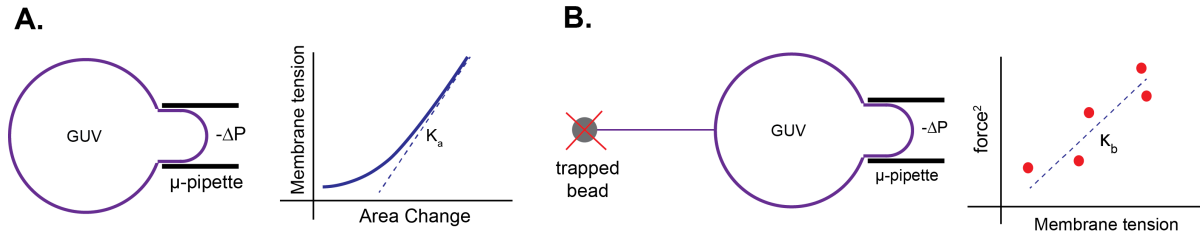

Figure III.3: Measuring the lipid stretching and bending modulus. A) The micropipette aspiration ($-\Delta P$) permits to vary the membrane tension and measure the membrane area change. In a high tension regime, the membrane tension is linear with the area change (K_a, stretching modulus). Using optical tweezers, a nanotube can be pulled from a GUV that is hold-aspirated ($-\Delta P$) by a micropipette. Since the the square of force scales linear with the membrane tension, the bending modulus κ_b represents the slope of the plot.

Due to the importance of the bending modulus to study lipid surfaces, various methods have been implemented to measure this value. In this regard, pioneering work has been performed by E. Evans and coworkers [47]. Using this approach, a GUV is aspirated ($-\Delta P$) using a micro-pipette to impose a membrane tension according to Laplace relation ($\Delta P = 2\sigma/R$). The response curve - σ vs. $\Delta A/A_0$ - suggests two elastic regimes: (i) a logarithmic regime proportional (slope in log-scale) to the inverse of the bending modulus κ_b (low tension) and (ii) a linear regime related to stretching modulus K_a (high tension, Figure III.2A). Indeed, the first regime represents the aspiration of microscopic thermal membrane undulations/fluctuations that represent a reservoir of membrane. Once this reservoir is aspirated, the lipid bilayer is clearly stretched. Therefore, appropriate fitting routines permit to determine both constants K_a and κ_b. As mentioned above, K_a and κ_b

are related by equation III.12; however, this equation needs a further correction. Using the "polymer brush model" Rawicz and coworkers found an expression that relate K_a and κ_b [84] (without Poisson's ratio ν correction [24]). Interestingly, this expression is two-times stiffer than considering two uncoupled-monolayers with $h/2$ (III.12):

$$\kappa_b = \frac{1}{24} K_a h^2 \frac{1}{1-\nu^2} \tag{III.15}$$

After discussing the importance of the bending module, the Helfrich Hamiltonian (eq. III.12) can be easily solved for a tubular geometry [23, 88]. In a tube, the only curvature is the inverse of its radius $c_t = 1/R_t$ and the area change is $\Delta A = 2\pi R_t L$ where L is the length of the tube. Then, the Helfrich energy functional can be written:

$$e_t = 2\pi R_t L\Big(\sigma + \frac{\kappa_b}{2R^2}\Big) - fL \tag{III.16}$$

where the f represents the force required for extracting a tube, independent of its length. By minimizing equation III.16 ($e_t = 0$, with respect to R_t and L), the radius R and force f at equilibrium can be easily determined [23, 88]:

$$f = 2\pi\sqrt{2\sigma\kappa_b} \tag{III.17}$$

$$R = \sqrt{\frac{\kappa_b}{2\sigma}} \tag{III.18}$$

These two simple expressions suggest the advantage of using optical tweezers to pull lipid tubes from GUVs. First, the square of the force is proportional to the membrane tension meaning that, by varying the membrane tension, the bending modulus (Figure III.2B) can be measured (slope). To vary the membrane tension, the GUVs is hold by a micropipette that aspirate proportional to $-\Delta P$. This approach has been used to determine bending modulus under physiological conditions (solutions with ionic strength > 0) [89] when proteins are used. Second, once the bending modulus is determined, this technique permits to control the radius since the square of the radius scales inversely with the membrane tension. Reasonable values for membrane tension ($\sigma = 0.005$ mN/m) and bending modulus

($\kappa_b \sim 10 k_B T$) produce nanotubes with radii around 50 nm [89]. In practical terms, it is easier to pull nanometric tubes since the -achievable- negative pressures enough to hold a GUV already imposes membrane tension sufficient to pull small tubes ($r < 100$ nm). As a result, this approach has been widely used for studying proteins such as dyanamin and ESCRT that constricts nanometric lipid tubes [89,92] as well as curvature-sensing-proteins (BAR proteins) [99].

The small-tube-diameter restriction represented a challenge for the purpose of this thesis since FtsZ is a curvature-sensing-protein in the scale of 1 μm^{-1}. Therefore, modifying the current state of the technique was needed without compromising the convenience of pulling tubes with optical tweezers and the possibility to measure forces.

III.3 Construction of an optical tweezers apparatus to pull lipid tubes: a new approach to obtain larger tube diameters

III.3.1 Construction of an optical tweezers apparatus with force detection

The optical tweezers setup (Fig. III.4) was built according to previous methods-reports [44, 45, 51, 64]. Briefly, a 3W 1064 nm DPSS laser (Cobolt, Sweden) was used as trapping laser. A half-wavelength plate ($\lambda/2$ plate) and a polarizing beam splitter (PBS) control the laser power entry to the scope (Thorlabs, USA). The $\lambda/2$ plate rotates the polarization angle while the PBS selects the P-polarized light to pass though (S-polarized is directed to a beam waste). A two-lens telescope expands the laser beam to fill the back aperture of -above mentioned- 100X objective (NA=1.45, Nikon, Japan). In addition, two mirrors adjust the laser-beam xy position. The force detection arm was mounted in the microscope illumination pillar, collecting (from above) the light from the laser using a -long working distance- condenser 20X, $NA = 0.6$ (Edmund optics, USA). A micrometric xyz stage positions the condenser (and the detection arm) in -z- to achieve Köhler illumination and -xy- for centering. For alignment, once the proper laser-axis has been defined, the position of field diaphragm (in Köhler illumination) is imaged through an auxiliary camera

DCC3240M (Thorlabs, USA) on the right port of the microscope. Using camera software options, a drawing masking the field diaphragm was saved in a file. This drawing can be re-used in such way that the drawing overlays the real-time camera acquisition. Therefore, xyz knobs are moved to position the field-diaphragm according to the drawing mask (Fig. III.5).

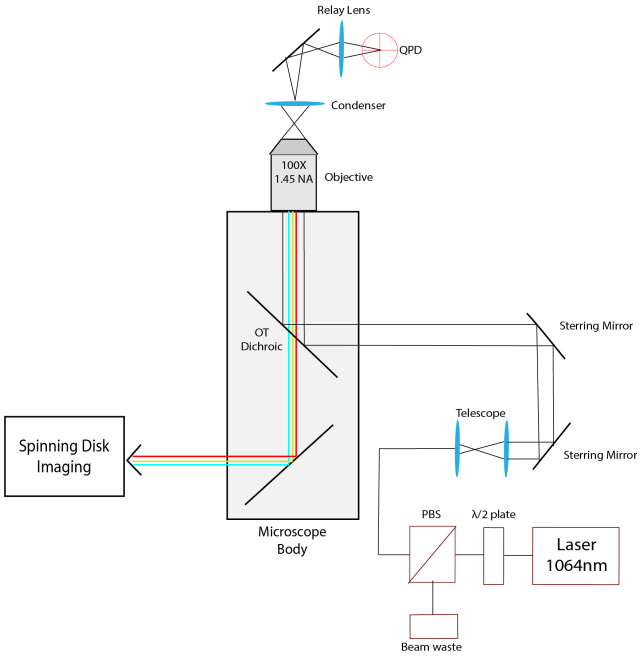

Figure III.4: Optical tweezers apparatus layout.

In the detection arm, a relay lens imaged the back focal plane of the condenser in a (QPD) quadrant positional detector PDQ80A (Thorlabs, USA). The signal voltage of the QPD defined the position of the trapped bead. The force detection module OTKBFM (Thorlabs, USA) was used for data acquisition. This DAQ acquired a voltage signal from the QPD at a maximum rate of 100 kHz. In addition, this module was customized to control a 20×20 μm range LT2 piezoelectric-stage (Piezoconcept, France) using an analog signal (1-10 volts). Position calibration and trap-stiffness determination was performed using the OTKBFM software (Thorlabs, USA). To calibrate position, beads were attached to a clean glass coverslip (Fig. III.5A) in high salt medium (1M NaCl). Here, the streptavidin-coated beads have a mean diameter of 1.71 μm (Spherotech, USA). The laser beam is focused over one bead. The xy position of the bead, relative to laser beam, was adjusted using the piezo-stage to maximize the signal in QPD. Similarly, the focus -z- position of the laser beam was adjusted to maximize QPD output. Then, the piezo-stage was moved 4 x 4 μm

xy and changes in QPD signal were recorded. From the typical "s-shape" response curve, a straight line was fitted representing the volts to μm conversion (Fig. III.5C).

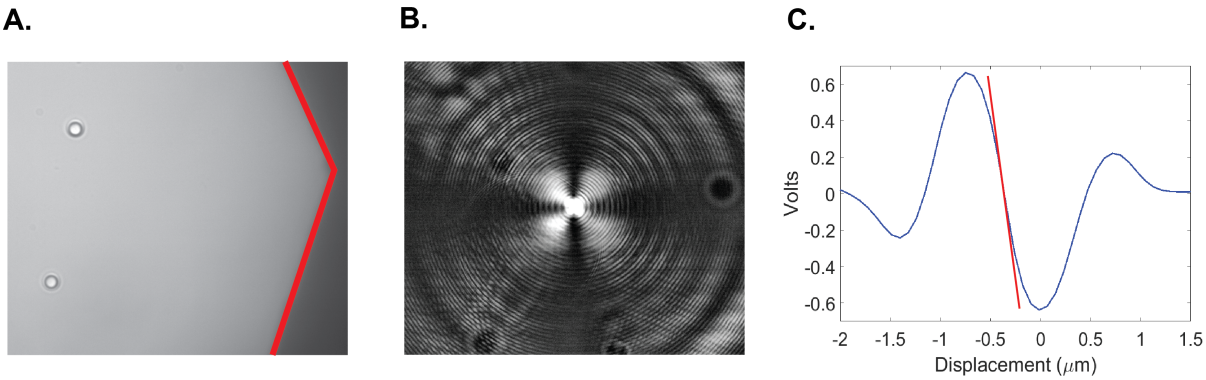

Figure III.5: Alignment of optical tweezers apparatus. A) The position of the field diaphragm was imaged, at the appropriate trapping-laser-axis, to create a mask (red line) in an auxiliary camera. For regular alignment, xyz position of the detection module was adjusted to overlap the mask position (Köhler illumination). B) Back-scattered light pattern for a trapping laser focused over a surface-bound bead (as shown in A). Symmetry of this pattern was vital for robust trapping. C) By scanning a surface-bound-bead (as shown in A) with the trapping-laser, a typical "s-curve" is obtained. From its linear range, a -volts to μm- conversion of 1.66 volts/μm was measured.

Once one bead was trapped, the trap stiffness was determined using the power-spectrum analysis. A trapped bead, also influenced by Brownian motion, can be described by the following motion equation [44]:

$$\frac{dx(t)}{dt} = -\frac{\kappa}{\gamma}x(t) + \sqrt{2D}\,W(t) \tag{III.19}$$

where κ is the trap stiffness; $\gamma = 6\pi\eta a$, the particle friction (η: viscosity and a: particle's radius); D, the diffusion coefficient and $W(t)$, a white noise function with intensity $\sqrt{2D}$. Taking the Fourier transform of equation III.19 [44]:

$$2\pi(f_c - if)\check{X}(f) = \sqrt{2D}\,\check{W}(f) \tag{III.20}$$

where $f_c = \kappa/(2\pi\gamma)$ is the "corner frequency". $\check{X}(f)$ and $\check{W}(f)$ represent $x(t)$ and $W(t)$ in the Fourier space. By taking the square modulus of equation III.19, we obtain the power

spectrum density (PSD) of the particle motion [44],

$$PSD = |\check{X}(f)|^2 = \frac{1}{2\pi^2}\frac{D}{f_c^2 + f^2} \tag{III.21}$$

Therefore, the corner frequency (trap-stiffness) can be determined from the experimental PSD (Fig. III.6A). To measure the trap-stiffness, the OTKBFM-included-software (Thorlabs, USA) was used. Since the trap-stiffness is proportional to the laser power, the trap-stiffness was measured over different laser powers to characterize its linear regime (Fig. III.6B).

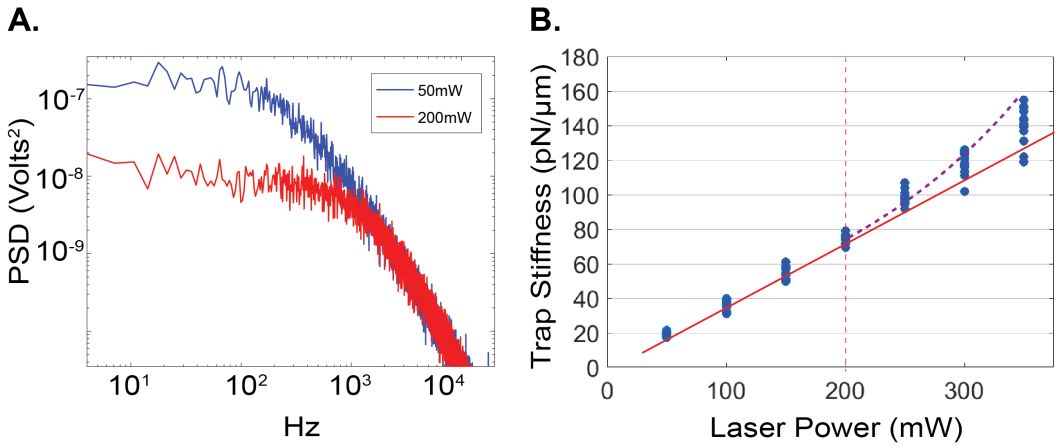

Figure III.6: PSD and trap-stiffness linear regime. A) The power spectrum density (PSD) of trapped-beads using different laser powers (laser power measured before objective). Using this approach, the corner frequency can be easily determined. Clearly, f_c was right-shifted for the case of higher laser power implying that trap-stiffness was increased. B) Trap-stiffness exhibited linear behavior for laser powers below 250 mW.

III.3.2 Pulling lipid tubes from GUVs: a new approach to obtain larger tube diameters

Without mentioning details, FtsZ experiments did not exhibit any interesting phenomenology for small diameters ($r < 100$ nm, high membrane tension imposed by a micropipette) most probably because of FtsZ's curvature ($\sim 1\ \mu m^{-1}$). On the other hand, FtsZ induced "inwards" deformations only when an osmolarity gradient produced deflated GUVs [7]. Then, the idea was to pull out a lipid tube from a surface-bound GUV with low surface

tension $\sigma \approx 0$ (Fig. III.7) to achieve large tube diameters ($d > 200$nm) (equation III.16). The GUV has to be mildly bound to the surface with a friction force larger than the force required to pull a tube. Otherwise, the GUVs was moved by the trapped bead. Therefore, the challenge here was to design a robust strategy to create deflated vesicles. Dilution of GUVs in higher -constant osmolarity buffers- showed no advantage since high osmolarities gradients caused -a high frequency- of tubulating GUVs.

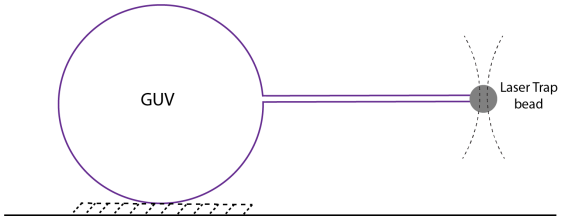

Figure III.7: Pulling out lipid tubes from deflated vesicles. Pulling out lipid tubes from surface-bound GUVs with low surface tension $\sigma \approx 0$ to achieve large tube diameters ($d > 200$nm) (equation III.16). GUVs have to be mildly bound to the surface with a friction-force larger than required-force to pull out a tube (otherwise, the GUVs is moved by the trapped bead).

The osmolarity challenge was overcome by using an evaporation chamber (Fig. III.9) (similar chambers are used in Aurelien Roux's lab, University of Geneva). As long as the water evaporates, the osmolarity in -outside buffer- slowly increases. The chamber was made using -customized size- coverslip glasses (Menzel, Germany) and a PMMA 3mm height spacer. The bottom coverslip had 1.5 thickness and 12 mm width. The upper one was 1.0 thickness and 10 mm width. Note that the upper coverslip width was smaller in order to form a meniscus that decreases water evaporation rate. Coverslips were cleaned by immersion in a 50:50 water/ethanol solution followed by 1-minute air-plasma cleaning. After this, coverslips were glued to the spacers and passivated for more than two hours using 5 mg/ml using β-casein (Sigma, Germany). Glass passivation here was critical since no-passivation implied a higher vesicle adhesion, increasing membrane tension. Water evaporation increased osmolarity at a rate of $\sim$ 50 mOsm per hour under constant temperature and humidity conditions. Examined vesicles were located in the central area of the chamber, fairly distant from the evaporation meniscus. Samples were discarded after 1 hour to avoid extreme deflation states.

Strikingly, large diameter-tubes ($d \sim 0.5\mu$m) were pulled under these evaporation conditions. GUVs were made of E.coli lipids (Avanti, AL, United States) doped with 0,05% (mol) of ATTO655-DOPE for lipid imaging (ATTO-Tech GmbH, Germany) and 0.15% of

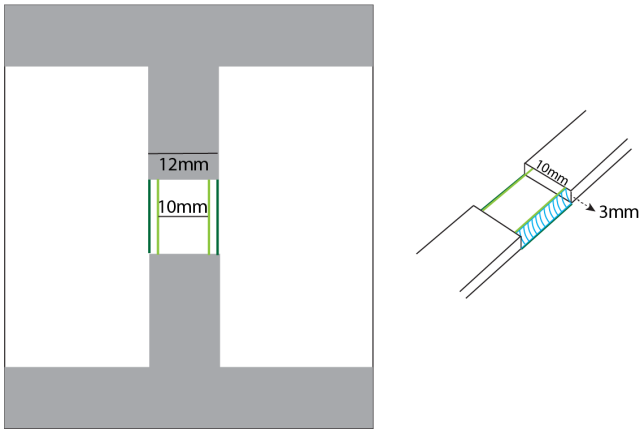

Figure III.8: Evaporation chambers design

DSPE-PEG-(2000)-Biotin (Avanti, AL, United States). Since biotinylated lipids bind to 1.71 μm streptavidin-coated beads (Spherotech, USA), a lipid tube resulted from moving the GUV away from the trapped bead (Fig. III.9B). The force required for pulling a tube, in the here flaccid case, was estimated $\sim$ 6.5 pN (Fig. III.9A). First, this implied that the friction force must be larger than this value. Second, this force value is lower than the case of lipid nanotubes (micro-aspirated vesicles) which is around 10 pN (private conversation with Prof. Aurelien Roux). The here estimated force agreed to what is expected according equation III.16 because the force decreases with the square root of the membrane tension σ.

Two technical aspects have to be mentioned: i) because no pipette is holding the vesicle, "pulling-out" force measurements were challenging since vesicles were free to have position-fluctuations affecting the zero-force reference. However, three independent "clean" experiments showed values between 4-6.5 pN (Fig. III.9B). ii) since there is no a micro-aspirating pipette tuning membrane tension, this parameter is unknown. Given equation III.16, the only parameter that determines tube diameter is the membrane tension (κ_b is constant). This parameter summarizes the area reservoir of the vesicle with respect to its size. Therefore, the tube diameter measurement represented a direct way to asses the membrane-tension. Tube diameter was measured by fitting the normalized intensity (lipid red dye) profile to a Gaussian curve, integrating the whole tube (Fig. III.10A). Reported diameters were half-width of the fitted-Gaussian. Therefore, pulled-tubes from N=55 GUVs, from different samples and deflation-states were measured. The diameter distribution showed a well-behaved Gauss-like-distribution (Fig. III.10B) with a mean of

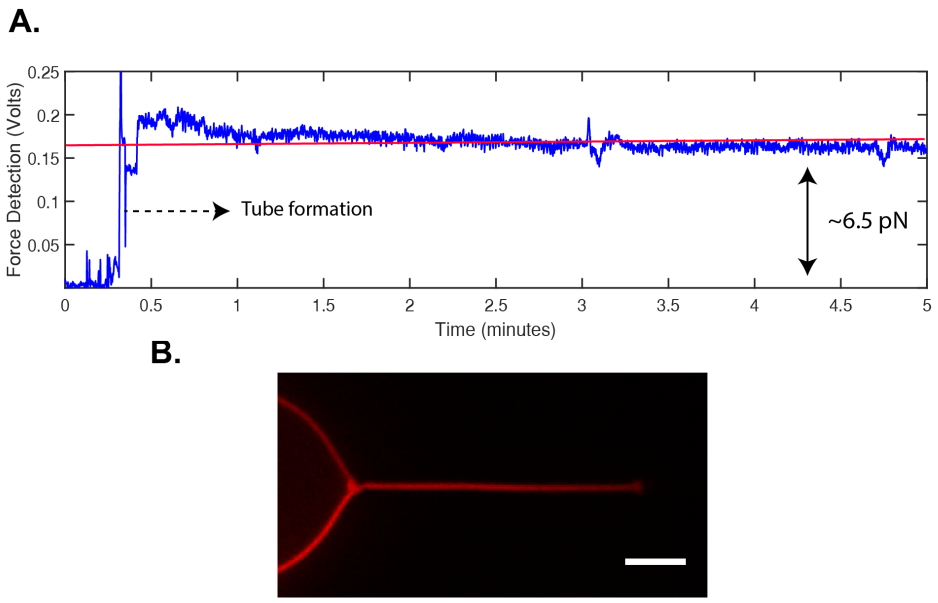

Figure III.9: Pulling out tubes with large diameter. A) Force-time plot showing the needed force to pull a lipid tube from a deflated GUV. After putting in contact the trapped bead and the GUV (peak before 0.5 mins), the stage was moved away to pull a lipid tube. The force required to form this tube is $\sim$ 4 pN. B) Image of the lipid tube with 0.5 μm lipid tube using ATTO655-DOPE red dye for lipids (scale bar=5 μm).

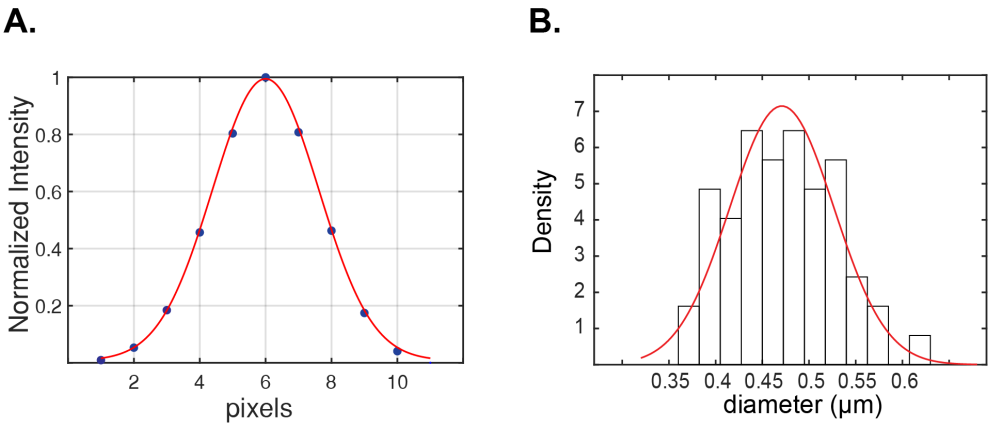

Figure III.10: Tube diameter distribution. A) The tube diameter was measured by fitting the normalized intensity (lipid red dye) profile to a Gaussian curve. B) The tube diameter distribution (N=55) showed a well-behaved Gauss-like-distribution with a mean of 0.47 μm.

0.47 μm (binning width = 0.0225 μm). This implied that membrane-tensions equivalent to this mean ($\pm$ standard deviation) are highly frequent for the here used experimental conditions despite of further control on the vesicle membrane tension.

IV

TORSIONAL STRESS EXERTED BY TREADMILLING FTSZ FILAMENTS OVER DEFORMABLE LIPID TUBES

In this chapter, I demonstrate that FtsZ filaments exert Darboux torques (twist) producing inwards vortex-like deformations on deformable GUVs and spring-like structures on soft lipid tubes. Interestingly, GTPase activity drives a super-twisted state causing either spring compression on a lipid tube or the formation of constriction necks when reconstituted inside GUVs.

IV.1 Extended introduction

IV.1.1 FtsZ-YFP-mts reconstitution on liposomes: state of the art and scientific inquiry formulation

To understand the role of FtsZ in the physical process of creating constriction, studies of FtsZ deforming liposomes were pioneered by Erickson's lab. FtsZ-YFP-mts was reconstituted inside tubular liposomes (Fig. II.3C) to produce FtsZ contractile rings and constriction necks. [69]. In addition, this same mutant reconstituted outside multilamellar liposomes caused inwards deformations [70]. Interestingly, by switching the membrane targeting sequence to the N-terminal (mts-FtsZ-YFP), outwards were obtained. Similar results were also evidenced in GUVs [7]. To explain this phenomenology, Erickson and coworkers conceived an intrinsically curved FtsZ filament with an attachment direction parallel (N-terminal) or antiparallel (C-terminal) to the curvature vector (Fig. IV.1). From this evidence, one can conclude that FtsZ exerts remodeling forces related to its curvature and direction of attachment; however, a clear mechanistic description on these forces remains elusive.

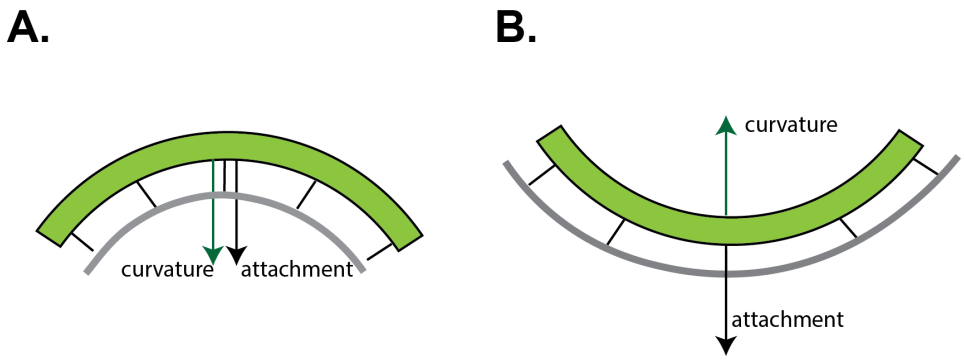

Figure IV.1: Erickson's model for FtsZ deformations. A) (mts-FtsZ-YFP) When attachment direction is parallel to intrinsic FtsZ-filament curvature, outwards deformations are observed. B) On the contrary (FtsZ-YFP-mts), attachment is anti-parallel to curvature producing inwards deformations.

Although Erickson and coworkers also observed rings inside GUVs [72], our findings of FtsZ-YFP-mts forming rings on flat surfaces (SLBs) [82] clearly opened the discussion whether Erickson's model (Fig. IV.1) could explain ring formation in a flat geometry. To explain this and reformulate Erickson's model, we proposed that the vector defining the filament-attachment also needed a perpendicular-component (to curvature) in such way that i) explains ring formation over flat surfaces and (b) switching the mts-location from C-terminal to N-terminal inverts chirality, as experimentally observed [82]. Intriguingly, the fact that switching treadmilling direction for mts-FtsZ-YFP rings resulted in the inversion of force direction indicated that growth polarity (in addition attachment and curvature) determined force direction. In light of the evidence showing that FtsZ forms helical structures in vivo [33, 39, 65, 103] and in vitro [7], we have proposed that an FtsZ filament with more than one main direction of curvature, such as a helix, would much more elegantly accommodate the combination of inward/outward deformations and chiral treadmilling for the opposite mts mutants [82]. In our recent work, we have hypothesized that, on deformable surfaces (deflated liposome), a growing filament would either pull or push depending on the direction of attachment (Fig. II.16) [82]. Then, to investigate this possible FtsZ "helical motif" or "twist", we will study the impact of FtsZ on soft lipid tubes pulled from deflated GUVs.

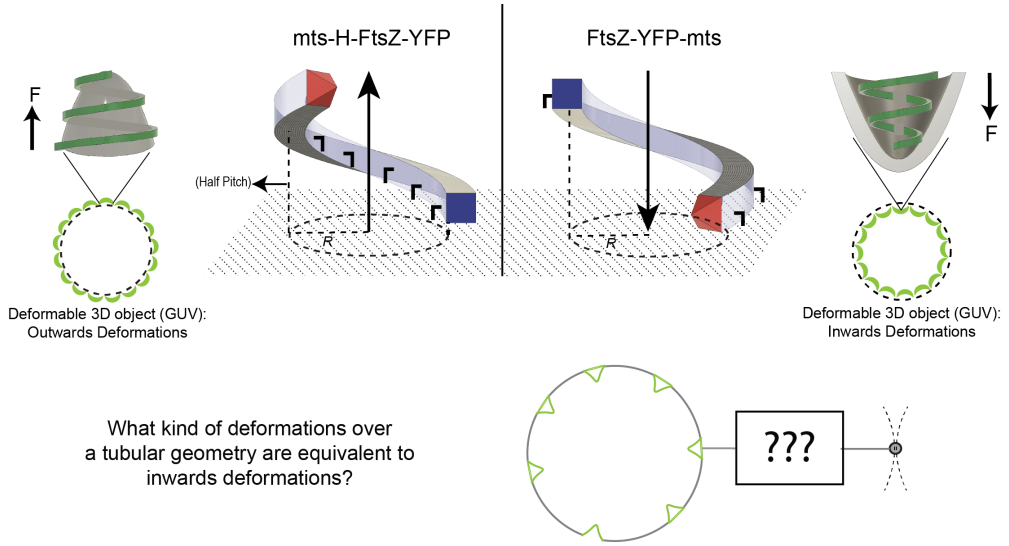

Figure IV.2: What kind of deformations over a tubular geometry are equivalent to inwards deformations?

IV.1.2 A (very) brief introduction to elastic deformations, torsion and polymer physics

The purpose of this section is to formulate equations for the elasticity and torsion of a beam in light of basic concepts of polymer physics such as persistence length and flexural rigidity. Let's first consider a small-beam with a cross-section A and an initial length l_0. If the beam is subjected to two opposite perpendicular forces, it will be stretched to have a new length l. The force divided by the cross-sectional area A is defined as the normal stress $\sigma = F/A$ whereas the normal strain is $\epsilon = (l - l_0)/l_0 = \delta l/l_0$ (Fig. IV.3 A). For most of materials subjected to small stresses, the stress scales linearly with the strain with a proportionality-constant called the Young's modulus (Y) [104]:

$$\sigma = Y\frac{\delta l}{l_0} = Y\epsilon \tag{IV.1}$$

Now, let's assume that the same small beam has height h and a tangential force F_t (Fig. IV.3 B) applied to the upper surface (point O is kept fixed). This force creates a δx displacement defining an angle as α with respect to O. The shear stress τ is defined as F_t/A and shear strain $\gamma = \delta x/h$. To generalize normal and shear stresses, we can consider

the same small beam with stresses acting on the six sides of the cubic element: $\sigma_x, \sigma_y, \sigma_z$ for normal stresses and $\tau_{xy} = \tau_{yx}, \tau_{xz} = \tau_{zx}, \tau_{yz} = \tau_{zy}$ for shear stresses (Fig. IV.3 C). Stresses are coupled in such way than an extension in x, for example, implies lateral contractions in y and z. This contraction is proportional to ν, the Poisson's ratio [104].

$$\epsilon_x = \frac{\sigma_x}{Y} \quad \epsilon_y = -\nu\frac{\sigma_x}{Y} \quad \epsilon_z = -\nu\frac{\sigma_z}{Y} \tag{IV.2}$$

Then, we can write strain equations considering the contributions from perpendicular directions to the normal stress [104]:

$$\epsilon_x = \frac{1}{Y}[\sigma_x - \nu(\sigma_y + \sigma_z)] \quad \epsilon_y = \frac{1}{Y}[\sigma_x - \nu(\sigma_x + \sigma_z)] \quad \epsilon_z = \frac{1}{Y}[\sigma_x - \nu(\sigma_x + \sigma_y)] \tag{IV.3}$$

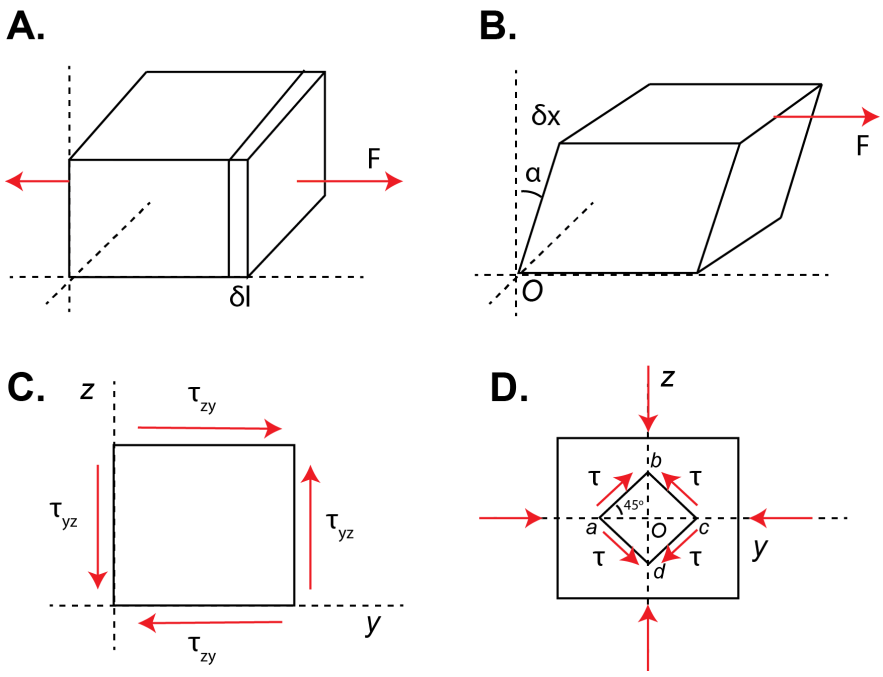

Figure IV.3: Normal and shear stress.

Now, let's define a rectangular section (Fig. IV.3 D) having $\sigma_y = -\sigma_z$ and $\sigma_x = 0$. Considering the inside element defined by the segments *abcd* and indicated shear stresses (Fig. IV.3 D), the shear stress τ can be written as $\tau = 1/2\,(\sigma_z - \sigma_y) = \sigma_z$ ("pure shear condition"). The vertical stretching of the segment *Ob* is coupled to the shortening of

segments Oa and Oc (Fig. IV.3 D). The angle between ab and bc corresponds to the shear-strain after deformation [104]:

$$\frac{Oc}{Ob} = \tan\left(\frac{\pi}{4} - \frac{\gamma}{2}\right) = \frac{1+\epsilon_y}{1+\epsilon_z} \tag{IV.4}$$

Using the "pure shear condition" and equations IV.3, γ (from IV.4) can be written in terms of σ_z. Therefore, we obtain a "hooke-like" expression for the shear stress in terms of G, the shear modulus [104].

$$\gamma = \frac{2(1+\nu)\sigma_z}{Y} = \frac{2(1+\nu)\tau}{Y} \qquad \gamma = \frac{\tau}{G} \tag{IV.5}$$

Now, we can formulate an equation for the torsion of a circular rod with radius r. The shear-strain of a dx and $d\phi$ section (Fig. IV.4) with ρ, the distance from the center, is defined as $\gamma = (d\phi/dx)\,\rho$. Note that the quantity $d\phi/dx$ defines the angle of twist per unit length . Therefore, the shear-stress is calculated as $\tau = G(d\phi/dx)\,\rho$. The force acting over an area-differential dA results $dF = \tau dA$, then the torque equals $dT = \rho dF$. By integrating this expression over the whole area, we obtain the total torque driving the cylinder twisting [104]:

$$T = G\frac{d\phi}{dx}\int \rho^2 dA \qquad \frac{d\phi}{dx} = \frac{T}{G\cdot J} \tag{IV.6}$$

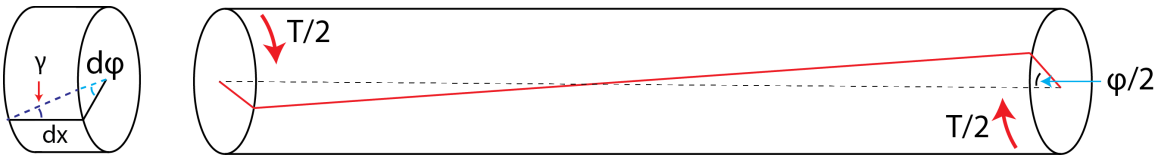

Figure IV.4: Twisting a circular beam.

where J refers to polar moment of inertia of the cross-sectional area. In a first approximation, one can consider that the twisting angle is constant over L; then [104]:

$$\frac{T}{\phi} = \frac{G\cdot J}{L} \qquad J = \frac{\pi r^4}{2} \tag{IV.7}$$

On the other hand, cytoskeleton proteins such as actin or tubulin form polymers in a length-scale of a cell: -micrometers- [15]. These polymers are well modeled by inextensible elastic rod with finite resistance to bend or twist, a worm-like chain. The bending energy for this worm-like polymer is proportional to K, the bending constant (flexural rigidity), and the square of the local curvature [15]:

$$F_{bending} = \frac{K}{2} \int ds \left| \frac{\partial \vec{t}}{\partial s} \right|^2 \tag{IV.8}$$

This flexural rigidity is proportional to the Young's modulus Y and a geometrical constraint called the area moment of inertia I. For the case of a solid rod-like polymer with radius r, we obtain [5, 15]:

$$K = Y I \qquad I = \frac{\pi r^4}{4} \tag{IV.9}$$

In addition, the flexural rigidity has units of energy $\times$ length. Then, by comparing this energy to thermal energy, we obtain the persistence length [5, 15]:

$$l_p = \frac{K}{k_B T} \tag{IV.10}$$

In plain words, the persistence length refers to the characteristic length where the polymer remains straight [5]. A semi-flexible polymer require of a high bending energy implying that straight conformations win over entropic clustering. However, due to thermal fluctuations, small angle deformations can occur and become more likely for lengths longer than lp. This implies that the closer points inside the filament are likely to exhibit the same orientation while distant point are likely to have a different orientation [5]. This can be quantitatively expressed by the orientation auto-correlation function:

$$C(s) = \langle \cos(\theta) \rangle = e^{-|s|/l_p} \tag{IV.11}$$

where s in the contour between two points and θ the angle difference between the filament tangents [5].

IV.2 Bidirectional FtsZ treadmilling promotes membrane constriction via torsional shear stress

The work of this section belongs to a manuscript in preparation:

Diego A. Ramirez-Diaz, Adrian Merino-Salomon, Michael Heymann, Petra Schwille (2019).

Bidirectional FtsZ treadmilling promotes membrane constriction via torsional shear stress

IV.2.1 Introduction

Fundamental biological processes, such as cell division and constriction, require an intricate space-time coordination of respective functional elements. However, how these elements, (proteins), can self-assemble in larger spatial scales (compared to its own-size) and exert forces driving large-scale membrane transformations is poorly understood. In several organisms, ring-like cytoskeletal elements appear to drive or support cytokinesis; for instance, the FtsZ contractile-ring in bacteria. When reconstituted on flat membranes, FtsZ self-assembles into rotating-treadmilling vortices with a conserved direction [53, 82]. Consequently, in vivo, FtsZ possess circumferential, but non-directional, treadmilling that serves as a pacemaker to guide peptidoglycan synthesis [11, 117]. To determine whether FtsZ-forces actively contribute for bacteria cytokinesis, the physical principles behind constriction should first be understood. Therefore, using a novel approach to produce soft lipid tubes from giant unilamellar vesicles GUVs, our aim here is to establish what physical principles drive membrane-deformations produced by FtsZ-YFP-mts dynamic rings on GUVs and the scale of the delivered forces.

IV.2.2 Results and Discussion

Based on the findings on our recent study [82], we externally added FtsZ-YFP-mts to GUVs made of E.coli lipids. The conditions to obtain ring-like structures were determined by tuning GTP and Mg^{2+} content (Fig. IV.5 A). Since no deformations were observed in the case of tensed vesicles (Fig. IV.5 A), we designed a two-side open chamber allowing

slow evaporation of the outside buffer to obtain deflated GUVs and deformable membranes. After 30 minutes, we have observed that rings were inducing drilling-like inwards forces shaping inwards cones (Fig. IV.5 B). Although similar observations have been previously reported [7,70], the emergence of these deformations from dynamic ring-vortices is a novel phenomenology. Motivated by the cone-like geometry, we designed microstructures in PDMS having inwards cones of size of 2.6 μm upper diameter and 4 um depth (Fig. IV.5 C Fig 1S A). Then, after coating with a SLB and triggering protein polymerization, we observed individual filaments/bundles wrapping the cone in a dynamic fashion resembling a vortex (Fig. IV.5 D). Strikingly, we noticed that the dynamic vortices possess clockwise/anticlockwise directions represented here in the kymograph (Fig. IV.5 E) indicating that preferential directionality observed in flat-SLBs is absent when geometry is altered. Rotational velocities in both directions can be estimated around 43 nm/s showing good agreement with our previous results on flat surfaces (34 nm/s) [82]. These results also support the assumption of a helical architecture of FtsZ [101]. Around the preferential diameter within the cone, a polar FtsZ helix will show clockwise treadmilling if it grows top-to-bottom and anticlockwise in reverse (bottom-to-top).

To explore the impact of FtsZ on soft tubular geometries, we developed a new technique using optical tweezers. Contrary to prior approaches using micropipettes to hold GUVs [80, 89] we can pull soft tubules from (low membrane tension) GUVs that are weakly attached to the surface (Fig. 2S A). Right after the streptavidin-coated bead bounded biotinylated-GUVs, GUVs were moved away and tubes with a mean diameter around 0.48 μm were formed (Fig. 2S B). More interesting, we pulled tubes from deflated GUVs decorated with ring like FtsZ structures and inwards deformations. Once tubes were formed, protein filaments started to enter the tube, producing small tube deformations. After 175s, helical deformations were clearly observed (Fig. IV.6 A) indicative of dynamic coiling and winding. Analogously to the two-treadmilling directions of filaments (Fig. IV.5 E), clockwise winding (pointing inwards) drives a lateral movement towards the tip, while the counter-clockwise cause the opposite. An estimation of the diffusion constant for these helical objects (size $\sim$ 1 μm) was around 0.1 μm^2/s (Fig. IV.6A, white box) indicating the possibility of an active process compared to passive lateral diffusion of membrane proteins [81]. As more protein entered the tube and accumulated in the tip, there is compression of the spring (Fig. IV.6 A, 500s). These helical membrane tube deformations can be rationalized by twisting of an elastic rod subjected to constant tensile force (Fig. IV.7 C). Similar to the experiment in Figure IV.5D, we have filaments that grow towards (clockwise) and away

(counterclockwise) the tip of the tube. If filament growth imposes torsion (clockwise), the counter-filament will generate a torsion in the opposite direction. These two different torsion contributions result in the buckling of the lipid tube and the formation of a three dimensional helix (Fig. IV.7 C). As previous studies have proposed, FtsZ torsion is here understood as an offset angle between of two adjacent monomers [41,91]. Further evidence for torsion can be found in tubes exhibiting plectonic/supercoiled regions (Fig. 1S E).

To investigate the role of GTP hydrolysis, we reconstituted FtsZ-YFP-mts*[T108A] on GUVs, a mutant that has low GTPase activity [82]. Using comparable conditions, we observed that FtsZ-YFP-mts*[T108A] also self-assembled into ring-like structures (Fig. 1S B) driving inwards cone-like deformations (Fig. 1S C). Since those rings lack dynamic treadmilling [82] yet promote similar inwards deformations, we studied the impact of FtsZ-YFP-mts*[T108A] on a tubular geometry. Interestingly, diffusion of FtsZ-YFP-mts*[T108A] was significantly slower (Fig. 2S C). Strikingly, after 350s, helical deformations were observed (Fig. IV.6 C). After imaging more than 900s, we noticed that long pitch deformations ($\lambda > 3\,\mu m$) remained unchanged. In contrast, FtsZ-YFP-mts achieve smaller pitch deformations (Fig. IV.6 B) that underwent further compression after 300s ($\lambda \sim 1.5\,\mu m$). Furthermore, we quantified the tube deformation by measuring the arc length compared to its initial length. By plotting this against the FtsZ tube density, we observed that the ability to deform membranes is greater for the GTPase activity case (Fig. IV.7A). Note that experiments shown in Fig IV.6B-C corresponded to a tube with similar diameter ($d = 0.44\,\mu m$ Fig. 2S B). Therefore, we also tested whether further compression could be biased by GUV-deflation-state (membrane reservoir) and the tube protein density. Although there was a mild correlation among mean-pitch λ and tube diameter (Fig. 2S E), a longer mean-pitch is clearly dominating for FtsZ-YFP-mts*[T108A] (Fig. 2S E-F). In addition, we also plotted the pitch distribution and found two pitch states for FtsZ-YFP-mts and FtsZ-YFP-mts*[T108A] (Fig. IV.7 B). As a result, we suggest that FtsZ has an intrinsic torsion than is enhanced by GTPase activity (driving compression). The intrinsic FtsZ torsion ruled large pitch transformations ($\lambda > 3.5\,\mu m$) while GTP enhances torsion causing lower pitch states ($\lambda < 1.5\,\mu m$). Intermediate pitch ($2\,\mu m < \lambda < 3.5\,\mu m$) could correspond to combination of intrinsic torsion and GTPase activity.

Since tube pulled vesicles exhibited position-fluctuations, absolute force measurements were difficult. However, to assess the mechanical properties of spring-like structures induced by FtsZ-YFP-mts, we implemented a novel approach based on the tube elastic response to

a specific dynamic input. Using a piezoelectric stage, we set an oscillation of the vesicle with an amplitude of 3 μm and frequency 1 Hz (Fig. IV.8 A). In this way, we can measure signal amplitudes at only 1 Hz frequency. Therefore, we recorded the force by tracking the trapped bead displacement. To model the system, we considered a spring-constant contribution of the lipid (k_{lipid}) in a parallel configuration with FtsZ (k_{FtsZ}) (Figure IV.8 C). The dynamic response of the optical tweezers is depicted in Figure IV.8 B, where red line refers to the lipid tube and green for lipid+protein. By calculating the amplitude of the signal, we could measure a spring constant k_{lipid}=0.5 $\pm$ 0.12 pN/μm. Next, we measured the spring constant (green line, Fig. IV.8 B) of helical FtsZ shaped tubes by subtracting the lipid contribution: k_{FtsZ}=0.36$\pm$0.1 pN/μm. Using this value, we could estimate the required force to compress the spring from low to high pitch which corresponded to the GTPase activity torsion contribution. Forces in the range $0.6 - 1$ pN were delivered due to GTPase activity. Note that this force is used to pull lipid from the GUV to be incorporated in the spring-like structure.

In addition, we could estimate the FtsZ Young's modulus using k_{lipid} and k_{FtsZ} using the two-spring modeling. By definition, the Young's modulus is related to the spring-constant k_s by $E = k_s l_0/S$, where l_0 the initial length of the spring and S the cross-section. Since S and l_0 were similar for our experiments, we could write FtsZ Young's modulus $E_{FtsZ} = (k_{FtsZ}/k_{lipid})E_{lipid}$ in terms of E_{lipid}. The bending modulus κ_b of lipid bilayers is between $10 - 20\, k_B T$ [10,76,89] which corresponds to a $E_{lipid} = 11.5 - 23$ MPa. Therefore, the FtsZ helical configuration exhibited a Young's modulus around $8.2 - 16.4$ MPa. Given this value, the bending rigidity and the persistence length can be inferred. For estimating the bending rigidity, we needed to calculate the area moment of inertia for a rod-like polymer $I = \pi a^4/4$ where a refers to an effective-radius of the polymer. Since FtsZ-YFP-mts is prone of bundling in presence of Mg^{2+} [61,82], we explored the impact of bundling in the persistence length $l_p = EI/k_B T$. We here used the persistence length found for FtsZ-rings on SLBs: $l_p = 0.39$ μm [82] as reference to assess the plausibility of our calculations. Bundles with an effective radius of one $n = 1$ or $n = 3$ FtsZ-monomers (diameter: 4 nm) resulted in $l_p < 0.09$ μm and $l_p > 3.5$ μm respectively. For $n = 2$, l_p values between $0.7 - 1.4$ μm were comparable to measured values in SLBs. This persistence length was significantly lower than microtubules $\sim 1.4 - 5.2$ mm [34,110] and lower than to actin ~ 18 μm [34,110]. Consequently, the bending rigidity EI was found to be $K = 2.6 - 5.2 \cdot 10^{-27}$ $N \cdot m^2$ showing good agreement with a previous report [109]. This value was significantly lower than microtubules $\sim 10^{-23}$ [110] and one order of magnitude lower than actin ($\sim 10^{-26}$) [108]

indicating that FtsZ bundles were significantly softer than other cytoskeleton proteins despite of its globular nature.

The helical transformation caused by FtsZ filaments is understood if there is torque around the lipid tube. Darboux torques are tangential torques caused by a local mismatch between the plane defined by the (unbound) filament-curvature and the membrane attachment direction ("adhesive stripe") [74]. To bind, filaments have to "stress" to align to the membrane; however, this stress is released by inducing a "spin" on its internal frame, the Darboux frame [30]. This twisting angle or "rotation" along the filament is key to produce torque. A molecular dynamics study have shown that dynamin, an endocytic-constriction helical protein, required of "rotation of the adhesive stripe" to achieve full membrane hemifusion [74]. This "rotation" was justified by the observation of tilting of PH-domains in dynamin-crystal-structure [46]. In the FtsZ case, molecular dynamics studies have predicted an angle of "twisting" between monomers . In addition, Fierling and coworkers have theoretically studied membrane deformations produced by filaments inducing Darboux-like torques [30]. Strikingly, they found inwards vortex-like deformations (flat surface) and spring-like shapes when filaments wrapped a tubular geometry. These predictions remarkably agreed with our observations. Along these lines, we can estimate the generated FtsZ-torque over one persistence length: $T/\phi = (G \cdot J)/l_p$ where G represents the shear modulus and $J = 2I$. As a result, FtsZ could deliver torques around 1.2 pN·nm/rad. As expected, this value was significantly lower than, for example, the ATP synthase FoF1 subunit (31.2 pN·nm/rad) [105] or dynamin ($\sim$ 500 pN·nm/rad) [62].

To investigate the influence of FtsZ-inside-geometry and confinement, we reconstituted FtsZ-YFP-mts and FtsZ-YFP-mts*[T108A] inside giant unilamellar vesicles (GUVs) using regular double emulsion techniques [75] (Fig. IV.9 A). The conditions to obtain rings-like-structures (Fig. IV.8 B) or also longer filaments wrapping the vesicle (Fig. 1S D) were also determined by tuning GTP and Mg^{2+}. Interestingly, the diameter of rings ($N > 100$) made of FtsZ-YFP-mts*[T108A] was significantly larger (0.89 μm) compared to case having regular GTPase activity (0.44 μm) (Fig. IV.9 C). This difference was not observed in the case of supported lipid bilayer (SLBs) [82] meaning that either surface-to-volume ratio or a softer lipid-surface determined the steady state of assembly. In addition, the wide size distribution, in the case of the GTPase mutant (Fig. IV.9 D), implied that polymers are flexible enough to accommodate a larger variety of curvatures. Strikingly, both FtsZ mutants could create outwards deformations emerging from ring-like structures (Fig. IV.10

A). In the case of FtsZ-YFP-mts, there was a clear formation of condensed and constricting rings (Fig. IV.10 A) similar to previous reports [69]. Based on our results (Fig. IV.6), we hypothesize that FtsZ torque could create outwards out-of-plane forces (Fig. IV.10 B). However, these FtsZ filaments exhibiting intrinsic torsion state are unable to mechanically-stabilize smaller diameters. In contrast, further twisting upon GTP hydrolysis drives constriction and clustering (Fig. IV.10 C). Upon GTP hydrolysis, FtsZ filaments became rigid and mechanically stable with smaller diameters ($\sim 0.5\ \mu m$). FtsZ constriction and neck formation represents an equivalent situation of helix-compression when protein was external to the tube. Therefore, we can estimate the force required for constriction based using k_{FtsZ} and the difference between relaxed-compressed state $0.6 - 1$ pN.

We have here shown that FtsZ can induce deformation forces via Darboux torques. Intrinsic FtsZ torsion ruled the assembly of ring-like structures on flat surfaces and inwards/outwards tubular deformations (Fig. IV.10 A). Regardless whether protein is externally added or encapsulated, the cylindrical geometry allows clockwise/anti-clockwise growth since both are geometrically equivalent (Fig. IV.5 E). Clockwise torsional stress is counteracted by anticlockwise stress driving a helical transformation of a lipid tube when protein binds from outside. For the encapsulated situation, we hypothesize that clockwise/anticlockwise intrinsic FtsZ torsion could create not-mechanically-stable constriction-necks. In this case, no treadmilling is evidenced. In contrast, we also suggest that GTP hydrolysis triggered a super-constricted state favoring higher curvatures. However, this super-twisted state imposed a mechanical strain on filaments causing filament breakage (Fig. IV.10 C). In this case, FtsZ clockwise/anticlockwise treadmilling occurs, as observed *in vivo* [11,117]. In this context, a remarkable similarity between FtsZ with the GTPase dynamin can be mentioned. Current models suggested that dynamin-helical-polymers could constrict lipid nanotubes via torsion [6, 62]. Likewise, GTP hydrolysis triggers a super-constricted state favoring fragmentation and clustering [17, 102]. Based on this, we conclude that torsion and Darboux torques represent a robust strategy to deform membranes among prokaryotic to eukaryotic organisms. In addition, here reported FtsZ forces may not suffice bacteria cell division (~ 2 pN); however, this force could induce neck-formation if membrane low tension is achieved. This could be achieved through the incorporation of *de novo* synthesized lipids, as recently hypothesized [73].

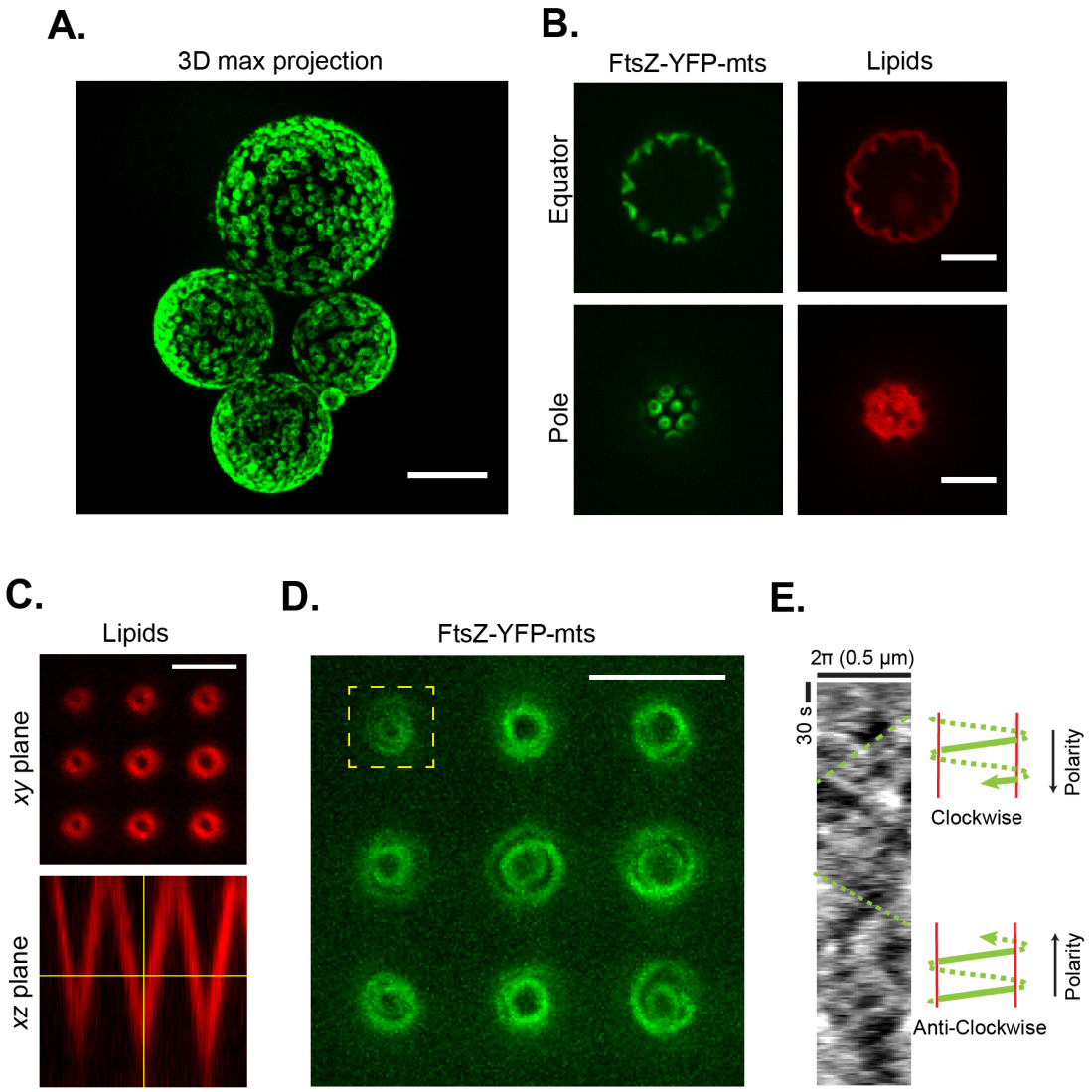

Figure IV.5: FtsZ-YFP-mts self assembles into rings that produce inwards conical deformations. A) GTP and Mg^{2+} conditions were optimized to obtain FtsZ-YFP-mts ring structures externally decorating GUVs (scale bar=10μm). B) After GUV deflation, inwards conical deformations emerged from FtsZ ring-like structures. C) Inspired by deformations in B), we designed a PDMS microstructure with a inwards conical geometry to be covered with a supported lipid bilayer. The imaging plane is chosen to have a cross-section of ~ 1 μm diameter. D) Inside this conical structure, FtsZ-YFP-mts self assembles into dynamic vortices. E) Kymograph analysis shows negative and positive slopes indicating the presence of clockwise and anticlockwise directions. Both velocities are close to 43 nm/s (Scale bar = 5 μm).

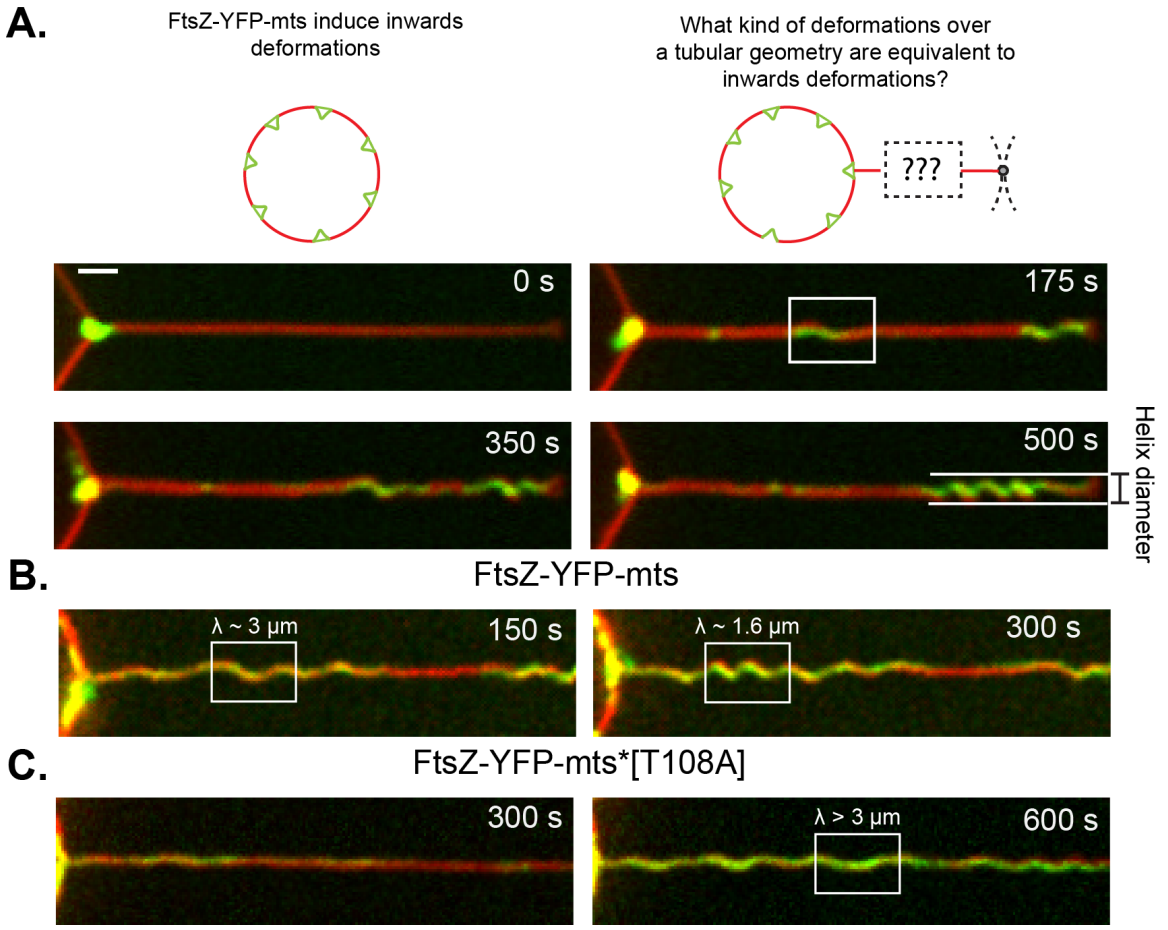

Figure IV.6: FtsZ-YFP-mts induced spring-like deformations over a soft tube. A) To understand the nature of FtsZ inwards deformations, we stretched this deformation over a tubular geometry pulled using optical tweezers. FtsZ-YFP-mts caused spring-like deformations exhibiting coiling and winding. Tubes of same diameter were pulled from GUVs decorated with B) FtsZ-YFP-mts and C) FtsZ-YFP-mts*[T108A], a mutant with no GTPase activity. Both proteins generated spring-like deformations with the difference that GTPase activity (green dots) induce fast spring ($\lambda \sim 1.6\mu m$) compression compared to a slow and low pitch deformation ($\lambda \sim 4\mu m$) for the low GTPase mutant.

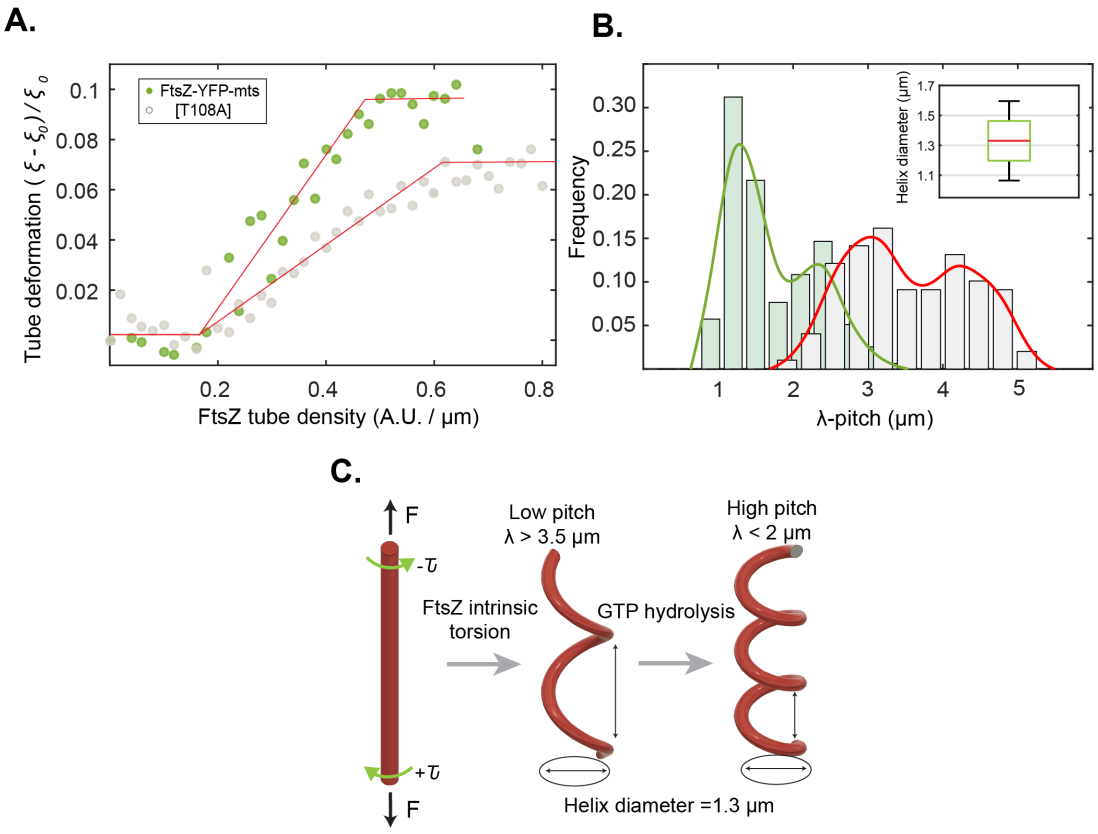

Figure IV.7: FtsZ-YFP-mts induced spring-like deformations over a soft tube II. A) We evidenced that GTPase activity causes higher deformation level by measuring tube deformation as a function of FtsZ tube density B) We measured the pitch (or wavelength) of spring-like deformations and observed two clear pitch states for FtsZ-YFP-mts (green bars/line): relaxed ($\lambda \sim 2.5\,\mu m$) and compressed ($\lambda \sim 1.5\,\mu m$). On the other hand, FtsZ-YFP-mts*[T108A] (gray bars/red line) also displayed two different pitch states: relaxed ($\lambda \sim 4\,\mu m$) and compressed ($\lambda \sim 3\,\mu m$). C) These helical deformations are well understood by twisting an elastic rod subjected to constant tensile force. We postulate that FtsZ has an intrinsic torsion than is enhanced by GTPase activity driving further compression. The intrinsic FtsZ torsion lead low pitch transformations ($\lambda > 3.5\,\mu m$) while GTP enhances torsion causing higher pitch states ($\lambda < 1.5\,\mu m$). Intermediate pitch states ($2\,\mu m < \lambda < 3.5\,\mu m$) could correspond to the competition between intrinsic torsion and GTPase activity. This implies that some residual GTPase activity of the mutant FtsZ-YFP-mts*[T108A] could slightly increase pitch.

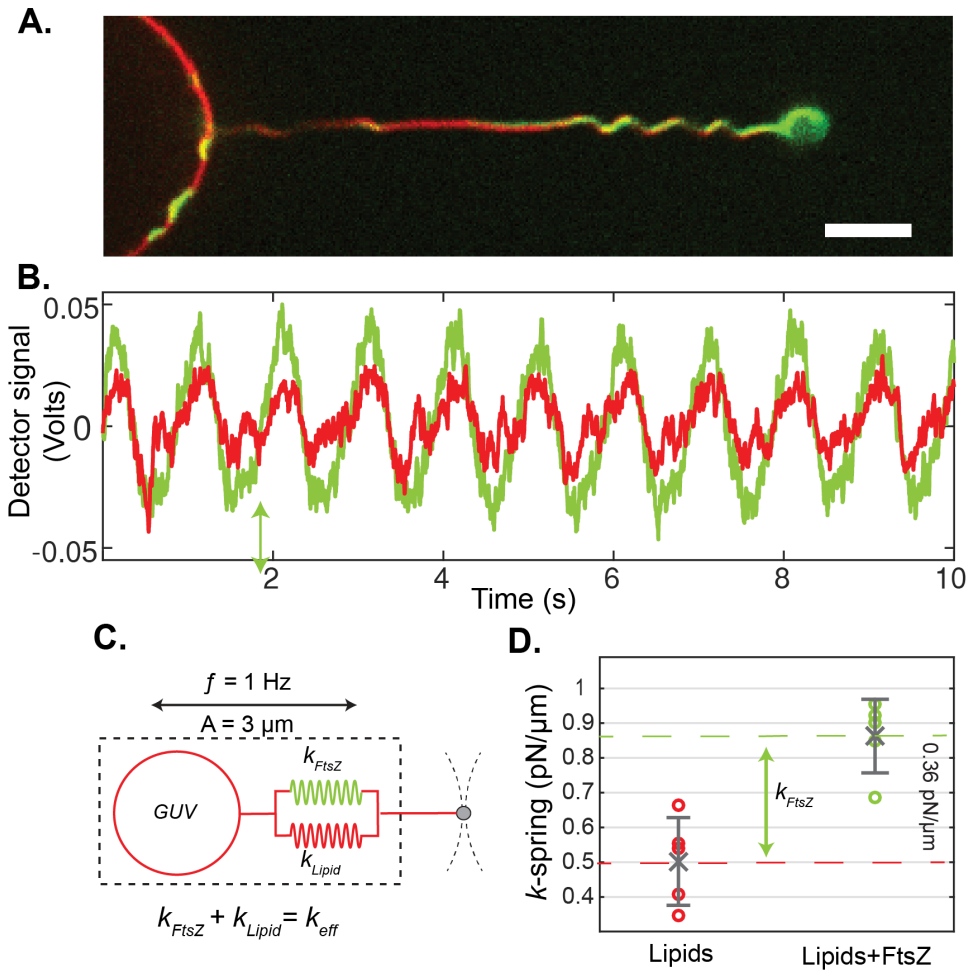

Figure IV.8: Measuring FtsZ-spring constant. A) Spring-like structures induced by FtsZ-YFP-mts were mechanically assessed by C) forcing the the GUV oscillate with an amplitude of 3 μm and a frequency of 1 Hz. To model the system, we consider a spring-constant contribution of the lipid in a parallel configuration with the FtsZ contribution (Scale bar = 5 μm). B) Using a force detection module, we could track the displacement of trapped bead as a response of the dynamic input. Red line corresponded to the lipid signal and green line to FtsZ. D) By calculating the amplitude of the signal, we could measure the FtsZ spring constant k_{FtsZ}=0.36±0.1 pN/μm.

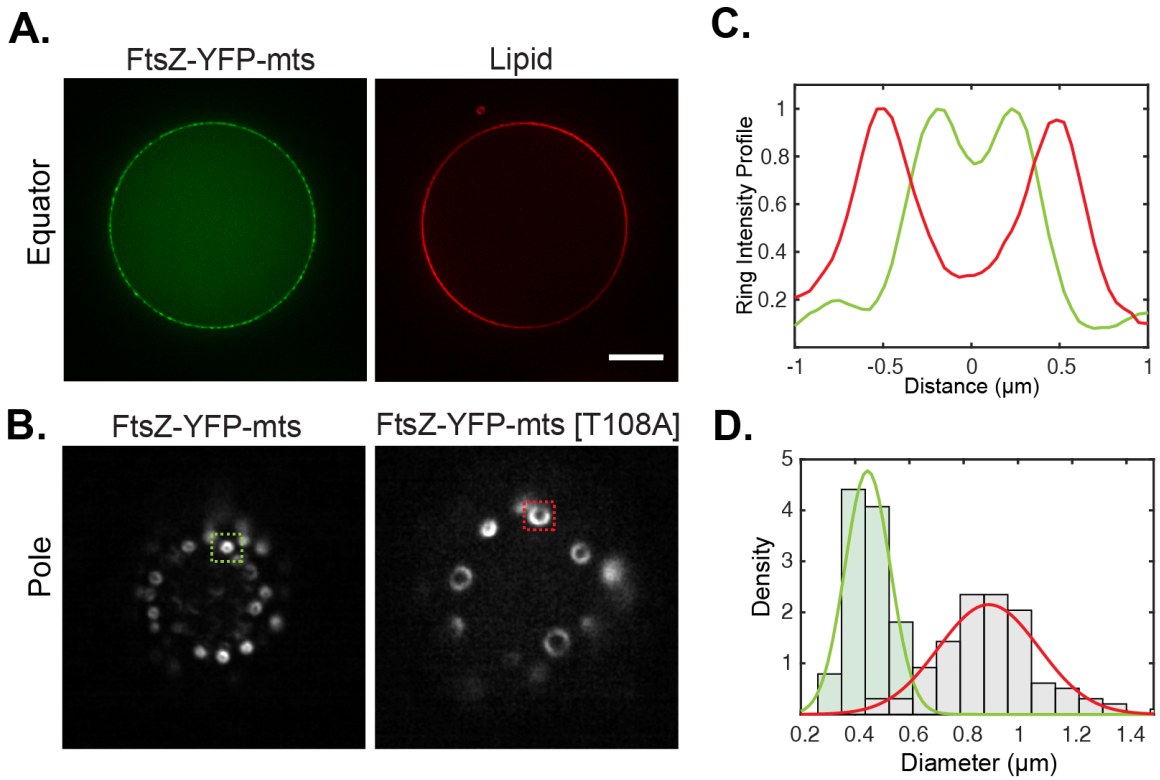

Figure IV.9: Encapsulation of FtsZ in GUVs. A) GTP and Mg^{2+} conditions were found to obtain FtsZ-YFP-mts and FtsZ-YFP-mts*[T108A] ring structures inside GUVs (Scale bar = 5 μm). B) Appropriate imaging of rings was possible at the bottom of the GUVs using TIRF microscopy. C) Light intensity profile of indicated structures in B) shows that FtsZ-YFP-mts (green line) rings exhibit smaller diameter than FtsZ-YFP-mts*[T108A] (red line). D) Size distribution of FtsZ-YFP-mts*[T108A] (gray bars and red line) and FtsZ-YFP-mts showed a drastic reduction in ring diameter due to GTP hydrolysis.

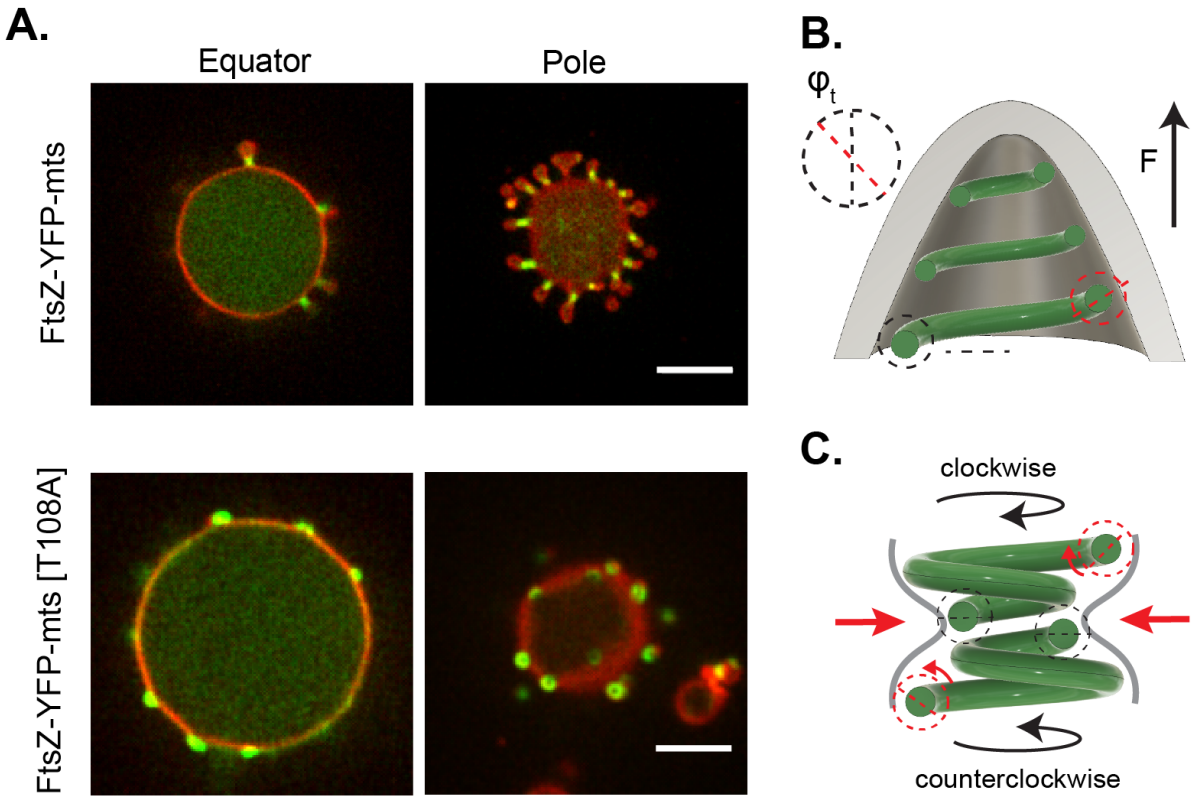

Figure IV.10: Inside-torsion generated -GTPase dependent- constriction necks. A) After deflation, both mutants drive outwards deformations with the difference that GTPase activity promotes constriction and neck formation. B) We suggest that intrinsic torsion can create out plane forces; however, C) GTP hydrolysis triggers a super-constricted state favoring higher curvatures. This super-twisted state imposes a mechanical strain on the filament that causes filament breakage and FtsZ clockwise/anticlockwise treadmilling (Scale bar = 5 μm).

IV.2.3 Materials and Methods

Confocal spinning disk imaging

Confocal spinning disk imaging was performed using a Yokogawa CSU10-X1 spinning disk system connected to a Nikon Eclipse Ti inverted microscope (Nikon, Japan). A DPSS laser stack with 488 nm, 561 nm and 640 nm laser lines (3i, Denver, Colorado USA) is used for illumination and an Andor Ixon Ultra 512 × 512 EMCCD camera for fluorescence detection. 3i-Slidebook software controlled lasers, filter selection, microscope, xy stage and acquisition (3i, Denver, Colorado USA). For simultaneous FtsZ-YFP-mts and ATTO655-DOPE excitation, 488 nm and 640 nm lasers were rapidly switched by an AOTF. For image detection, the use of an appropriated quad-band-filter avoided mechanical filter switch. Samples were images using a CFI Plan Apochromat Lambda 100X oil, $NA = 1.45$ (Nikon, Japan).

FtsZ rings reconstitution in vesicles

FtsZ externally added to vesicles and tube experiments with force detection.

Giant unilamellar vesicles (GUVs) were produced using electro-swelling as described elsewhere (ref). E.coli lipid extract was dissolved in chloroform to reach a final concentration of 3mg/ml. To image lipids in the red channel, 0.05 % (mol) of ATTO655-DOPE (ATTO-Tech GmbH, Germany) was added to the lipid mixture. In addition, 0.15% of DSPE-PEG (2000) Biotin (Avanti, AL, United States) was also added to achieve binding between GUVs and streptavidin-coated beads. In our home-made Teflon chambers, 3 drops (~ 1 μl) were carefully seeded in Pt wires and rapidly air dried. After 1h vacuum for further chloroform drying, GUVs were swelled in 250 mOsm sucrose solution at 10Hz for 2 hours and 2Hz for 1 additional hour (detachment). Lipid concentration and electroformation times were carefully optimized to guarantee an appropriated GUV yield. Furthermore, to obtain similar GUV-lipid concentrations, two identical chambers underwent same procedure and mixed afterwards.

GUVs were mixed in buffer (120 mM KCl, 20 mM Tris-HCl, and 1.5 mM $MgCl_2$ pH 7.5) with an osmolarity of 250 mOsm. In details, 4 μl of GUVs were highly diluted in 380 μl of buffer in a reaction tube. FtsZ-YFP-mts and FtsZ-YPF-mts*[T108A] were added to reach a final concentration around 0.07 μM. Polymerization is triggered by adding 1.25

mM of GTP (Sigma, Germany). Flaccid vesicles with FtsZ rings and inward deformation were observed after 20 mins. On these vesicles, tubes were pulled and imaged for 10 minutes (1 fps) in two-colors: FtsZ-YFP-mts and lipid channel. This time was enough to obtain helical deformations and reach a steady state of protein entering the tube, at least for FtsZ-YFP-mts. To analyze pitch, N=11 experiments for FtsZ-YFP-mts and N=9 for FtsZ-YFP-mts*[T108A] were analyzed (see Image Analysis below). Right after this 10 mins time, force measurements (oscillations) were performed for 60 seconds. Experiments with pulled tubes longer than 10 minutes were prone to gain contamination in the "force channel" (beads, vesicles and protein clusters were attracted by the optical trap). This made force measurements for FtsZ-YFP-mts*[T108A] highly difficult since the timescale of deformation was significantly longer. To estimate spring-constants, we used the oscillation mode as described above. Force experiments (N=5) were carried out in tubes without protein to be contrasted to experiments with FtsZ-YFP-mts and helical deformations (N=5). As mentioned above, data was acquired in Matlab (Mathworks, USA) and signal-amplitude determined by the amplitude of the FFT (Fast Fourier Transformation) at 1 Hz. Then, this values is converted to force using volts/μm conversion and trap stiffness and lastly divided by the oscillation amplitude ($A = 3$ μm).

FtsZ encapsulated in lipid vesicles

FtsZ encapsulating vesicles were produced using droplet emulsion transfer [75]. Lipid composition was EggPC/DOPG 80:20 (Avanti, AL, United States) with 0.05% mol ATTO655-DOPE (ATTO-Tech GmbH, Germany). Briefly, vacuum dried lipids were dissolved in mineral oil (Sigma, Germany) to reach a final concentration of 0.5 mg/ml. To form lipid vesicles, two interfaces are required: outer and inner interface. In a reaction tube (A), 500 μl of lipid+oil mixture was added to 500 μL of outer buffer (150 KCl 50 mM Tris-HCl pH 7.5). At the oil-water interface, a lipid monolayer was assembled after 30 minutes. In a second reaction tube, 15 μl of protein-master-mix was added 500 μl of lipid+oil and vigorously vortexed for two minutes to obtain a homogenous cloudy emulsion. The inner monolayer was rapidly formed ($\sim$ 2 minutes). This protein-master-mix was composed of inner buffer (125 mM KCl, 25 mM Tris-HCl, 2 mM $MgCl_2$ pH 7.5), 20% OptiPrep (Density Gradient Medium, Sigma, Germany), protein and GTP. FtsZ-YFP-mts (or FtsZ-YPF-mts*[T108A]) and GTP final concentrations were 1.65 μM and 1.4 mM respectively. Therefore, the emulsion was transferred to the reaction tube (A) and centrifuged at 100g for 7 minutes. Finally, the oil-based supernatant is discarded and 300 μl final vesicles are

1:2 or 1:3 diluted in fresh outer buffer.

PDMS Microfabrication and FtsZ assay

PDMS microstructures were fabricated using soft lithography. The inverse of the target 3D geometry was designed in SolidWorks (Dasault Systems SE), exported to STL format and converted into 3D print instructions using DeScribe (Nanoscribe GmbH) for 63x objective fabrication using default parameters. Master molds were then produced on a 4 inch silicon wafer (University Wafer) using IP-L resist on a Professional GT two photon 3D printer (both Nanoscribe GmbH) and finally developed using PGMEA and rinsed with isopropanol. To facilitate intact release of the small PDMS features, the developed master was surface-treated with a fluorophilic coating by spin coating about 200 μl of a 1:20 Cytop CTL-809AE in CTsolv.100E (both from Asahi Glass Co. Ltd., Japan) onto the master. This the Cytop dilution was directly pipetted onto the SU8 features and then spin-coated at 3000 rpm for 1 min, using a 500 rpm/s ramp. We then hard-baked the wafer for 30 min at 453 K on a hot plate to simultaneously drive IP-S polymerization to completion while also covalently anchoring the fluorophilic coating. The master was then allowed to slowly cool down to room temperature by turning off the hot plate. PDMS base and curing agent (Sylgart 184, Dow Corning) was mixed at a ratio of 10:1. About 5-10 μl of this PDMS resin was then applied onto the features. After degassing for about 15 min, cleaned microscope slides where placed onto the PDMS droplet and gently pressed to squeeze the PDMS into a thin film, before cured the PDMS at 80 °C for at least one hour. The coverside was then gently peeled off the silicon wafer using a razor blade and stored for further use.

Supported lipid bilayers (SLBs) over PDMS structures were prepared according to our recent study [82] with the difference that plasma-cleaner time was carefully chosen to not affect the PDMS structure (5 mins). FtsZ concentration was 0.1 μM with 4mM GTP in buffer: 150 mM KCl, 50 mM Tris-HCl, 5 mM $MgCl_2$ pH 7.5.

Image analysis

Image analysis and plotting was carried out in MATLAB (MathWorks, USA). To generate kymographs, a script allowed the user to define a circular section by providing 2 coordinates. This circular section is automatically fitted to a circle with radius r (in this case, $r = 0.5$ μm). Then, 3 trajectories corresponding to 3 concentric circles having radii r, $r + 1$, and $r - 1$ pixels were determined. At this point, the script read the time-series data

and calculate a kymograph for each time point and trajectory. The final kymograph corresponds to the average of the 3 different trajectories (1). To determine tube diameter, the intensity over a representative tube section was normalized to be fitted to a Gaussian function. Then, the reported here diameter represented half-width of the Gaussian. To quantify the arc-length (helical shapes projection to an 2D image), tubes were binarized and fitted to a function using linear interpolation. Then, the arc-length of the function was calculated. The protein density was calculated by measuring, over the tube, the FtsZ-intensity-difference between initial and final acquisition. This difference was divided by the FtsZ intensity on the GUV (in the tube proximity) times the tube length. To measure the pitch in the spring-like tubes, a Gaussian-filter was applied to every image. The tube red-lipid-intensity profile was integrated and normalized, in a perpendicular-direction (to the tube), to find the pixel-position where the normalized intensity was "1" and closer to "0.3". The 1 (maximum) position pixel defined the center of the tube while "0.3" defined the upper and lower limit of the tube. The intensity profile, now in parallel direction to the tube, was plotted for these 3 locations: up, center and down. Using this intensity profile, peaks are automatically found and then pitch was calculated. Every experiment was eye-inspected to avoid miscalculation. To measure the size distribution of encapsulated rings (Figure 4), the diameter was manually measured using intensity profile in ImageJ (NIH, USA). Diameters were exported and plotted in MATLAB. All shown images were adjusted in ImageJ.

Methods related to protein purification and optical tweezers were described in chapters II and III, respectively

IV.2.4 Supporting Information

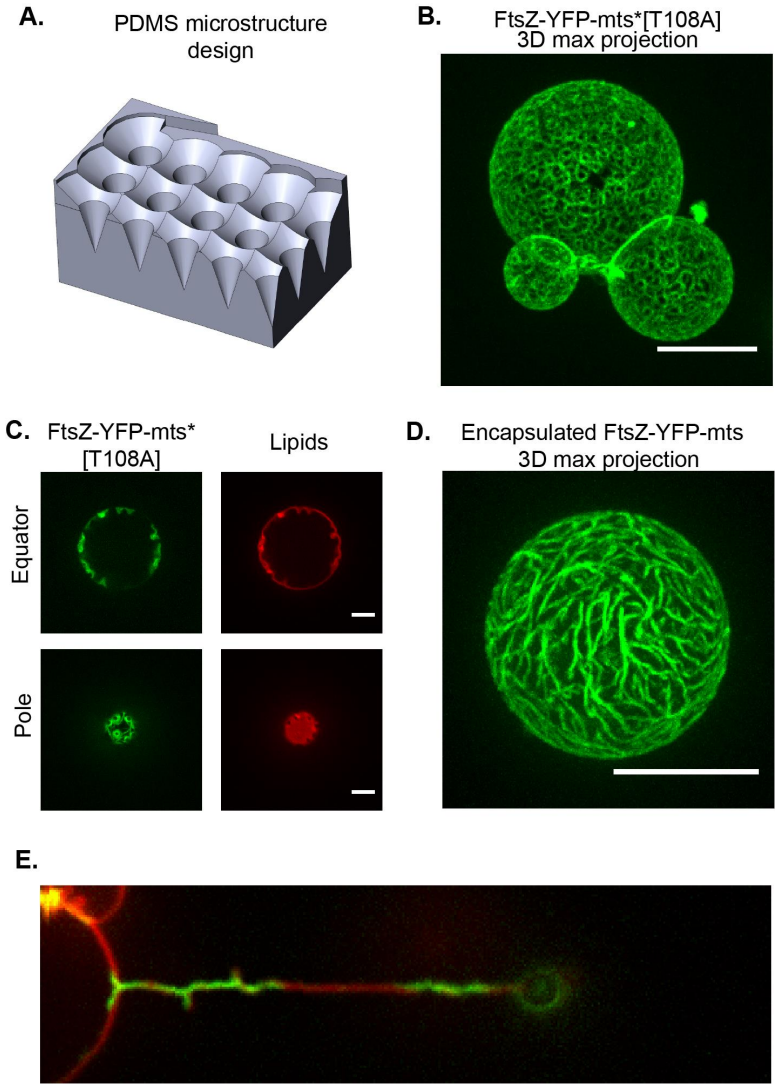

Figure S1. A) 3D sketch of the PMDS microstructure with inwards cone-like shapes. B) FtsZ-YFP-mts*[T108A] also self-assembled into ring-like structures under similar used conditions for FtsZ-YFP-mts rings (main text). C) After deflation, FtsZ-YFP-mts*[T108A] induced inwards conical deformations emerging from before mentioned rings. D) Using an encapsulation approach, Mg^{+2} and GTP content-conditions were fine-tuned to obtain either ring structures (Fig. 4) or nematic phases at a higher membrane protein density. E) Further evidence for FtsZ-torsion over lipid tubes can be found in (less frequent) experiments displaying plectonic/supercoiled regions. (Scale bar = 5 µm)

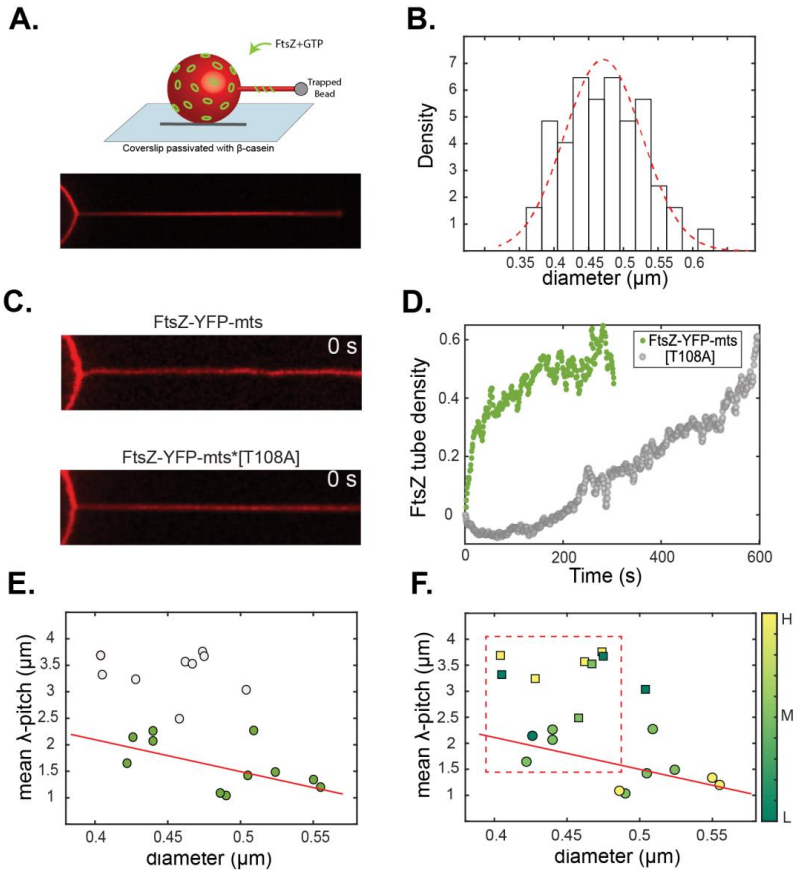

Figure S2. A) Schematic representation of pulling tubes from deflated GUVs exhibiting ring-like structures that promoted inwards deformations. B) The diameter distribution (N=55) showed a gauss-like distribution with a mean of 0.47 μm. This implied that membrane tensions equivalent to this mean (± std) were highly frequent despite of precise control on the vesicle membrane tension. C) Similar initial diameter (0.44 μm) for experiments shown in Figure 2 B-C. D) For experiments shown in Fig. 2 B&C, FtsZ-YFP-mts entered rapidly to the lipid tube while the mutant without GTPase activity reached comparable FtsZ tube densities in a slower manner. E) To rule out that GTPase-related compression shown in Fig 2 A&B was not biased by diameter size and protein density, we analyzed 11 and 9 experiments for FtsZ-YFP-mts and FtsZ-YFP-mts*[T108A] to calculate the mean-λ-pitch for each experiment. Although there is a mild correlation for FtsZ-YFP-mts (green circles) between mean-λ-pitch and diameter (red line), FtsZ-YFP-mts*[T108A] (gray circles) experiments, with comparable diameter, displayed a larger mean-λ-pitch. F) For similar tube diameters (red dashed square), dominant higher protein densities (yellow and light-green colors) for FtsZ-YFP-mts*[T108A] (squares) achieved a longer mean-λ-pitch compared to FtsZ-YFP-mts (circles) having intermediate (M) and low (L) protein densities (light and dark green). High, medium and low protein densities ρ were defined as: (H) $1 < \rho < 0.66$; (M) $0.66 < \rho < 0.33$ and (L) $\rho < 0.33$.

V

CONCLUSIONS AND OUTLOOK

In this thesis I showed that the protein chimera FtsZ-YFP-mts self-assembled into dynamic treadmilling ring-like structures, contrary to expected according to prior evidence [53]. The parameter that determined the appearance of ring-like structures was the surface protein density agreeing with theoretical work [22]. This means that rings were only obtained at "intermediate densities" while a parallel-nematic arrangement of filaments was observed at high densities. More than an specific anchor-protein, I evidenced that the emergence of treadmilling rings depended on the GTPase activity, agreeing with recent *in vivo* evidence [11, 117]. Altogether, this showed that the protein chimera FtsZ-YFP-mts represented a powerful minimal FtsZ-system to study FtsZ membrane interactions.

Consequently, I reconstituted FtsZ-YFP-mts ring-like structures on soft and deformable vesicles. Interestingly, these rings produce inwards vortex-like deformations. To study the equivalence of these inwards deformations over a soft tube-like geometry, I implemented a novel technique to pull tubes from GUVs using optical tweezers. Therefore, inwards deformations were equivalent to helical spring-like deformations over a tubular geometry. These helical deformations can be rationalized by twisting an elastic rod. In addition, GTPase activity triggered a super-twisted state causing spring compression and delivering forces around $0.6 - 1$ pN. This GTPase dependent spring-compression was equivalent to the formation of constriction necks when FtsZ was reconstituted inside GUVs. Therefore, I suggest that FtsZ makes constriction via torsional stress.

Assessing the relevance of torsion in the context of bacterial cytokinesis (*in vivo*) represents a very complicated task. However, *E. coli* strains displaying FtsZ spirals showed a "twisted" septum [2] (Fig.V.1). Similar morphology was observed for strains with lowered FtsZ GTPase activity [117]. The possible link between a "twisted septum" and the torsion of proteins such as FtsZ represents an exciting topic to investigate *in vivo*.

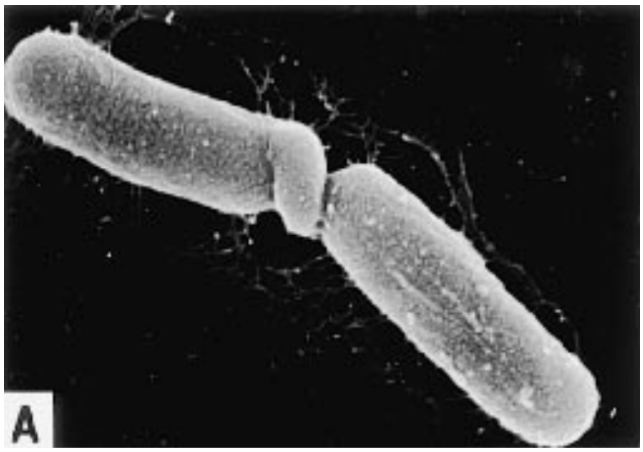

Figure V.1: Twisted septum Retrieved from [2]

Bibliography

[1] David W. Adams and Jeff Errington. Bacterial cell division: assembly, maintenance and disassembly of the Z ring. *Nature Reviews Microbiology*, 7(9):642–653, September 2009.

[2] Stephen G. Addinall and Joe Lutkenhaus. FtsZ-spirals and -arcs determine the shape of the invaginating septa in some mutants of Escherichia coli. *Molecular Microbiology*, 22(2):231–237, 1996.

[3] Jun F. Allard and Eric N. Cytrynbaum. Force generation by a dynamic Z-ring in Escherichia coli cell division. *Proceedings of the National Academy of Sciences*, 106(1):145–150, January 2009.

[4] David E. Anderson, Frederico J. Gueiros-Filho, and Harold P. Erickson. Assembly dynamics of FtsZ rings in Bacillus subtilis and Escherichia coli and effects of FtsZ-regulating proteins. *Journal of Bacteriology*, 186(17):5775–5781, September 2004.

[5] Steven S. Andrews. Methods for modeling cytoskeletal and DNA filaments. *Physical Biology*, 11(1):011001, January 2014.

[6] Bruno Antonny, Christopher Burd, Pietro De Camilli, Elizabeth Chen, Oliver Daumke, Katja Faelber, Marijn Ford, Vadim A. Frolov, Adam Frost, Jenny E. Hinshaw, Tom Kirchhausen, Michael M. Kozlov, Martin Lenz, Harry H. Low, Harvey McMahon, Christien Merrifield, Thomas D. Pollard, Phillip J. Robinson, Aurelien Roux, and Sandra Schmid. Membrane fission by dynamin: what we know and what we need to know. *The EMBO journal*, 35(21):2270–2284, 2016.

[7] Senthil Arumugam, Grzegorz Chwastek, Elisabeth Fischer-Friedrich, Carina Ehrig, Ingolf Monch, and Petra Schwille. Surface Topology Engineering of Membranes for the Mechanical Investigation of the Tubulin Homologue FtsZ. *Angewandte Chemie International Edition*, 51(47):11858–11862, November 2012.

[8] A. Ashkin. Acceleration and Trapping of Particles by Radiation Pressure. *Physical Review Letters*, 24(4):156–159, January 1970.

[9] A. Ashkin. Forces of a single-beam gradient laser trap on a dielectric sphere in the ray optics regime. *Biophysical Journal*, 61(2):569–582, February 1992.

[10] Patricia Bassereau, Benoit Sorre, and Aurore Levy. Bending lipid membranes: Experiments after W. Helfrich's model. *Advances in Colloid and Interface Science*, 208:47–57, June 2014.

[11] Alexandre W. Bisson-Filho, Yen-Pang Hsu, Georgia R. Squyres, Erkin Kuru, Fabai Wu, Calum Jukes, Yingjie Sun, Cees Dekker, Seamus Holden, Michael S. VanNieuwenhze, Yves V. Brun, and Ethan C. Garner. Treadmilling by FtsZ filaments drives peptidoglycan synthesis and bacterial cell division. *Science*, 355(6326):739–743, February 2017.

[12] David Boal. *Mechanics of the Cell*. Cambridge University Press, 2001.

[13] N. Borghi, O. Rossier, and F. Brochard-Wyart. Hydrodynamic extrusion of tubes from giant vesicles. *EPL (Europhysics Letters)*, 64(6):837, December 2003.

[14] A A Brian and H M McConnell. Allogeneic stimulation of cytotoxic T cells by supported planar membranes. *Proceedings of the National Academy of Sciences of the United States of America*, 81(19):6159–6163, October 1984.

[15] Chase Broedersz and Fred MacKintosh. Modeling semiflexible polymer networks. *Reviews of Modern Physics*, 86(3):995–1036, July 2014.

[16] Yaodong Chen and Harold P. Erickson. Rapid in vitro assembly dynamics and subunit turnover of FtsZ demonstrated by fluorescence resonance energy transfer. *The Journal of Biological Chemistry*, 280(23):22549–22554, June 2005.

[17] Adai Colom, Lorena Redondo-Morata, Nicolas Chiaruttini, Aurelien Roux, and Simon Scheuring. Dynamic remodeling of the dynamin helix during membrane constriction. *Proceedings of the National Academy of Sciences*, 114(21):5449–5454, May 2017.

[18] Carla Coltharp, Jackson Buss, Trevor M. Plumer, and Jie Xiao. Defining the rate-limiting processes of bacterial cytokinesis. *Proceedings of the National Academy of Sciences*, 113(8):E1044–E1053, February 2016.

[19] Carla Coltharp and Jie Xiao. Beyond force generation: Why is a dynamic ring of FtsZ polymers essential for bacterial cytokinesis? *BioEssays*, 39(1):e201600179, 2017.

[20] Tanneke den Blaauwen, Leendert W Hamoen, and Petra Anne Levin. The divisome at 25: the road ahead. *Current Opinion in Microbiology*, 36:85–94, April 2017.

[21] Yi Deng, Mingzhai Sun, and Joshua W. Shaevitz. Direct Measurement of Cell Wall Stress Stiffening and Turgor Pressure in Live Bacterial Cells. *Physical Review Letters*, 107(15):158101, October 2011.

[22] Jonas Denk, Lorenz Huber, Emanuel Reithmann, and Erwin Frey. Active Curved Polymers Form Vortex Patterns on Membranes. *Physical Review Letters*, 116(17):178301, April 2016.

[23] Imre Derenyi, Frank Julicher, and Jacques Prost. Formation and Interaction of Membrane Tubes. *Physical Review Letters*, 88(23):238101, May 2002.

[24] Markus Deserno. Membrane Elasticity and Mediated Interactions in Continuum Theory: A Differential Geometric Approach. In Roland Faller, Marjorie L. Longo, Subhash H. Risbud, and Thomas Jue, editors, *Biomembrane Frontiers: Nanostructures, Models, and the Design of Life*, Handbook of Modern Biophysics, pages 41–74. Humana Press, Totowa, NJ, 2009.

[25] Shishen Du and Joe Lutkenhaus. Assembly and activation of the Escherichia coli divisome. *Molecular Microbiology*, 105(2):177–187, 2017.

[26] H. P. Erickson, D. W. Taylor, K. A. Taylor, and D. Bramhill. Bacterial cell division protein FtsZ assembles into protofilament sheets and minirings, structural homologs of tubulin polymers. *Proceedings of the National Academy of Sciences*, 93(1):519–523, January 1996.

[27] Harold P. Erickson. How bacterial cell division might cheat turgor pressure - a unified mechanism of septal division in Gram-positive and Gram-negative bacteria. *BioEssays*, 39(8):1700045, 2017.

[28] Harold P. Erickson, David E. Anderson, and Masaki Osawa. FtsZ in Bacterial Cytokinesis: Cytoskeleton and Force Generator All in One. *Microbiology and Molecular Biology Reviews*, 74(4):504–528, December 2010.

[29] Harold P. Erickson and Masaki Osawa. Cell division without FtsZ - a variety of redundant mechanisms. *Molecular microbiology*, 78(2):267–270, October 2010.

[30] Julien Fierling, Albert Johner, Igor M. Kulic, Herve Mohrbach, and Martin Michael Muller. How bio-filaments twist membranes. *Soft Matter*, 12(26):5747–5757, June 2016.

[31] Kenneth N. Fish. Total internal reflection fluorescence (TIRF) microscopy. *Current Protocols in Cytometry*, Chapter 12:Unit12.18, October 2009.

[32] Nicola De Franceschi, Maryam Alqabandi, Nolwenn Miguet, Christophe Caillat, Stephanie Mangenot, Winfried Weissenhorn, and Patricia Bassereau. The ESCRT protein CHMP2b acts as a diffusion barrier on reconstituted membrane necks. *J Cell Sci*, 132(4):jcs217968, February 2019.

[33] Guo Fu, Tao Huang, Jackson Buss, Carla Coltharp, Zach Hensel, and Jie Xiao. In Vivo Structure of the E. coli FtsZ-ring Revealed by Photoactivated Localization Microscopy (PALM). *PLOS ONE*, 5(9):e12680, September 2010.

[34] F. Gittes, B. Mickey, J. Nettleton, and J. Howard. Flexural rigidity of microtubules and actin filaments measured from thermal fluctuations in shape. *The Journal of Cell Biology*, 120(4):923–934, February 1993.

[35] Daniel P. Haeusser and William Margolin. Splitsville: structural and functional insights into the dynamic bacterial Z ring. *Nature Reviews Microbiology*, 14(5):305–319, May 2016.

[36] Loic Hamon, Dulal Panda, Philippe Savarin, Vandana Joshi, Johann Bernhard, Elodie Mucher, Alain Mechulam, Patrick A. Curmi, and David Pastre. Mica Surface Promotes the Assembly of Cytoskeletal Proteins. *Langmuir*, 25(6):3331–3335, March 2009.

[37] W. Helfrich. Elastic properties of lipid bilayers: theory and possible experiments. *Zeitschrift Fur Naturforschung. Teil C: Biochemie, Biophysik, Biologie, Virologie*, 28(11):693–703, December 1973.

[38] Seamus Holden. Probing the mechanistic principles of bacterial cell division with super-resolution microscopy. *Current Opinion in Microbiology*, 43:84–91, June 2018.

[39] Seamus J. Holden, Thomas Pengo, Karin L. Meibom, Carmen Fernandez Fernandez, Justine Collier, and Suliana Manley. High throughput 3d super-resolution microscopy reveals Caulobacter crescentus in vivo Z-ring organization. *Proceedings of the National Academy of Sciences*, 111(12):4566–4571, March 2014.

[40] I. Horger, E. Velasco, J. Mingorance, G. Rivas, P. Tarazona, and M. Velez. Langevin computer simulations of bacterial protein filaments and the force-generating mechanism during cell division. *Physical Review E*, 77(1):011902, January 2008.

[41] Jen Hsin, Ajay Gopinathan, and Kerwyn C. Huang. Nucleotide-dependent conformations of FtsZ dimers and force generation observed through molecular dynamics simulations. *Proceedings of the National Academy of Sciences*, 109(24):9432–9437, June 2012.

[42] Sonia Huecas and Jose Manuel Andreu. Energetics of the Cooperative Assembly of Cell Division Protein FtsZ and the Nucleotide Hydrolysis Switch. *Journal of Biological Chemistry*, 278(46):46146–46154, November 2003.

[43] Sonia Huecas and Jose Manuel Andreu. Polymerization of nucleotide-free, GDP- and GTP-bound cell division protein FtsZ: GDP makes the difference. *FEBS Letters*, 569(1-3):43–48, July 2004.

[44] Philip H. Jones, Onofrio M. Marago, and Giovanni Volpe. *Optical Tweezers: Principles and Applications*. Cambridge University Press, December 2015.

[45] Matthias D. Koch and Joshua W. Shaevitz. Introduction to Optical Tweezers. In Arne Gennerich, editor, *Optical Tweezers: Methods and Protocols*, Methods in Molecular Biology, pages 3–24. Springer New York, New York, NY, 2017.

[46] Leopold Kong, Kem A. Sochacki, Huaibin Wang, Shunming Fang, Bertram Canagarajah, Andrew D. Kehr, William J. Rice, Marie-Paule Strub, Justin W. Taraska, and Jenny E. Hinshaw. Cryo-EM of the dynamin polymer assembled on lipid membrane. *Nature*, 560(7717):258, August 2018.

[47] R Kwok and E Evans. Thermoelasticity of large lecithin bilayer vesicles. *Biophysical Journal*, 35(3):637–652, September 1981.

[48] Joseph R. Lakowicz. *Principles of Fluorescence Spectroscopy*. Springer, 3 edition, 2006.

[49] Ganhui Lan, Brian R. Daniels, Terrence M. Dobrowsky, Denis Wirtz, and Sean X. Sun. Condensation of FtsZ filaments can drive bacterial cell division. *Proceedings of the National Academy of Sciences*, 106(1):121–126, January 2009.

[50] Ganhui Lan, Charles W. Wolgemuth, and Sean X. Sun. Z-ring force and cell shape during division in rod-like bacteria. *Proceedings of the National Academy of Sciences*, 104(41):16110–16115, October 2007.

[51] Woei Ming Lee, Peter J. Reece, Robert F. Marchington, Nikolaus K. Metzger, and Kishan Dholakia. Construction and calibration of an optical trap on a fluorescence optical microscope. *Nature Protocols*, 2(12):3226–3238, December 2007.

[52] Bing Liu, Logan Persons, Lynda Lee, and Piet A. J. de Boer. Roles for both FtsA and the FtsBLQ subcomplex in FtsN-stimulated cell constriction in Escherichia coli. *Molecular Microbiology*, 95(6):945–970, March 2015.

[53] Martin Loose and Timothy J. Mitchison. The bacterial cell division proteins FtsA and FtsZ self-organize into dynamic cytoskeletal patterns. *Nature Cell Biology*, 16(1):38–46, January 2014.

[54] Chunlin Lu, Mary Reedy, and Harold P. Erickson. Straight and Curved Conformations of FtsZ Are Regulated by GTP Hydrolysis. *Journal of Bacteriology*, 182(1):164–170, January 2000.

[55] ML Martin-Fernandez, CJ Tynan, and SED Webb. A "pocket guide" to total internal reflection fluorescence. *Journal of Microscopy*, 252(1):16–22, October 2013.

[56] Ariadna Martos, Ana Raso, Mercedes Jimenez, Zdenek Petrasek, German Rivas, and Petra Schwille. FtsZ Polymers Tethered to the Membrane by ZipA Are Susceptible to Spatial Regulation by Min Waves. *Biophysical Journal*, 108(9):2371–2383, May 2015.

[57] Pablo Mateos-Gil, Alfonso Paez, Ines Horger, German Rivas, Miguel Vicente, Pedro Tarazona, and Marisela Velez. Depolymerization dynamics of individual filaments of bacterial cytoskeletal protein FtsZ. *Proceedings of the National Academy of Sciences*, 109(21):8133–8138, May 2012.

[58] Romain Mercier, Yoshikazu Kawai, and Jeff Errington. Wall proficient *E. coli* capable of sustained growth in the absence of the Z-ring division machine. *Nature Microbiology*, 1(8):16091, August 2016.

[59] Jesus Mingorance, Michael Tadros, Miguel Vicente, Jose Manuel Gonzalez, German Rivas, and Marisela Velez. Visualization of Single Escherichia coli FtsZ Filament Dynamics with Atomic Force Microscopy. *Journal of Biological Chemistry*, 280(21):20909–20914, May 2005.

[60] W. E. Moerner and David P. Fromm. Methods of single-molecule fluorescence spectroscopy and microscopy. *Review of Scientific Instruments*, 74(8):3597–3619, July 2003.

[61] Begona Monterroso, Ruben Ahijado-Guzman, Belen Reija, Carlos Alfonso, Silvia Zorrilla, Allen P. Minton, and German Rivas. Mg2+-Linked Self-Assembly of FtsZ in the Presence of GTP or a GTP Analogue Involves the Concerted Formation of a Narrow Size Distribution of Oligomeric Species. *Biochemistry*, 51(22):4541–4550, June 2012.

[62] Sandrine Morlot, Valentina Galli, Marius Klein, Nicolas Chiaruttini, John Manzi, Frederic Humbert, Luis Dinis, Martin Lenz, Giovanni Cappello, and Aurelien Roux. Membrane Shape at the Edge of the Dynamin Helix Sets Location and Duration of the Fission Reaction. *Cell*, 151(3):619–629, October 2012.

[63] A. Mukherjee and J. Lutkenhaus. Guanine nucleotide-dependent assembly of FtsZ into filaments. *Journal of Bacteriology*, 176(9):2754–2758, May 1994.

[64] Keir C. Neuman and Steven M. Block. Optical trapping. *Review of Scientific Instruments*, 75(9):2787–2809, September 2004.

[65] Lili Niu and Ji Yu. Investigating Intracellular Dynamics of FtsZ Cytoskeleton with Photoactivation Single-Molecule Tracking. *Biophysical Journal*, 95(4):2009–2016, August 2008.

[66] Tomoo Ohashi, Cynthia A. Hale, Piet A. J. de Boer, and Harold P. Erickson. Structural Evidence that the P/Q Domain of ZipA Is an Unstructured, Flexible Tether between the Membrane and the C-Terminal FtsZ-Binding Domain. *Journal of Bacteriology*, 184(15):4313–4315, August 2002.

[67] K. Olbrich, W. Rawicz, D. Needham, and E. Evans. Water Permeability and Mechanical Strength of Polyunsaturated Lipid Bilayers. *Biophysical Journal*, 79(1):321–327, July 2000.

[68] Cristina Ortiz, Paolo Natale, Laura Cueto, and Miguel Vicente. The keepers of the ring: regulators of FtsZ assembly. *FEMS Microbiology Reviews*, 40(1):57–67, January 2016.

[69] Masaki Osawa, David E. Anderson, and Harold P. Erickson. Reconstitution of Contractile FtsZ Rings in Liposomes. *Science*, 320(5877):792–794, May 2008.

[70] Masaki Osawa, David E. Anderson, and Harold P. Erickson. Curved FtsZ protofilaments generate bending forces on liposome membranes. *The EMBO journal*, 28(22):3476–3484, November 2009.

[71] Masaki Osawa and Harold P. Erickson. Chapter 1 - Tubular liposomes with variable permeability for reconstitution of FtsZ rings. In *Methods in Enzymology*, volume 464, pages 3–17. 2009.

[72] Masaki Osawa and Harold P. Erickson. Liposome division by a simple bacterial division machinery. *Proceedings of the National Academy of Sciences*, 110(27):11000–11004, July 2013.

[73] Masaki Osawa and Harold P. Erickson. Turgor Pressure and Possible Constriction Mechanisms in Bacterial Division. *Frontiers in Microbiology*, 9, 2018.

[74] Martina Pannuzzo, Zachary A McDargh, and Markus Deserno. The role of scaffold reshaping and disassembly in dynamin driven membrane fission. *eLife*, 7:e39441, December 2018.

[75] Sophie Pautot, Barbara J. Frisken, and D. A. Weitz. Production of Unilamellar Vesicles Using an Inverted Emulsion. *Langmuir*, 19(7):2870–2879, April 2003.

[76] Laura Picas, Felix Rico, and Simon Scheuring. Direct Measurement of the Mechanical Properties of Lipid Phases in Supported Bilayers. *Biophysical Journal*, 102(1):L01–L03, January 2012.

[77] Sebastien Pichoff and Joe Lutkenhaus. Tethering the Z ring to the membrane through a conserved membrane targeting sequence in FtsA. *Molecular Microbiology*, 55(6):1722–1734, March 2005.

[78] Martin Pilhofer, Karin Aistleitner, Jacob Biboy, Joe Gray, Erkin Kuru, Edward Hall, Yves V. Brun, Michael S. VanNieuwenhze, Waldemar Vollmer, Matthias Horn, and Grant J. Jensen. Discovery of chlamydial peptidoglycan reveals bacteria with murein sacculi but without FtsZ. *Nature communications*, 4, December 2013.

[79] David Popp, Mitsusada Iwasa, Akihiro Narita, Harold P. Erickson, and Yuichiro Maeda. FtsZ condensates: An in vitro electron microscopy study. *Biopolymers*, 91(5):340–350, 2009.

[80] Coline Prevost, Hongxia Zhao, John Manzi, Emmanuel Lemichez, Pekka Lappalainen, Andrew Callan-Jones, and Patricia Bassereau. IRSp53 senses negative membrane curvature and phase separates along membrane tubules. *Nature Communications*, 6:8529, October 2015.

[81] Sivaramakrishnan Ramadurai, Andrea Holt, Victor Krasnikov, Geert van den Bogaart, J. Antoinette Killian, and Bert Poolman. Lateral Diffusion of Membrane Proteins. *Journal of the American Chemical Society*, 131(35):12650–12656, September 2009.

[82] Diego A. Ramirez-Diaz, Daniela A. Garcia-Soriano, Ana Raso, Jonas Mucksch, Mario Feingold, German Rivas, and Petra Schwille. Treadmilling analysis reveals new insights into dynamic FtsZ ring architecture. *PLOS Biology*, 16(5):e2004845, May 2018.

[83] Beatrice Ramm, Philipp Glock, Jonas Mucksch, Philipp Blumhardt, Daniela A. Garcia-Soriano, Michael Heymann, and Petra Schwille. The MinDE system is a generic spatial cue for membrane protein distribution in vitro. *Nature Communications*, 9(1):3942, September 2018.

[84] W. Rawicz, K. C. Olbrich, T. McIntosh, D. Needham, and E. Evans. Effect of Chain Length and Unsaturation on Elasticity of Lipid Bilayers. *Biophysical Journal*, 79(1):328–339, July 2000.

[85] Ana Isabel Rico, Marcin Krupka, and Miguel Vicente. In the beginning, Escherichia coli assembled the proto-ring: an initial phase of division. *The Journal of Biological Chemistry*, 288(29):20830–20836, July 2013.

[86] German Rivas, Sven K Vogel, and Petra Schwille. Reconstitution of cytoskeletal protein assemblies for large-scale membrane transformation. *Current Opinion in Chemical Biology*, 22:18–26, October 2014.

[87] Enrique R. Rojas, Gabriel Billings, Pascal D. Odermatt, George K. Auer, Lillian Zhu, Amanda Miguel, Fred Chang, Douglas B. Weibel, Julie A. Theriot, and Kerwyn Casey Huang. The outer membrane is an essential load-bearing element in Gram-negative bacteria. *Nature*, 559(7715):617, July 2018.

[88] Aurelien Roux. The physics of membrane tubes: soft templates for studying cellular membranes. *Soft Matter*, 9(29):6726–6736, July 2013.

[89] Aurelien Roux, Gerbrand Koster, Martin Lenz, Benoit Sorre, Jean-Baptiste Manneville, Pierre Nassoy, and Patricia Bassereau. Membrane curvature controls dynamin polymerization. *Proceedings of the National Academy of Sciences*, 107(9):4141–4146, March 2010.

[90] Veronica Wells Rowlett and William Margolin. The bacterial Min system. *Current Biology*, 23(13):R553–R556, July 2013.

[91] Pablo Gonzalez de Prado Salas, Ines Horger, Fernando Martin-Garcia, Jesus Mendieta, Alvaro Alonso, Mario Encinar, Paulino Gomez-Puertas, Marisela Velez, and Pedro Tarazona. Torsion and curvature of FtsZ filaments. *Soft Matter*, 10(12):1977–1986, February 2014.

[92] Johannes Schoneberg, Mark Remec Pavlin, Shannon Yan, Maurizio Righini, Il-Hyung Lee, Lars-Anders Carlson, Amir Houshang Bahrami, Daniel H. Goldman, Xuefeng Ren, Gerhard Hummer, Carlos Bustamante, and James H. Hurley. ATP-dependent force generation and membrane scission by ESCRT-III and Vps4. *Science*, 362(6421):1423–1428, December 2018.

[93] Sviatlana Shashkova and Mark C. Leake. Single-molecule fluorescence microscopy review: shedding new light on old problems. *Bioscience Reports*, 37(4):BSR20170031, August 2017.

[94] Bang Shen and Joe Lutkenhaus. The conserved C-terminal tail of FtsZ is required for the septal localization and division inhibitory activity of MinCC/MinD. *Molecular microbiology*, 72(2):410–424, April 2009.

[95] Thomas J. Silhavy, Daniel Kahne, and Suzanne Walker. The Bacterial Cell Envelope. *Cold Spring Harbor Perspectives in Biology*, 2(5), May 2010.

[96] Bill Soderstrom, Kiavash Mirzadeh, Stephen Toddo, Gunnar von Heijne, Ulf Skoglund, and Daniel O. Daley. Coordinated disassembly of the divisome complex in Escherichia coli. *Molecular Microbiology*, 101(3):425–438, 2016.

[97] Bill Soderstrom, Karl Skoog, Hans Blom, David S. Weiss, Gunnar von Heijne, and Daniel O. Daley. Disassembly of the divisome in Escherichia coli: evidence that FtsZ dissociates before compartmentalization. *Molecular Microbiology*, 92(1):1–9, April 2014.

[98] Smita P. Soni and Robert V. Stahelin. The Ebola Virus Matrix Protein VP40 Selectively Induces Vesiculation from Phosphatidylserine-enriched Membranes. *Journal of Biological Chemistry*, 289(48):33590–33597, November 2014.

[99] Benoit Sorre, Andrew Callan-Jones, John Manzi, Bruno Goud, Jacques Prost, Patricia Bassereau, and Aurelien Roux. Nature of curvature coupling of amphiphysin with membranes depends on its bound density. *Proceedings of the National Academy of Sciences*, 109(1):173–178, January 2012.

[100] Jeanne C. Stachowiak, Eva M. Schmid, Christopher J. Ryan, Hyoung Sook Ann, Darryl Y. Sasaki, Michael B. Sherman, Phillip L. Geissler, Daniel A. Fletcher, and Carl C. Hayden. Membrane bending by protein-protein crowding. *Nature Cell Biology*, 14(9):944–949, September 2012.

[101] Piotr Szwedziak, Qing Wang, Tanmay A. M. Bharat, Matthew Tsim, and Jan Lowe. Architecture of the ring formed by the tubulin homologue FtsZ in bacterial cell division. *eLife*, 3:e04601, January 2015.

[102] Tetsuya Takeda, Toshiya Kozai, Huiran Yang, Daiki Ishikuro, Kaho Seyama, Yusuke Kumagai, Tadashi Abe, Hiroshi Yamada, Takayuki Uchihashi, Toshio Ando, and Kohji Takei. Dynamic clustering of dynamin-amphiphysin helices regulates membrane constriction and fission coupled with GTP hydrolysis. *eLife*, 7:e30246, January 2018.

[103] Swapna Thanedar and William Margolin. FtsZ Exhibits Rapid Movement and Oscillation Waves in Helix-like Patterns in Escherichia coli. *Current Biology*, 14(13):1167–1173, July 2004.

[104] Timoshenko. *Theory of Elasticity*. Mcgraw Hill Education, January 2010.

[105] Shoichi Toyabe, Takahiro Watanabe-Nakayama, Tetsuaki Okamoto, Seishi Kudo, and Eiro Muneyuki. Thermodynamic efficiency and mechanochemical coupling of F1-ATPase. *Proceedings of the National Academy of Sciences*, 108(44):17951–17956, November 2011.

[106] Anke Treuner-Lange, Kryssia Aguiluz, Chris van der Does, Nuria Gomez-Santos, Andrea Harms, Dominik Schumacher, Peter Lenz, Michael Hoppert, Jorg Kahnt, Jose Munoz-Dorado, and Lotte Sogaard-Andersen. PomZ, a ParA-like protein, regulates Z-ring formation and cell division in Myxococcus xanthus. *Molecular Microbiology*, 87(2):235–253, 2013.

[107] Mary-Jane Tsang and Thomas G Bernhardt. Guiding divisome assembly and controlling its activity. *Current Opinion in Microbiology*, 24:60–65, April 2015.

[108] Yuri Tsuda, Hironori Yasutake, Akihiko Ishijima, and Toshio Yanagida. Torsional rigidity of single actin filaments and actin-actin bond breaking force under torsion measured directly by in vitro micromanipulation. *Proceedings of the National Academy of Sciences of the United States of America*, 93(23):12937–12942, November 1996.

[109] Daniel Turner, Ian Portman, Timothy Dafforn, Alison Rodger, David Roper, Corinne Smith, and Matthew Turner. The Mechanics of FtsZ Fibers. *Biophysical Journal*, 102(4):731–738, February 2012.

[110] Joost van Mameren, Karen C. Vermeulen, Fred Gittes, and Christoph F. Schmidt. Leveraging Single Protein Polymers To Measure Flexural Rigidity. *The Journal of Physical Chemistry B*, 113(12):3837–3844, March 2009.

[111] James M. Wagstaff, Matthew Tsim, Maria A. Oliva, Alba Garcia-Sanchez, Danguole Kureisaite-Ciziene, Jose Manuel Andreu, and Jan Lowe. A Polymerization-Associated Structural Switch in FtsZ That Enables Treadmilling of Model Filaments. *mBio*, 8(3):e00254–17, July 2017.

[112] Peter Walde, Katia Cosentino, Helen Engel, and Pasquale Stano. Giant Vesicles: Preparations and Applications. *ChemBioChem*, 11(7):848–865, May 2010.

[113] Kathryn P. Wall, Rebecca Dillon, and Michelle K. Knowles. Fluorescence quantum yield measurements of fluorescent proteins: A laboratory experiment for a biochemistry or molecular biophysics laboratory course. *Biochemistry and Molecular Biology Education*, 43(1):52–59, 2015.

[114] Laura Weimann, Kristina A. Ganzinger, James McColl, Kate L. Irvine, Simon J. Davis, Nicholas J. Gay, Clare E. Bryant, and David Klenerman. A Quantitative Comparison of Single-Dye Tracking Analysis Tools Using Monte Carlo Simulations. *PLOS ONE*, 8(5):e64287, May 2013.

[115] Adrian M. Whatmore and Robert H. Reed. Determination of turgor pressure in Bacillus subtilis: a possible role for K+ in turgor regulation. *Microbiology*, 136(12):2521–2526, 1990.

[116] Jie Xiao and Erin D Goley. Redefining the roles of the FtsZ-ring in bacterial cytokinesis. *Current Opinion in Microbiology*, 34:90–96, December 2016.

[117] Xinxing Yang, Zhixin Lyu, Amanda Miguel, Ryan McQuillen, Kerwyn Casey Huang, and Jie Xiao. GTPase activity-coupled treadmilling of the bacterial tubulin FtsZ organizes septal cell wall synthesis. *Science*, 355(6326):744–747, February 2017.

[118] Yong-Mei Zhang and Charles O. Rock. Membrane lipid homeostasis in bacteria. *Nature Reviews Microbiology*, 6(3):222–233, March 2008.

[119] Qinsi Zheng, Steffen Jockusch, Zhou Zhou, and Scott C. Blanchard. The Contribution of Reactive Oxygen Species to the Photobleaching of Organic Fluorophores. *Photochemistry and photobiology*, 90(2):448–454, March 2014.

ACKNOWLEDGEMENTS - AGRADECIMIENTOS

No hay suficientes palabras que reflejen el agradecimiento que tengo con mi familia. A mi madre Cecilia por siempre darme esa fuerza en tiempo de tristeza y por vivir con tanta intensidad aquellos momentos de alegria. A mi padre Angel por sembrar el gusto por la fisica y a mi hermano Ivan por ser incondicional. Ademas fui muy afortunado de tener a mi prima Angela, su esposo Martin, mis sobrinitos Isa y Leo y mi prima Laura aca en Munich.

Tambien quiero agradecer a mis buenos amigos: Juan, Sven, Ivan-Rey, Jose y Eric. Parceros! Con ellos siempre hubo una buena charla y una palabra de animo. La lista quedaria corta sin Lina, Cathe, Laura-Burbaum, Natalia, Sofia, Fabian, Laura-Cinnamon porque con ellos quedan bonitos recuerdos de mi tiempo en Munich.

Quiero resaltar y agradecer a las personas que leyeron esta tesis antes de ser sometida: Prof. Dr. Allen Liu, Prof. Dr. German Rivas y Dr. Ivan Rey. Ademas quiero resaltar el apoyo de German en todo mi doctorado. Mil Gracias.

Por ultimo quiero agradecer a mi supervisora Prof. Dr. Petra Schwille por dame tanta libertad y confianza al igual que a todos los miembros de su laboratorio. En especial a Silke, Sigrid y aquellos miembros que disfrutan de jugar kicker tanto como yo.